"Surface passivation effects of aluminium oxide on ultra-thin CIGS solar cells"

Kotipalli, Raja Venkata Ratan

Abstract

Among all thin-film (TF) technologies, photovoltaic (PV) cells based on copper indium gallium diselenide (CIGS) absorbers yield the highest efficiency (>22%). Current approaches and future priorities within the CIGS TF PV community are focused on CIGS thickness reduction to further lower material costs and surface passivation concepts to reduce the electronic recombination at interfaces and further enhance the solar cell performance. These approaches involve novel methods to passivate the front and rear surfaces of the CIGS absorber by implementing (i) alkali post-deposition treatments at the front surface and (ii) rear surface field-effect passivation using gallium grading schemes within the CIGS absorber layer. However, above-mentioned surface passivation approaches have been shown less effective when considering ultra-thin (<400nm) absorber layers. Hence, as an attempt to address these challenges, this thesis work is focused on the “Rear surface passivated ultra-thin CIGS solar ...

Document type : *Thèse (Dissertation)*

Université Catholique de Louvain
Ecole Polytechnique de Louvain

ICTEAM

Institute of Information and
Communication Technologies,
Electronics and Applied Mathematics

Surface Passivation Effects of Aluminum Oxide on Ultra-Thin CIGS Solar Cells

Raja Venkata Ratan Kotipalli

Thesis presented for the degree of Ph.D in Engineering Sciences

Dissertation Jury

Prof. Denis Flandre (Advisor)	UCL
Prof. Jean-Pierre Raskin	UCL
Prof. Laurent Francis	UCL
Dr. Xiaohui Tang	UCL
Dr. Bart Vermang	IMEC
Dr. Romain Tanguy Delamare	Melexis

February 2016

To Saibaba and Subbalakshmi

"The present is theirs; the future, for which I really worked, is mine."

Nikola Tesla

Acknowledgements

Firstly, I would like to express my sincere gratitude to my advisor Prof. Denis Flandre for the continuous support of my Ph.D study and related research, for his patience, motivation, and immense knowledge. His guidance helped me in all the time of research and writing of this thesis. I could not have imagined having a better advisor and mentor for my Ph.D study; and more importantly for his time, enthusiasm, efforts, patience, ever optimistic support and guidance during my stay at UCL.

Secondly, my special thanks go to Dr. Bart Vermang (IMEC-Belgium) and Prof. Marika Edoff (Ångström Solar Center-Sweden) whose collaborations resulted in interesting results, projects and scientific publications. In particular, I am grateful to Dr. Bart Vermang for enlightening me with the first glance of CIGS solar cell research. Without your support, guidance, encouragement, countless insightful ideas and suggestions, this research would not have been possible.

I am also thankful to Dr. Romain Tanguy Delamare for mentoring me for the first two years of my PhD. I sincerely thank for his cooperation, advice, and unlimited technical and personal support, which helped me to think freely in the initial stage of my PhD.

My warm regards also goes to both Prof. Laurent Francis and Dr. Xiaohui Tang for their continuous help in the surface passivation studies using atomic layer deposition (ALD) technique. I thank both of them for their expertise, guidance, support, encouragement and opportunities provided to me during my stay in UCL.

I also wish to appreciate Mr. Pascal Simon for his help in WELCOME; Mr. Andre Crahay and Mr. Christian Renaux for their assistance, training, support, guidance, and organization in WINFAB. I would especially like to thank all the charming friendly users and staff of WINFAB, WELCOME and MAXWELL, who made my stay at UCL memorable. Moreover, I would like to thank my close friends Dr. Umesh Bhaskar (Macha) and Dr. Oliver Poncelet (Sheldon) for always cheering me up and giving positive energy.

Last but not the least, I would like to thank my mother Prof. Subbalakshmi Kotipalli, my father Rama Murthy Kotipalli, my brothers (Jinney and Nukesh Kotipalli), Dr. Padma Kotipalli (her family), Anja Kotipalli (her family), Prof. Günther Benstetter (THD-Germany) and Prof. Rajendra Singh (Clemson University-USA) for supporting me spiritually throughout writing this thesis and my life in general.

List of Symbols

Symbol	Description	Unit
τ_{eff}	Effective lifetime	s
$\tau_{eff,max}$	Maximum effective lifetime	s
τ_{bulk}	Bulk lifetime	s
S_{eff}	Effective surface recombination velocity	cm/s
$S_{eff,max}$	Maximum effective surface recombination velocity	cm/s
SRV	Surface recombination velocity	cm/s
T	Absolute temperature	K
R_s	Series resistance	Ω
R_{sh}	Shunt resistance	Ω
n	Ideality factor	-
V_T	Thermal voltage (kT/q)	V
η	Power conversion efficiency	%
J_{sc}	Short-circuit current density	A/cm^2
V_{oc}	Open-circuit voltage	V
FF	Fill-Factor	%
λ	Wavelength	m
A	Absorptance	%
R	Reflectance	%
p	Density of free holes	cm^{-3}
N_{DLCP}	Density of Deep-defects	cm^{-3}
R_s	Series resistance	Ω
R_{sh}	Shunt resistance	Ω
n	Ideality factor	-
V_T	Thermal voltage (kT/q)	V
η	Power conversion efficiency	%
J_{sc}	Short-circuit current density	A/cm^2

V_{oc}	Open-circuit voltage	V
FF	Fill-Factor	%
λ	Wavelength	m
A	Absorptance	%
R	Reflectance	%
p	Density of free holes	cm^{-3}
N_{DLCP}	Density of Deep-defects	cm^{-3}
n_i	Intrinsic carrier density	cm^{-3}
N_A	Acceptor carrier concentration	cm^{-3}
N_D	Donor carrier concentration	cm^{-3}
D_n	Diffusion coefficient for electrons	cm^2/s
D_p	Diffusion coefficient for holes	cm^2/s
U_{srv}	Surface recombination rate	$cm^{-2}\ s^{-1}$
E	Energy	eV
E_C	Conduction band energy	eV
E_F	Fermi energy	eV
E_g	Bandgap energy	eV
E_V	Valency band energy	eV
R_{sh}	Sheet resistance	$\Omega/\square$
x_j	Junction depth	m
Δn	Excess election density	cm^{-3}
Δp	Excess hole density	cm^{-3}
$\Phi_{AM\ 1.5G}$	Photon flux of AM1.5G spectrum	$cm^{-2}\cdot s^{-1}$
α	Absorption coefficient	cm^{-1}
n	Refractive index	-
W	Silicon wafer thickness	m
σ_n	Electron capture cross section	cm^2
σ_p	Hole capture cross section	cm^2
ν_{th}	Thermal velocity	cm/s

D_{it}	Interface trap density	$cm^{-2} \cdot eV^{-1}$
p_s	Surface electron density	cm^{-3}
n_s	Surface hole density	cm^{-3}
S_{n0}	Electron surface recombination velocity	cm/s
S_{p0}	Hole surface recombination velocity	cm/s
A	Area	cm^2
d	Distance	cm
AC	Alternating current	A
f	Frequency	Hz
ω	Angular frequency	
V_{DC}	Bias voltage	V
C	Capacitance	C
G	Conductance	S
χ_S	Electron affinity	eV
V_D	Dielectric voltage	V
φ_m	Work function of a metal	eV
φ_{ms}	Metal semiconductor work function	eV
Q_{eff}	Effective oxide charge	$q\ cm^{-2}$
V_{FB}	Flatband voltage	V
ε_S	Permittivity of the semiconductor	F/m
ε_0	Permittivity of vacuum	F/m
k_S	Dielectric constant of the semiconductor	-
L_D	Debye length	cm
MCD	Minority carrier density	cm^{-3}

List of Acronyms

Acronym	Description
Al_2O_3	Aluminium oxide
ALD	Atomic layer deposition
ALD-Al_2O_3	Atomic layer deposition aluminum oxide
BSF	Back surface field
C-V	Capacitance-Voltage
Cz	Czochralski
CIGS	Copper indium gallium selenide
CdS	Cadmium sulfide
DC-Al_2O_3	Direct current-sputtered aluminum oxide
EQE	External quantum efficiency
FZ	Float-zone
FSF	Front surface field
FGA	Forming gas anneal
Ga	Gallium
G-V	Conductance-Voltage
G_p/ω	Parallel conductance normalized by frequency
HCL	Hole colloidal lithography

IQE	Internal quantum efficiency
NIL	Nano-imprint lithography
NP	Nano-particle
PC-1D	One-dimensional numerical semiconductor simulation program for personal computers
PECVD	Plasma-enhanced chemical vapour deposition
PERC	Passivated emitter rear cell
PERL	Passivated emitter rear locally diffused
PERT	Passivated emitter rear totally diffused
SCAPS	Solar Cell Capacitance Simulator
SRH	Shockley-Read-Hall
SR	Spectral response
SCR	Space charge region
SEM	Scanning electron microscopy
SLG	Soda lime glass
TOF-SIMS	Time of flight - Secondary ion mass spectrometry
T-SiO_2	Thermal silicon di-oxide
TEM	Transmission electron microscopy
XRF	X-ray fluoroscopy

Abstract

To address the challenges imposed by the highly recombinative CIGS/Mo interface in CIGS thin-film solar cells, this thesis work aims to obtain the fundamental understanding of the aluminum oxide (Al_2O_3) rear surface passivation effects and their impact on the CIGS solar cell performance. The main contributions of this thesis work includes:

(i) The development of high-quality industrially viable Al_2O_3 films using DC-sputtering technique. Obtained surface passivation results revealed extremely low effective surface recombination velocities < 7 cm/s (on p-type c-Si surfaces). Implementing these films in ultra-thin CIGS solar cells (as the rear surface passivation layer) demonstrate enhanced cell efficiency compared to the unpassivated reference cells.

(ii) The need for alternative surface passivation schemes while moving towards to ultra-thin (<400nm) CIGS solar cells has been qualitatively addressed using advanced opto-electrical characterization techniques. It was found that excess-gallium content within the CIGS absorber layers would increase the net deep-defect concentrations thereby increasing the absorber resistivity (within the active-region of the solar cell). Moreover, the effects of gallium grading can result in devastating cell results, particularly while considering CIGS absorber-thickness in the range of 300-400nm, due to optimal notch position within/near the space charge region (~250nm) thereby resulting in almost flat profiles (i.e. flat conduction band).

(iii) As a first attempt to reduce the rear surface recombination rates at the highly recombinative CIGS/Mo interface, we have introduced highly-acclaimed atomic-layer-deposition (ALD) and less commonly used direct current (DC) - sputtered Al_2O_3 films as the rear surface passivation layer in ultra-thin CIGS solar cells. The resulting experimental cell results demonstrate an absolute increase of 4.5% in efficiency for cells with rear surface passivation concept compared to the unpassivated reference cells. Such an improvement in cell efficiencies for rear-passivated cells can be attributed to the increased rear surface reflection in combination with the reduced recombination losses.

(iv) In-depth investigation of the CIGS/Al_2O_3 interface electronic properties by using extensive electrical characterization on Al/ALD-Al_2O_3/CIGS/Mo (Metal-Insulator-Semiconductor) –structures. These results indicate that the as-deposited (AD) Al_2O_3 films exhibit positive fixed charges Q_f (approximately 10^{12} cm^{-2}), whereas the post-deposited annealed (PDA) Al_2O_3 films exhibit very high density of negative fixed charges Q_f (approximately 10^{13} cm^{-2}). The extracted interface state densities (D_{it}) values, which reflect the extent of chemical passivation, were found to be in a similar range of order (approximately 10^{12} cm^{-2} eV^{-1}) for both AD and PDA samples. Additionally, using the experimentally extracted Q_f and D_{it} mean values, SCAPS simulation results showed that the surface concentration of minority carriers (n_s) in the PDA films was approximately eight orders of magnitude lower than in the AD films

thereby reducing the effective surface recombination velocity to a great extent.

(v) Finally, in order to improve the understanding of Al_2O_3 passivation of CIGS surfaces we have developed a simplified 1D-SCAPS simulation model to address the fundamental passivation mechanisms involved, to interpret the impact of rear surface passivation concept on the cell performance for varying CIGS thickness and to generate theoretical "*golden parameters*" for future experimental optimization.

Table of Contents

THESIS MOTIVATION

In order to position photovoltaics (PV) as the mainstream energy generation technology, it is necessary to further reduce the dollar per Watt peak ($/W) of the PV-modules (using mature technologies). This can be accomplished by reducing the usage of raw materials, increasing the cell performance by reducing the electronic recombination losses, implementing novel cell architectures, and by increasing the manufacturing throughput using industrially-viable cell processing techniques.

Recent research on high-efficiency PV cells is reviewed with a special focus on minimizing the electronic recombination losses in materials, interfaces, and devices. Therefore, effective surface-passivation schemes are necessary to avoid the large efficiency losses especially while scaling towards thinner absorber layers. To address these challenges the silicon PV-research community has carried out intensive research on the surface-passivation concepts for crystalline silicon (c-Si) photovoltaics. And the results demonstrated solar cell efficiencies greater than 22% with effective surface recombination velocities (SRV's) < $5cms^{-1}$.

On the other hand, there exists a wide gap in efficiencies (both at cell and module levels) between c-Si and other mature thin-film solar cells (for example $CuInGaSe_2$ (CIGS). Such a disparity in the cell performance in the latter technologies (CIGS) can be attributed to the polycrystalline nature and highly recombinative CIGS/Molybdenum (Mo) rear contact interface. Therefore, one possible way to enhance

the CIGS cell performance is to reduce the (CIGS/Mo) rear surface recombination. This can be accomplished by transferring the passivated rear point cell (PERC) concept from c-Si PV cell technologies to CIGS cell technologies. Therefore, within the frame of this thesis work, we aim to fill the technological gaps that exist between the c-Si and thin-film CIGS solar cells.

THESIS OUTLINE

Chapter 1: Provides a brief introduction on the current-state-of-the art surface passivation schemes both in silicon and thin-film CIGS solar cells and their corresponding cell efficiencies.

Chapter 2: Reviews the surface passivation quality of wide variety of passivation materials on p-type c-Si surfaces. Using capacitance/conductance voltage /frequency and minority carrier lifetime measurements, the interface electronic properties and surface passivation quality assessments were performed. Obtained results show good agreement with the state-of-the art literature reported values. Moreover, this chapter also provides the figure of merits in choosing the right passivation material based on their interface passivation properties (i.e. SRV, negative charge density ($Q_{f,}$), interface charge density (D_{it}) and the thermal stability), adaptability to thin-film CIGS (p-type) surfaces, deposition conditions (i.e. deposition temperatures) and industrial viability (i.e. deposition rates) for large-scale production.

Chapter 3: Addresses the viability, quality and thermal stability of aluminum oxide films deposited by DC-sputtering technique. Experimental results were evaluated both in terms of the surface passivation properties and thermal stability. We show that DC-sputtered Al_2O_3 films are capable of achieving high density of negative fixed charges ($Q_f \sim 10^{11}$-10^{13} cm^{-2}) in combination with extremely low interface trap densities ($D_{it} \sim 10^{10}$-10^{11} $cm^{-2}.eV^{-1}$) upon high temperature post-deposition firing steps. Effective surface

recombination velocities < 7 cm/s and 11cm/s are achieved on 1-5 Ω.cm p-type c-Si surfaces for two different atmospheric conditions (N_2 and O_2) respectively.

We will also specify the sputtering requirements and post-deposition firing conditions to achieve these results. Local delamination "blistering" of the Al_2O_3 film takes places for films fired at temperatures greater than 600ºC in N_2 atmospheric conditions. Additionally, without the use of additional capping layers, we have proposed an alternative approach to avoid the blister formation by firing the films in O_2 atmospheric conditions. Experimental results reveal no blister formation for films fired at 600ºC (i.e. can withstand the 550ºC CIGS post-selenization step) in combination with excellent surface passivation quality makes the DC-sputtered Al_2O_3 films potential candidate for an industrially viable PercIGS concept realization.

Chapter 4: Provides a review on the conventionally used gallium (Ga) grading passivation schemes has been analyzed using advanced opto-electrical characterization techniques. After, a brief discussion on the benefits offered by the gallium grading on CIGS solar cell performance, we will discuss in-detail the complementary drawbacks offered by the Ga grading schemes. By using drive-level capacitance profiling (DLCP) and admittance spectroscopy (AS) analyses, we show the influence of Ga grading on the spatial variation of deep defects, free-carrier densities in the CIGS absorber, and their impact on the cell's open-circuit voltage V_{oc}. The parameter most

constraining the cell's V_{oc} is found to be the deep-defect density close to the space charge region (SCR). Moreover, experimental results also demonstrate that in compositionally graded devices, the free-carrier density in the absorber's bulk decreased in tandem with the ratio of gallium to gallium plus indium ratio GGI = Ga/(Ga + In), thereby increasing the activation energy, hindering the ionization of the defect states at room temperature and enhancing their role as recombination centers within the energy band. Furthermore, we anticipate that Ga-grading in ultra-thin (<400 nm) CIGS films will result in less effective electric-field passivation (i.e. flat conduction band due to uniform gallium content). Therefore, this void in the present research to passivate ultra-thin CIGS solar cells necessitates the need for alternative surface passivation concepts.

Chapter 5: Deals with the realization of the rear-passivated ultra-thin CIGS solar cells concept using two different Al_2O_3 deposition techniques (ALD and DC sputtering). The resulting cell results demonstrated an absolute increase of 4.5% (for both deposition techniques) in efficiency for cells with rear surface passivation concept compared to the unpassivated reference cells. This is followed by an in-depth investigation on the surface passivation effects of Al_2O_3 on CIGS surfaces using extensive capacitance-voltage-conductance measurements as a function of frequency and temperature on $Al/Al_2O_3/CIGS/Mo$ M-I-S structures. The extracted electronic properties were used in the 1-dimensional (D) simulation model that has been developed especially to address the impact of Al_2O_3 passivation on the CIGS cell performance. This step in the

simulation process has been strategically implemented by considering a simplified M-I-S structure (Al/ALD-Al_2O_3/CIGS/Mo) to validate the Al_2O_3 layer passivation effects (i.e. field-effect and chemical passivation), followed by the introduction of the validated Al_2O_3 layer into complete CIGS solar cell structures. And the resulting cell efficiencies with Al_2O_3 rear passivation layer shows a significant gain (> 4% abs) when compared to the unpassivated cell structures, which is in good agreement with the experimentally obtained results.

CHAPTER 1: SURFACE PASSIVATION SCHEMES IN CRYSTALLINE SILICON AND CIGS SOLAR CELLS

1.1 Introduction

Currently the lion's share of crystalline silicon (c-Si) solar cell production is estimated to be around 90 percent with majority of the cell production being done industrially [1,2]. The reasons behind c-Si's dominance on the PV market are numerous, including a high module efficiency (13-20%), low manufacturing cost ($/Wp), an excellent long-term stability (>20 years) of the modules in the field, robust and high-yield wafer, cell and module fabrication processes, and material abundance and non-toxicity. Conversional efficiencies of industrial multi-crystalline, mono-crystalline solar cells are typically at 16.0 % and 22% respectively, while the laboratory-type cells are around 18.8% and 25.0 % respectively, more closely to the theoretical maximum of 29% (in the latter case). One of the major technical challenges, the solar cell research community has been facing over the past couple of decades is the issue of electronic recombination losses; which take place via defect states at the surfaces such as open dangling bonds, at the interfaces between two different materials, within the bulk of the absorbing material (impurities, deep–defect states, grain boundaries, material compositions), as well as due to the diffusion of other detrimental elements (such as C, Fe, Cr, Mg…etc.) during the high-temperature cell processing [1-6].

The dominant recombination mechanisms in mono-crystalline silicon, are due to *Auger and Shockley-Read-Hall (SRH)* mechanisms, the latter recombination mechanism is dominant and can be reduced by choosing the right doping concentrations and illumination conditions/injection levels (ex: concentrated solar cells), while the latter recombination mechanism can be manipulated and minimized by surface passivation of the open dangling bonds using appropriate dielectric layers [3,6,7].

In response to these challenges, very few industries in the past have been able to counter these effects with minimal success, experiencing and coming up with effective strategies to reduce its impact on the cell performances. Indeed, this could also explain the disparities in V_{oc} and cell efficiencies between laboratory and industrial cells until the year 2006 [3-5]. With these challenges in mind, significant research has been done on wide variety of dielectric materials and their combinations, to effectively passivate both front and rear surfaces of the c-Si solar cells [7].

Furthermore, a number of factors have been crucial in determining the quality and stability of the passivation schemes. Some include: (i) the optical properties, (ii) doping type of the silicon bulk, (iii) its stability and (iv) the processing conditions of the solar cell. Optical properties that are considered include the refractive index of the material as well as the absorption coefficient, and its sensitivity to UV light. The polarity (+ve/–ve) and density of the fixed charges existing within the bulk of dielectric films and their impact on the

surface carrier concentrations depending on the doping type (p/n) of silicon. Thermal (bulk degradation) as well as the long-term stability of the material includes: Hydrogen out-diffusion with time, oxide defect evolution, carrier injection into the dielectric layer resulting in charge to break down (QBD) of the dielectric [3,6,7]. And the solar cell processing factors includes: the thermal stability of the deposited films (delamination of the dielectric layer) under high temperature annealing steps, synthesis methods at disposal and the surface cleaning.

1.2 State-of-the-art surface passivation schemes in crystalline silicon solar cells

The first challenge with the solar cell production lies in the property of the absorbing semiconductor material used in the development. To date, the photovoltaic (PV) industry has many matured technologies based on variety of absorbing materials (Si, CIGS, CdTe, CIS... etc), amongst them silicon is lauded as the most suitable absorbing material due to (i) its overall good bandgap (1.1eV) match with the AM (air mass) 1.5 solar spectrum, (ii) its stability under light illumination and (iii) the purity of the material itself [7]. While the disadvantage factor lies in the fact that they are produced and processed under high thermal budget conditions, thickness, and complex advanced cell processing.

On the other hand, when it comes to the choice of dielectric layers to passivate these silicon surfaces, numerous dielectric materials have been considered and implemented based on their

interface passivation quality, optical absorptions, thermal stability, deposition temperatures, and industrial throughput [7,9]. Amongst the many available dielectric materials, one that has been widely accepted by both industrial and laboratory cells is the silicon nitride (a-SiN_x:H), due to its excellent anti-reflecting properties, high-temperature stability during screen printed metal-contact firings, low deposition temperatures and industrial suitability. Additionally, its usage also demonstrated good level of surface passivation both on n and p-type silicon surfaces due to the excess % of Hydrogen available for Si-OH interface dangling bond passivation [7,8,9].

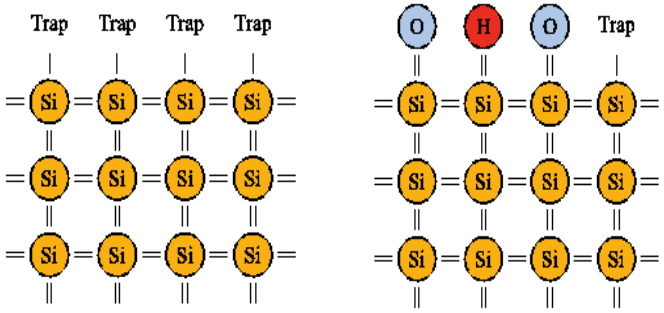

Fig 1.1: (a) Silicon surface (b) after hydrogen passivation [10]

The other form of Si that has been used widely in passivating silicon surfaces, not limited to PV technologies but also in microelectronic technologies is the thermally-grown silicon di-oxide (SiO_2) films. These dielectric films offer excellent surface passivation quality with extremely low surface recombination velocities (SRV) <30 cm/s attributed due to extremely low densities of interface states (D_{it} ~ 5-8 x 10^{10} eV^{-1} cm^{-2}). Additionally, these films exhibit very low positive

fixed charge (Q_f ~ 1-5 x 10^{10} cm^{-2}), thereby reducing unwanted parasitic junction formation beneath the silicon surface, thereby reducing the parasitic shunting of the metal contact during contact firing cell processing step. This makes SiO_2 as one of the most favorable candidate to passivate the silicon surfaces, yielding record cell efficiencies of 25% (laboratory developed) [4-9].

Although SiO_2 films demonstrated high surface passivation quality, many reasons have been put forward for its limited usage at industrial scale; one of the most important is that, requires, or indulges high temperatures. For instance, the multicrystalline silicon wafers are highly sensitive to thermal processes that involve temperatures above 900°C, eventually resulting in bulk lifetime degradation. For this reason most of the solar cell industries resort to use of passivation alternatives that entail the use of low-temperature surface passivation strategies to ensure high cell efficiencies [7-9]. Therefore, there exists a great need for low temperature surface passivation as an alternative. This lead to extensive research on the use of silicon nitride (SiN_x) as an alternative to the high temperature thermal oxidation, since it can be deposited by PECVD at temperatures below 400°C. However, with the use of SiN_x, it is observed that there exists a tendency of reduced fill factor (FF) and open circuit voltage (V_{oc}) of the solar cell in comparison to those fabricated with thermally grown SiO_2 as the rear surface passivation layer. Such an effect is due to the large density of the fixed positive charges (+ (1-5) x10^{12} cm^{-2}) that are found in the bulk of SiN_x films. This indeed will form an inversion layer at the P-type silicon surface (i.e. beneath the SiN_x). This inversion layer will

induce a floating junction (FJ) underneath the SiN_x films, thereby parasitic shunting (parallel low resistance path for the current, against the light induced solar cell junction current through the solar cell) with the rear metal contacts. Such parasitic effects have successfully been countered with the introduction of the negatively-charged aluminum oxide (Al_2O_3) layer, which has demonstrated excellent rear surface passivation quality on both n-type and p-type silicon surfaces [5-7,11].

1.3 Aluminum oxide (Al_2O_3) success on crystalline silicon solar cells

Over the years, the use of Al_2O_3 for surface passivation of both n and p-type silicon surfaces has proven convenient thanks to their low temperature deposition conditions, industrial feasibility by Spatial-ALD, PECVD, or DC/RF-sputtering techniques and their good surface passivation quality SRV~ 5-100 cm/s [11-13].

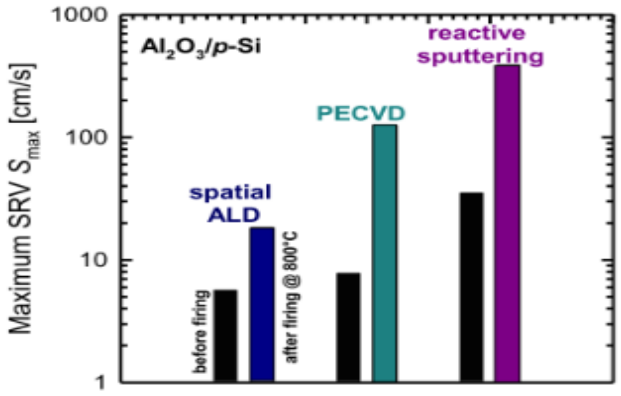

Fig 1.2: Effective surface recombination velocity (SRV) results for spatial ALD, PECVD and reactive sputtering on p-type Si wafers before and after firing [14]

Since the aluminum oxide (Al_2O_3) inception in 1989, when Hezel and Jaeger brought these films into limelight, it has not widely been considered as an alternative to conventional thermally grown SiO_2. Nevertheless over years, the use of Aluminum oxide (Al_2O_3) technology has been embraced and has gained the momentum and publicity, becoming one of the most preferred present choices [11]. After the initial reluctance towards the consideration of the Al_2O_3 passivation schemes, Hoex et al. reintroduced it using Atomic Layer Deposition (ALD) technique in year 2006 by demonstrating good level of passivation on n, p, and highly doped p+ silicon surfaces. And when it comes to cell level, an ultra-thin (10-30 nm) layer of Al_2O_3 films applied on silicon surfaces, demonstrated significant enhancement in the open-circuit voltage and thereby cell efficiency. ALD films are synthesized by alternate doses of process gases separated by a purging step. For the ALD deposition of Al_2O_3, the process gases consist of trimethly aluminium (TMA) and an oxidation step (H_2O, O_3, or an O_2-plasma). Until recently, ALD did not look like a viable technology for application in mass-scale manufacturing of silicon wafer solar cells, mainly due to its relatively low deposition rate (typically in the range of 1-2 nm/min) in the standard configuration that required purging between the two ALD steps. Recently, however, it was shown that this can be solved by moving from the time to the spatial domain for the dosing of the various process gasses resulting in depositions rates comparable to standard plasma enhanced chemical vapour deposition (PECVD), with deposition rates in the range of 1-5 nm/min. This non-contact method

has furthermore already been shown to be applicable to thin Si wafers with a thickness below 150 µm and handling of thinner wafers is expected to be feasible. The property that distinguished Al_2O_3 films in comparison to other conventional surface passivation dielectrics is its ability to induce field-effect passivation due to high density of negative fixed charges existing within the bulk of the dielectric films. Several explanations were given in the literature regarding the origin of these negative fixed charges and are still open to debate both in PV and microelectronic industry [11-15].

The extent to which Al_2O_3 passivation has been accepted in the PV industry is clearly demonstrated by the fact that the conventional screen printed p-type Si solar cells with total Al-back surface field (Al-BSF) concepts in passivated emitter and rear totally diffused (PERT) cell architectures were replaced by the point local contacts (PERC) through the Al_2O_3 dielectric layers as shown in Figure 2(a) below.

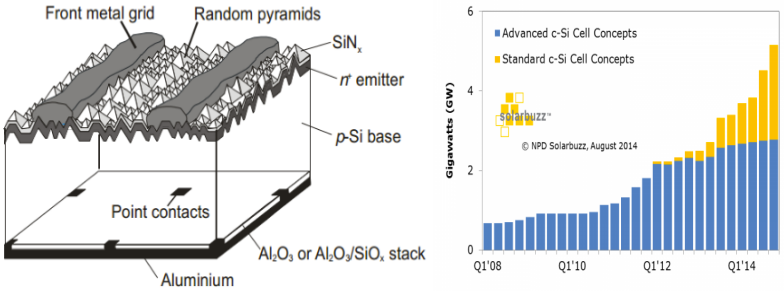

Fig 1.3: Rear passivated c-Si PERC (a) architecture and (b) its ramped capacity [15,16]

The above figure 2(b) shows the ramped annual c-Si PERC cell capacity that has passivation layers deployed on the rear side of the cell. The blue bar shows the thin/advanced c-Si cell capacity that uses rear side passivation by default. The upper yellow bar shows the PERC-specific capacity, mainly coming today from p-type mono c-Si cells. For instance, within just two years (2012-2014), 2.5GW of PERC-specific ramped annual capacity has been added. Collectively, approximately 10% of the effective c-Si cell capacity today has rear side passivation layers applied [15-17]. On the other hand for instance, when the standard full Al-BSF schemes are considered, it is observed that the rear internal reflection R_b and the rear surface recombination velocity S_b stands at 60 to 70% and 1×10^4 to 1×10^6 cm/s respectively. Under such opto-electronic conditions, reduction in wafer thickness also triggers a further decrease in the cell efficiency due to higher surface-to-volume ratio and significant loss in absorption due to low rear internal reflection [21,22]. In contrast, when the rear surface passivated cell designs are considered, the rear S_b is around 1×10^2 cm/s while the R_b stands at above 85%, which accounts for the enhanced efficiencies of the cells especially for thinner (50um-80um) Si wafers. This results in an enhanced short-circuit current density (J_{SC}) due to higher R_b, while on the other hand the fill factor FF may get reduced substantially as a result of the challenges offered by the point contacting schemes. However thanks to the absolute improvement of the rear surface passivation quality that resulted in a significant enhancement in the V_{oc} [11,17]. This indeed leverages dielectrically passivated rear surface concepts, that are meant to

minimize the surface recombination losses, concurrently enhancing the rear internal reflection (R_{back}) and minimizing the wafer bow due to thick metal especially for the thin wafers [20,21]. Hence, the need to adoption of thinner Si wafers and high efficiencies requirements leads to the success of Al_2O_3 films within the PV industry.

Al_2O_3 revelation also led to the re-introduction of ALD technique that is currently being used extensively in the high efficiency Si based industrial solar cell manufacturing [11-15]. The uniqueness of ALD unlike the plasma-enhanced conventional chemical methods of deposition (PECVD/PVD) is that ALD entails the use of precursor gases separated in two half-cycles when deposition causes self-limiting growth that occurs one layer (atomic thickness) after the other, leading to enhanced conformity and uniformity of precise thickness over larger surfaces. Moreover, Al_2O_3 thin films grown by ALD technique have shown better passivation results (SRV~5cm/s) compared to other deposition techniques such as plasma-enhanced chemical vapor deposition (SRV~100cm/s) and RF/DC reactive sputtering (SRV~30cm/s). ALD has emerged to be one of the most powerful techniques in thin film deposition and has been proven to be an attractive way in several PV applications. Aluminum oxide is able to achieve low SRV's due to both chemical passivation and field effect passivation on the silicon surface [14,15]. Chemical passivation, which could be compared to the thermal SiO_2 films, is responsible for the reduction of the interface defect density (D_{it}). On the other hand the dielectric films such as SiN_x and Al_2O_3 involve a high fixed charge density (Q_f), that will induce a built-in

electric field repelling one of the carrier types and reducing the overall surface recombination rate [9,11,15]. When it comes to p-type silicon surface passivation, PE- ALD Al_2O_3 is largely successful because it acquires a high density of negative $Q_f \sim 10^{13}$ cm^{-2} in combination with extremely low $D_{it} \sim 10^{11}$ eV^{-1} cm^{-2} after the annealing step at 430ºC for 30 minutes (activation step). More work in the same field have also shown that presence of fixed charge which occurs near the Al_2O_3/Si interface as a result of certain types of defects such as Al vacancies: interstitial H and, interstitial O located on the Al_2O_3 film or interface [9-15]. Hence, in order to achieve a breakthrough in terms of the next-generation industrial silicon solar cells with the highest possible efficiencies, one of the inevitable issues is to improve and enhance the surface passivation quality, to guarantee efficiencies above 20% on PV cells and modules [13,15].

1.4 Copper indium gallium (di) selenide (CIGS) thin-film solar cells

Despite the large market share of c-Si solar cells, thin-film solar cells based on hetero-junctions of direct band gap semiconductors, such as Copper indium gallium (di) selenide (CIGS), offer several advantages: less material consumption, wide range of deposition techniques, possibility to produce large areas in any shape or structure, lower cost per Watt, equal or even better theoretical efficiency of thin-film solar cells compared to other types of PV technologies. However, CIGS solar cells have a more complex material nature and requires rapid research and development growth to

meet their peak in technology, i.e. reaching optimal energy efficiency [23-25].

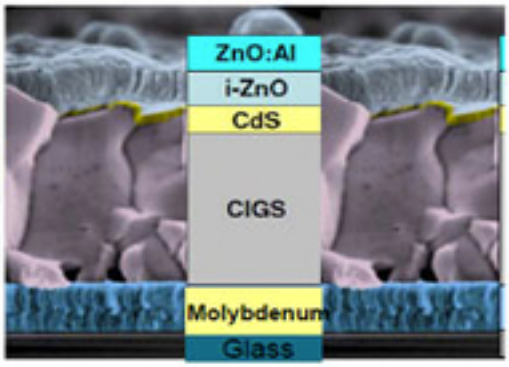

Fig 1.4: SEM image of Copper indium gallium (di) selenide (CIGS) solar cell [23]

In principle, the device structure of CIGS consists of five thin layers on a soda lime glass substrate, as depicted in Figure 1.4. Among several types of substrates used, soda lime glass (SLG) has been proven to be the most suitable one, since it has better match with Molybdenum (Mo) back contact, in terms of thermal expansion coefficient. It is also claimed that the sodium (Na) diffusion from the SLG (through Mo layer) into the CIGS absorber layer has a significant benefit on the overall cell performance. The effect is mostly related to passivation of grain boundary defects, increased carrier density, and crystal orientation change through the Na incorporation in CIGS layer [26-27]. Mo is generally chosen as a back contact of the solar cell, due to its good ohmic nature with the CIGS absorber layer (i.e. due to $MoSe_2$-layer formation during the selenization step). Cadmium sulfide

(CdS) buffer layer acts not only as a hetero-junction partner to CIGS layer, but also prevents oxidation of CIGS layer [28]. It is also responsible for band-gap alignment and lattice matching. Intrinsic ZnO's most important role as an additional buffer layer is believed to be reducing the shunt paths (pin-holes) between back and front contacts in CIGS devices. Al-doped ZnO acts as a front layer and TCO electrode (transparent and conducting oxide).

1.5 State-of-the-art passivation schemes in thin-film CIGS solar cells

CIGS solar cells are considered to be the best thin film absorbing material in terms of their excellent light-to-power conversion efficiencies exceeding 20%, although the efficiency has largely been affected or rather limited by the introduction and usage of gallium (Ga) as a means to develop a back surface field (BSF) [29]. With an estimated theoretical efficiency of around 29 percent in terms of conversion efficiency the material is one of the most embraced and used worldwide for the development of solar cells. Some of the manufacturers have been able to achieve very high efficiencies as a result of these. For instance the Swiss Federal Laboratories for Materials Science and Technology (EMPA) developed thin film CIGS solar cells with conversional efficiency of 20.4 percent while on the other hand Solar Frontier, a Japanese thin-film manufacturer developed a CIGS solar cell that was free of cadmium but with an efficiency that stood at 19.7 percent [24,25,30].

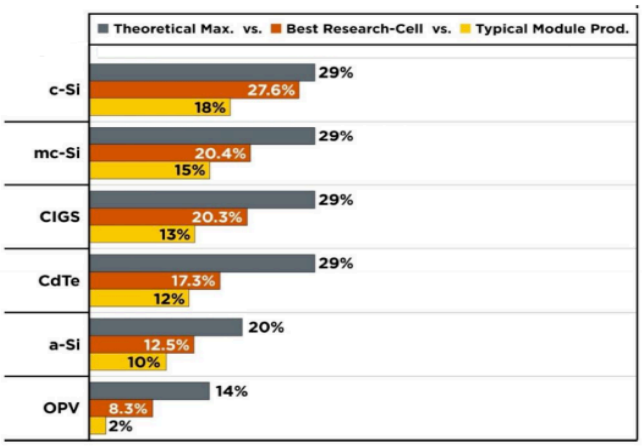

Fig 1.5: Status of cell efficiencies in the year 2014 for various PV technologies [31]

Similar to c-Si solar cells, the SRH recombination mechanism through defects is considered to be the dominant recombination mechanism in CIGS devices. However, compared to c-Si solar cells, the densities of defects within the bulk and interface of CIGS solar cells are orders of magnitude higher. The reason behind such high density of bulk defects within the CIGS absorber layer is due to the poly-crystalline nature of the layer. Fermi level pinning within the bandgap of CIGS absorbers is another severe problem that has been reported by many research groups. Under non-equilibrium conditions (i.e. room temperature/illumination), the quasi-Fermi level aligns with the high density of interface trap state energies (E_T) within the bandgap resulting in a significant loss in the cell's open circuit voltage due to recombination [29]. Apart from the naturally grown defects (poly-crystalline grain boundaries), other manufacturing defects

include; unwanted parasitic secondary phase formation ($MoSe_x$, $CuSe_{x...}$etc.), material compositional related defects (excess Cu, Ga within the space charge region), other interfaces related defect states due to (i) elemental diffusing of Fe, Mg, Cr, C..etc into the CIGS absorber film from the rigid glass/ flexible steel substrates during high-temperature (530ºC) selenization process step, (ii) Na, K, Cu, and O impurities segregation at the grain boundaries, surface states at the metal –semiconductor interface (i.e Mo/CIGS interfaces). As an attempt to reduce the concentration of these defects (both bulk and interface defects) within the CIGS material and at interfaces several research groups have come up with novel cell processing strategies. Amongst them are well known, (i) post Potassium induced alkaline treatment of the Cds/CIGS interface, (ii) conventional Ga grading surface field passivation and (iii) negatively charged Al_2O_3 rear surface field effect passivation [32].

1.5.1 Surface modification using alkaline post-deposition treatments

Potassium-induced surface modification technique proposed by the Twirai group at EMPA (Swiss Institute of Technology) has demonstrated a new sequential post-deposition treatment of the CIGS layer, with sodium and potassium fluoride that enables modified interface properties and mitigation of optical losses in the CdS buffer layer resulting in a remarkable conversion cell efficiency of 20.4 %. Solid-state ion exchange of Na with K within the CIGS film, Potassium fluoride-post deposition treatment (KF-PDT), are proposed to be the underlying mechanisms responsible for the surface

modification due to chemical composition of the deposited CIGS layer and interface properties of the heterojunction. This treatment eventually leads to a significant depletion of Cu and Ga concentrations in the CIGS near-surface region and enables a significant thickness reduction of the CdS buffer layer without the commonly observed losses in photovoltaic parameters [30].

1.5.2 Surface electric-field modification (passivation) using Gallium grading

Gallium grading at different depths within the bulk of CIGS layer is another surface passivation conventional strategy that has been in use by several research groups over many years. Very high efficiencies (upto 20%) at laboratory scale cells have been reported by varying the elemental ratios of Ga to Gallium plus Indium [GGI=([Ga]/([Ga]+[In])] from 0 to 1. This way the bandgap of CIGS can be adjusted approximately from 1.0eV to 1.7eV and the variation affects only the conduction bandedge of the bandgap. For desired field-effect passivation within the depth of CIGS absorber, the GGI ratios are altered at the (1) rear surface close to the Mo back contact, (2) near the space charge region (SCR) or (3) as a combination of front and rear surface. Variation of these GGI ratios is done in an effort to achieve higher bandgaps at different depths within the CIGS film. In an effort to suppress the effects of the carrier recombination at the surfaces, the ratios of GGI are monotonically increased at interfaces. Such an increase in the bandgap due to GGI varation at the front surface will benefit the decoupling of photo-generation and carrier recombination (FSF) at the CdS/CIGS interface, while GGI

ratio variation at the rear side of the solar cell will result in a gradient introducing quasi-electrical back surface field (BSF), which drifts the minority charge carriers away from the CIGS/Mo interface thereby reducing more effectively the rear surface recombination. The back-surface grading thus can improve the open- circuit voltage V_{oc}. It may also marginally increase the short-circuit current density J_{SC} thanks to an improvement in the carrier-collection probability close to the Mo rear contact. More detail, experimental results, and discussions on different Ga grading schemes are discussed in chapter 3 of this thesis [29].

1.5.3 Rear surface passivation of CIGS solar cells using Al_2O_3 films

Al_2O_3 rear surface passivation of CIGS solar cells is an alternative concept to reduce the amount of Gallium content usage to create back surface field. Although significant improvements in cell efficiencies were obtained using Ga-graded BSF schemes, the long-term stability of the Ga-rich solar cells is a major concern within the thin-film PV community. Since gallium by itself is consider as an impurity type, it will introduce new bulk-related defects within the bandgap and increase the bulk resistivity within the active region of the CIGS absorber. The mobility of free-carriers within this region is lowered due to the additional recombination centers (R-centers) introduced by gallium. The position of these R-centers with the bandgap will indeed decide the recombination rate and cell's open circuit voltage (V_{oc}). To counteract these negative effects of gallium grading with the CIGS films, at the same time providing adequate

back surface field to the minority carriers without being recombined at the CIGS/Mo interface, negatively charged Al_2O_3 films were introduced as the rear surface passivation layer with nano-sized contacts. This innovative approach will indeed reduce the surface recombination rate of the minority carriers at the CIGS/Mo back contact due to field effect passivation. This idea stems from the Si PV industry (PERC cell technology), where at the rear side of the advanced cell concepts consists of rear surface passivation layers combined with micron-sized point openings. More detailed information on the device fabrication, electrical characterization of the rear passivated CIGS solar cells with different passivation layer deposition techniques (ALD, DC/RF sputtered), dependence of cell efficiency on CIGS absorber thickness with rear Al_2O_3 layer, passivation, passivation quality analysis and the dominant passivation mechanisms involved are discussed in chapter 3, 4 and 5 of this thesis [32].

CHAPTER 2: QUANTIFICATION OF DIELECTRIC PROPERTIES FOR SILICON SURFACE PASSIVATION

This chapter critically evaluates the results obtained by analyzing the passivation quality of different dielectric layers on c-Si surfaces as well the thermal stability of industrially viable DC-Sputtered Al_2O_3 films. These results serve as figures of merit in choosing the best passivation materials and techniques for enhanced cell efficiencies. Additionally, we will also present different the electrical characterization techniques and methodologies used to extract the electronic properties at the c-Si/passivation layer interface. Furthermore, we will also discuss in detail, the correlation between the extracted electronic properties and the obtained injection dependent minority carrier lifetime (a) shape, (b) values, (c) dominant passivation mechanism involved and (d) the estimated SRV's.

In retrospect, materials such as SiO_2 have been used as passivation materials for crystalline silicon (c-Si). However, the major problem associated with the use of c-SiO_2 is the fact that it requires high-temperature processing that are above 900^{o}C resulting in silicon quality degradation and increasing processing costs. This implies that there exists a great need to adopt the use of passivation materials that can be deposited at considerably lower temperatures. For instance, one such material that can be used as a passivation material at low temperatures is the Hydrogenated amorphous silicon nitride (a-SiN*x*:H) which is obtained through the process of plasma-enhanced chemical vapour deposition (PECVD). The a-SiN*x*:H is normally used

as a front surface anti-reflection coating, emitter passivation (both n+, p+) and surface passivation (both n and p-type) [13,14,15].

2.1 Surface Passivation using Atomic Layer Deposited (ALD) Al_2O_3 films

Atomic layer deposited (ALD) aluminum oxide (Al_2O_3) has been widely used in the recent years as an effective material for surface passivation of both p-type and n-type c-silicon solar cells. The factors attributed to the excellent surface passivation quality are (i) *excellent interface chemical passivation (i.e. very low interface charges (*$D_{it} \sim \leq 10^{12}$ eV^{-1} cm^{-2}), in combination with the (ii) high density of negative fixed charges of $Q_f \sim 10^{12}$–10^{13} cm^{-2} *(i.e. field effect passivation)* resulting in extremely low surface recombination velocities (SRV< 5 cm/s). Moreover, ALD-Al_2O_3 is considered to be effective passivation films for both n-type and p-type surfaces including the surfaces that are highly doped with p+ emitters. Other factors that make the use of ALD technique more attractive over other deposition techniques include: good uniformity, controllability of thickness due to the self-limiting property (Angstrom/cycle), better step coverage (on rough surfaces like textured pyramids, nano-grass black silicon), good stoichiometry due to functional reactions, and relatively low deposition temperature (<300ºC). The above characteristics makes the ALD technique effective to passivate a wide range of solar cell architectures (PERC, IBC, EWT..etc) and technologies (wafer, thin film). The optimal surface passivation quality (SRV < 5 cm/s) on silicon surfaces were obtained through the use of plasma-ALD deposition mode, with passivation layer thickness

ranging from 10–25 nm at an average deposition temperature in between 150 to 200^0C, followed by an annealing step either in forming /nitrogen gas atmosphere at 430^0C for 30 minutes [33].

In the past many research groups have undertaken studies to understand and estimate the surface recombination rate (U_s) due to surface states using empirical approaches and scientific methods. Amongst them, Girisch, Mertens and De-Keersmaecker (1988) undertook a study to investigate the process of surface recombination by extending the Shockley-Read Hall (SRH) formalization to effectively model the surface recombination rates. In their study, Grish et al also investigated the effects of surface band bending due to fixed insulator charges (Q_f) and charged interface states (D_{it}=q*N_{it}). In general, these interface states are distributed with different trap energy levels (E_t) throughout the bandgap, i.e. D_{it} (E_t). We can relate the surface passivation of c-silicon surface with the extended SRH-recombination theory, since the interface states act as defect recombination centers. The overall surface recombination rate (U_s) can be estimated by integrating the interface state densities over the entire band gap [7, 12, 15, 17].

$$U_s = (n_s p_s - n_i^2) * \int_{Ev}^{Ec} \frac{v_{th} D_{it}(E_t) dE_t}{[n_s + n_1(E_t)]\sigma_p^{-1}(E_t) + [p_s + p_1(E_t)]\sigma_n^{-1}(E_t)} \qquad (2.1)$$

where v_{th} is the thermal velocity ; n_s and p_s are the surface concentrations of electrons and holes respectively; σ_n , σ_p are the capture cross-section of electrons and holes respectively; n_1 and

p_1 are equilibrium densities of electrons and holes when the Fermi level (E_f) coincides with the trap energy level (E_t) as defined by;

$$n_1 = N_c \exp\left(-\frac{E_C - E_t}{kT}\right) \ , \ \ p_1 = N_v \exp\left(-\frac{E_t - E_v}{kT}\right) \qquad (2.2)$$

with N_c and N_v the effective densities of states in conduction and valence bands respectively.

Surface recombination rate (U_s) can be estimated by experimentally determining the surface parameters $D_{it}(E_t)$, $\sigma_n(E_t)$ and $\sigma_p(E_t)$ with their energy dependence, and parameters n_s and p_s. The former group of parameters can be obtained from the conductance method described below and the latter group can be estimated through PC-1D simulation by defining surface charge (extracted from the flat-band voltage (V_{fb}) of the experimental low-frequency C-V curve) on silicon surface and assuming a very high bulk lifetime (~10ms). This estimated surface recombination rate (U_s) could be fitted on the experimentally extracted SRV (from lifetime measurements) over a range of injection levels (Δn) [7,11]. Therefore, the surface recombination velocity (SRV) can be estimated at a particular injection level (Δn) of interest from equation (2.3)

$$\text{SRV} = \frac{U_s}{\Delta n} \qquad (2.3)$$

Recalling equation (2.1), the surface recombination rate (U_s) can be reduced by altering two fundamental mechanisms:

(i) Reducing the interface state densities D_{it} (i.e. Chemical passivation): The D_{it} is dependent on material and chemical processes used in the fabrication of the solar cell. For example its reduction can be realized by diffusing hydrogen into the silicon/dielectric interface to replace the dangling bond defects [7].

(ii) Reducing the surface concentration of minority carriers (i.e. Field-effect passivation): The surface recombination rate (U_S) can be reduced by decreasing one of two carrier concentrations at the silicon surface, typically the minority carrier concentration. This can be achieved by fixed charges existing in the dielectric layer. Specifically, these charges creates a built-in electric field which shields the minority carrier to be recombined at the surface by driving the device into accumulation or inversion modes depending on the charge sign (positive or negative) and the chosen substrate type [11-15].

In this chapter, we particularly lay emphasis on the surface passivation quality of different dielectrics films on p-type silicon surfaces. Amongst them include the conventionally grown/deposited positive fixed charge dielectrics namely thermal SiO_2, PECVD-SiO_2 and a-SiNx:H, negative fixed charges dielectric Al_2O_3 films deposited by thermal and plasma–ALD, and DC/RF sputtering techniques. After a general introduction about the surface passivation mechanism in Section 2.1, we describe the fabrication steps involved to fabricate metal insulator semiconductor (MIS) capacitor and lifetime sample preparations to perform opto-electrical characterizations on the above-considered dielectric films in Section 2.2. Next, in order to quantify

the passivation quality of these dielectric films on silicon surfaces, detailed electrical characterizations, parameter extractions (i.e. Q_f , D_{it}) and the passivation quality (i.e. SRV and lifetime) results were discussed in Section 2.3 and 2.4 respectively. Followed by experimental results, discussions on the (i) nature of interface passivation involved, (ii) the impact of naturally grown interfacial-SiO_2 layer (1-2 nm) on the field-effect passivation were presented in Section 2.5. Finally, the surface passivation quality and thermal stability analysis of DC-sputtered Al_2O_3 films were discussed in Section 2.6 of this chapter.

2.2 Methodology

2.2.1 Characterization and fabrication of samples

It clearly appears from equations (2.1) and (2.2), that insight knowledge about the density of interface states (D_{it}) and surface concentrations of carrier ns, ps (which depend on Q_f) gives in-depth information about the interface passivation quality of each dielectric film. To extract these values we have considered MIS capacitors as test vehicle [33].

2.2.2 Dielectric films deposition

As a reference, thermal SiO_2 was prepared up to a 20nm thickness at a temperature of 1050ºC in an atmosphere that contained ultra-dry oxygen through the use of a vertical thermal furnace from Koyo Thermo Systems for a duration of 15 min. 20 nm-thick PECVD SiO_2 layers were deposited in a parallel plate reactor from Oxford

Plasmalab system-100. The deposition parameters used during the film growth were: chamber pressure 0.8 Torr, deposition temperature 300°C, gas flow: SiH_4-500 sccm, N_2O-20 sccm and O_2-5 sccm. PECVD a-SiNx:H 20 nm-thick layers were also deposited using the same Plasmalab system-100. However, in this case silane (SiH_4) and ammonia (NH_3) were used as reactive gases in the chamber. During the deposition process, SiH_4 was diluted to 5% in pure nitrogen (N_2). The deposition parameters used for the PECVD a-SiNx:H film growth are: chamber pressure 0.8 Torr, deposition temperature 300°C, radio frequency (RF) power 20 W, plasma frequency 13.56 MHz, gas flow: NH_3-1.8 sccm, SiH_4-10 sccm, and N_2-700 sccm [34-38].

Regarding Al_2O_3, 15 nm thick layers were deposited through the use of plasma enhanced atomic layer deposition (PE-ALD) and thermal-atomic layer deposition (T-ALD) modes. In both modes, the deposition was performed at a temperature of 250^0C. Argon was used as the carrier gas in the deposition chamber using both techniques. Moreover, before the deposition process, all experimental samples were kept in the deposition chamber for almost 1800 seconds in order to pump away oxygen and water. The TMA pulse duration was 10 seconds while the TMA pulse duration for T-ALD was 0.06 seconds. In the T-ALD mode, the precursor deionization element is water while for PE-ALD mode, the deionization element was oxygen. Moreover, from the experimental analysis during the deposition process, the observed flow was estimated to be 30 sccm and the plasma power at 300 W. The purge time of the plasma was estimated at 5 seconds while the pulse duration of the plasma was estimated at 20s. Moreover,

from the experimental analysis that was undertaken, the growth rate was estimated at 1A per cycle in both experiments that involved the T-ALD and the PE-ALD. All these steps are depicted in Fig. 2.1 [11-15,39,40].

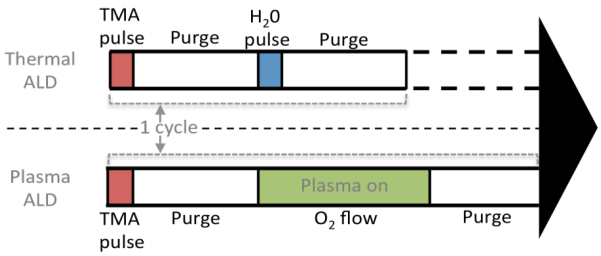

Fig 2.1: Schematic view of the ALD cycle. Firstly, TMA is pulsed and a purge time is performed to pump away the reaction products and residual TMA. Secondly, water is pulsed in case of thermal ALD. For PE-ALD, remote oxygen plasma is activated. Finally, purge time is performed for the same purpose that before.

2.2.3 C-V-G measurements and device fabrication

Fabrication of the MIS capacitors was undertaken on p-type silicon wafers with resistivity ranging from 1- 3 Ohm.cm as shown in Figure 2.2.

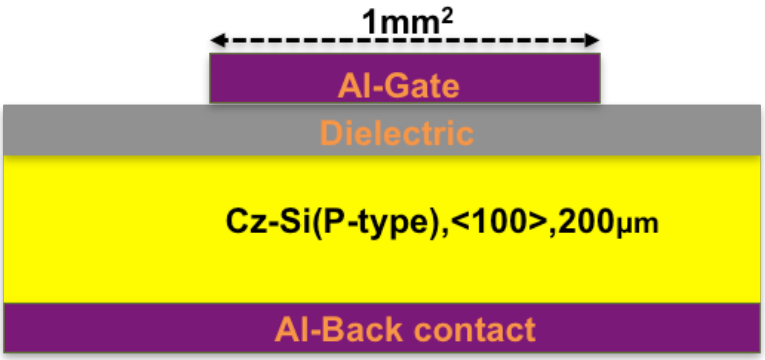

Fig 2.2: MIS capacitor schematic diagram

Piranha solution (3:1:H_2SO_4: H_2O_2), was used to clean the wafers before the deposition process. The cleaning of the wafers was undertaken for a period of 20 minutes at a temperature of 120 ^{0}C. In order to remove the native oxide, the wafers were dipped in dilute 2% HF solution at room temperature. After removal of the native oxide, the dielectric materials used in the experiments were deposited, after which the gate electrodes with an active area of approximately 1 mm^2 were patterned on the front side using image reversal lithography. A 300 nm Al layer was evaporated on the front side of the samples followed by a lift-off in acetone. After front-side device fabrication, full-area aluminum back contact (300 nm) is evaporated on the backside of the wafers. Finally, all the samples were annealed in forming gas (N_2/H_2: 90/10%) ambient at 432ºC for 30 min.

2.2.4 Sample preparation for lifetime measurements

In order to focus and comment on the involved passivation quality of each dielectric material, the lifetime samples were prepared using boron doped p-type, double side polished, 200µm thick silicon

wafers. Moreover, wafers of high resistance (> 5000 Ohm.cm) were intentionally selected; in order to avoid unwanted bandgap related defects that are induced by the excess impurity dopants. In essence, the above impurity dopants act as effective recombination centers for SRH. For instance, the concentration of the dopant impurities sets the Fermi levels, and that materials with low resistivity are considered to be quite sensitive to these defects as opposed to materials that have high resistivity (HR). This implies that the dominant bulk recombination in HR samples is as a result of radiative and Auger mechanisms [11,14,26]. In these experiments, lifetime measurements were undertaken through the use of Sinton WCT-120 lifetime tester in both the transient and quasi steady states. In that case, the various dielectric layers (considered above) were deposited on both sides of the wafers, followed by thermal annealing process in forming gas atmosphere at 432 ºC for a duration of approximately 30 minutes to activate the passivation mechanism [6,7,39-41].

2.3 Analysis of key findings using different dielectric materials

The C-V characteristics of MOS capacitors measured at 10 kHz for the different dielectrics under consideration are shown in Figure 2.2. The flat-band voltage V_{fb} of the low frequency (10kHz) C-V curves enables us to determine the density and polarity of fixed charges present in the dielectric film with the following equation:

$$Q_f = (\Phi_{ms} - V_{fb})\, C_{oxide}$$

where Φ_{ms}= -0.96 is the difference between the silicon and aluminum work functions.

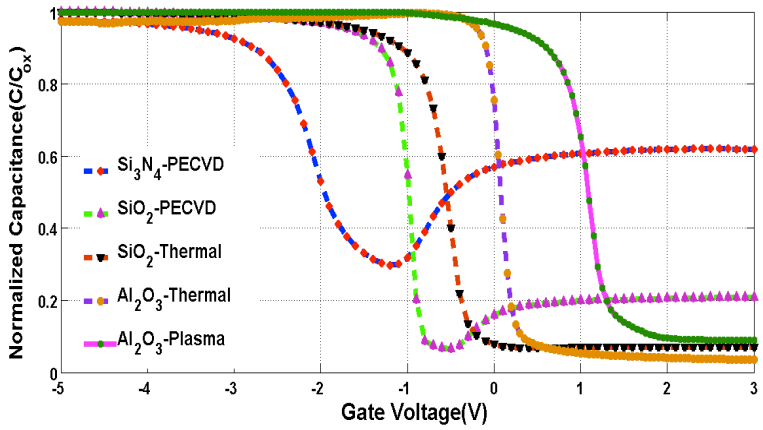

Fig 2.2: 10kHz C-V characteristics of MIS capacitors for various dielectric films

For instance from Fig 2.2, the flat-band voltage (V_{fb}) of the MOS capacitors with the PECVD Si_3N_4, PECVD SiO_2 and thermal SiO_2 films is negative (i.e. lower than Φ_{ms}), meaning that these films contain fixed positive charges (Q_f). Whereas for the T -ALD and PE-ALD Al_2O_3 films, the V_{fb} is observed to be positive meaning a negative Q_f in the bulk of the films [42,43].

2.3.1 Methodologies for interface states density extraction

Extracting the interface state densities (D_{it}) using a single method may in most cases yield inaccuracies, due to internal parasitic effects originating from the device under test (DUT) such as inappropriate surface band bending, surface doping concentration, high leakage currents through the dielectric films and external

parasitic effects due to the electrical characterization–set up that include, series resistance from the measurement set up (i.e cables, probe tips...), dielectric charging/discharging due to parasitic light illuminations as well as the frequency dispersion problems due to temperature variations. These parasitic effects will indeed affect the measured capacitance-conductance (C-G) data, and may eventually affect the extracted D_{it} values by to an order of magnitude. In order to extract the D_{it} values with confidence and to propose a range of values as a figure of merit for each dielectric under test, we have considered three different D_{it} extraction methodologies as described below. Prior to the D_{it} extractions, parasitic series-resistance correction using dual-frequency five element MOS capacitor small-signal model was performed on the C-V-G data [please see Appendix A and 43-45].

I. The first method involved the extraction of the D_{it} using the high-low frequency method. As illustrated in the figure 2.3.1 (below), the methodology involves the comparison of the quasi-static (typically 1Hz) C-V curve with the high-frequency curve (1 MHz). In the quasi–static mode, the interface traps are assumed to follow the slow variations in the applied ac-signal, which contributes to the interface trap charge capacitance (C_{it}).

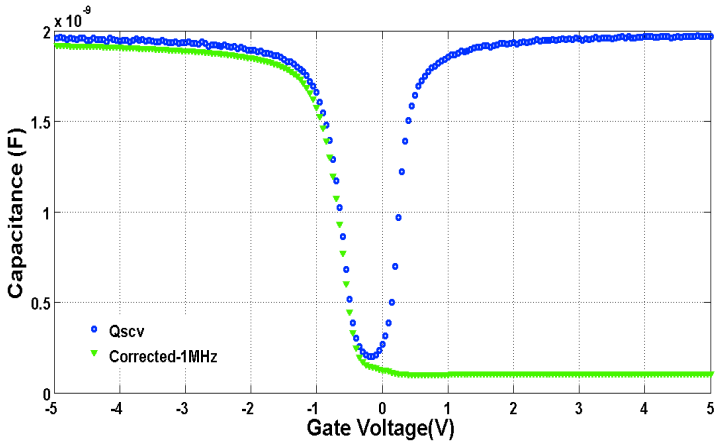

Fig 2.3.1: D_{it} extraction using high-low frequency method: here experimentally measured quasi-static (QSCV) and high frequency (HF) C-V curves of the MIS capacitor are compared in the depletion gate regime. The HF curve is represented after parasitic free (frequency- dispersion related problems in the accumulation gate voltages) correction using "dual-frequency five-element small-signal circuit model".

On the contrary, in the high-frequency measurement, the interface traps are assumed not capable of following the applied ac-signal, which in essence will result in a zero C_{it} capacitance. The value of the C_{it} is hence estimated by comparing the capacitance differences between the high frequency C-V curves and the quasi-static C-V curves in the depletion-inversion regions [44-51].

II. The second methodology involves the extraction of the D_{it} using the Terman method as shown in Fig. 2.3.2. In this method D_{it} extraction is based on the stretch-out phenomenon; i.e. the experimental high-frequency C-V curve is compared

to the theoretically simulated high-frequency C-V curve (i.e. ideal) with no interface traps (D_{it} =0). From the ideal C-V curve, one can find the surface potential (φ_S) for a given capacitance value within the depletion regime, and by interpolating it on to the experimental gate voltage (V_G) curve one can obtain the relation between surface potential and the gate voltage (φ_S–V_G). Repeating this process for other points from accumulation to inversion regimes results in a (φ_S–V_G) curve. Thus φ_S versus V_G curve will be stretched-out curve, when compared to theoretical curve with no D_{it}, this stretch-out yields the information about the interface state densities [43-45,52].

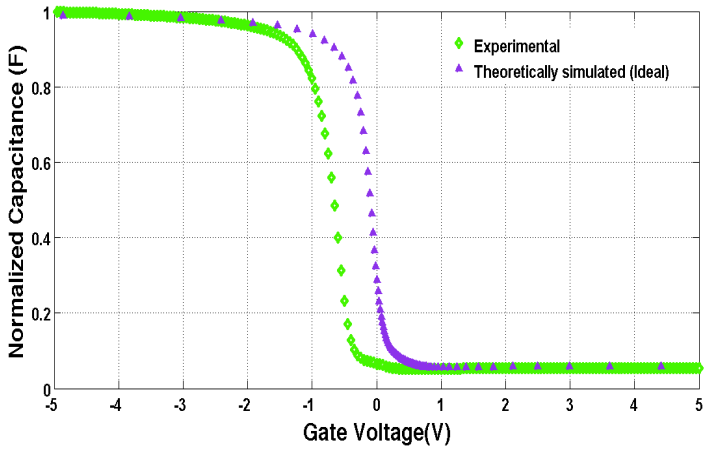

Fig 2.3.2: D_{it} extraction using high-low Terman method: here experimentally measured high frequency C-V curve is compared with a theoretically simulated 1MHz-C-V curve

III. The last method involves the use of the parallel conductance measurements in the extraction of the D_{it} values as illustrated in Fig 2.3.3 (below). Nicollian and Brew first proposed the method and it is considered to be the most accurate interface state extraction procedures within the range of ($8x10^{9}$ - $5x10^{13}$) cm^{-2} eV^{-1} [26]. Furthermore, the method is insensitive to then DUT parasitic effects, whereas strongly dependent on the series resistance (R_s) of the characterization set-up. The conductance methodology involves the extraction of the D_{it} values by measuring the equivalent parallel conductance per unit area (G_p), and is expressed as a function of frequencies and/or gate bias voltages. The equivalent parallel conductance peaks represents the loss in energy due to carrier emission and capture from the interface states. Plotting (G_p/ω) with respect to frequencies (ω) within the range of depletion gate voltages will yield a maximum in the energy loss mechanism (due to carrier exchange (charging and discharging phenomena) with the interface states. This peak (maximum energy loss) value of (G_p/ω) yields direct information on the amount of D_{it} involved [43-45,53-57].

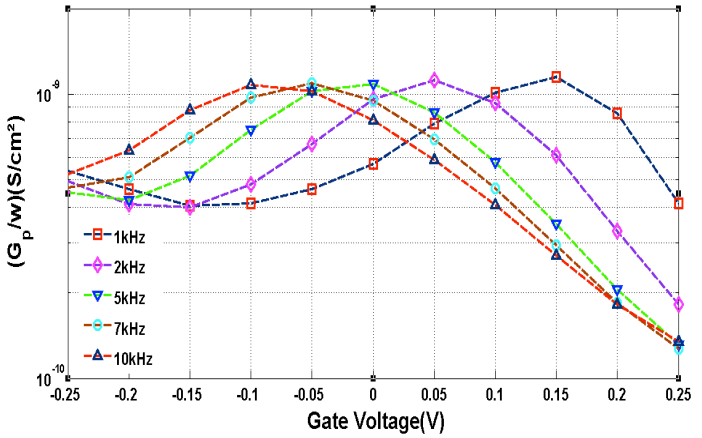

Fig 2.3.3: D_{it} extraction using conductance method: the maximum energy loss due to trapping/de-trapping mechanism at the interface (SiO_2/Si) were recorded by plotting parallel conductance (G_p) *as a function of depletion gate voltage (V_g) for given frequency (f)*

Furthermore, Table 2 (a) and 2 (b) presents the extracted values of accumulation capacitance (C_{ox}), flatband voltage (V_{fb}), fixed charge (Q_f) and interface trap density (D_{it}) from the C-V-G measurements on MIS capacitors with different dielectric films. Specifically, Table 2 (a) reveals that the PECVD-Si_3N_4 layer has a relatively high density of positive charges (~ + 4.2 x10^{12} cm $^{-2}$) comparatively to other dielectrics. On the other hand, Al_2O_3 dielectric films depicts negative fixed charge densities as high as -2.3 x 10^{12} cm^{-2} and -5.3 x 10^{12} cm^{-2} when deposited through the use of T-ALD and PE-ALD modes respectively. From the experimental analysis that was undertaken, Al_2O_3 deposited through the use of PE-ALD depicts high density of

negative fixed charges comparatively to the Al_2O_3 deposited through the use of T-ALD.

Table 2 (b) above summarizes the extracted values of the D_{it} using different methods. The differences in the D_{it} values can be attributed to the fact that the different methods used depict different sensitivities and specifications. Moreover, the variation in the D_{it} levels can be attributed to the fact that the results from each methodology are not extracted at the same depletion gate voltages. Moreover, other parasitic effects may affect the results such as inappropriate band bending in low-frequency measurements due to non-uniform doping of the substance. However, from the experimental analysis that was undertaken, the extracted values of D_{it} using the conductance method was slightly higher as a result of the asymmetry of the capture cross-sections (electron/holes) within the dielectric films [43,45].

Table 2 (a): Summary of the extracted values of fixed charge density (Q_f)

Dielectric layer	C_{oxide} *(F/cm²)*	V_{fb} *(V)*	Q_f *(cm⁻²)*	*Reported values [11-21]*
SiO_2 –Thermal (20 nm ± 1 nm)	1.7×10^{-7}	−1.0	$+(3.3-4.7)\times10^{10}$	$+(1-20)\times10^{10}$
SiO_2 –PECVD (20 nm ± 2 nm)	1.7×10^{-7}	−1.3	$+(2.3-3.9)\times10^{11}$	$+(1-10)\times10^{11}$
Si_3N_4 –PECVD (20 nm ± 2 nm)	3.0×10^{-7}	−3.0	$+(3.4-4.2)\times10^{12}$	$+(4-80)\times10^{11}$
Al_2O_3 –Thermal (15 nm ± 0.1 nm)	5.3×10^{-7}	−0.3	$-(2.1-2.3)\times10^{12}$	$-(3-50)\times10^{11}$
Al_2O_3 –Plasma (15 nm ± 0.1 nm)	5.3×10^{-7}	+0.6	$-(5.1-5.3)\times10^{12}$	$-(2-13)\times10^{12}$

Table 2 (b): Summary of the interface state densities (D_{it}) extractions using different methods from C-V-G measurements

Dielectric layer	*HF-LF* *($cm^{-2}\ eV^{-1}$)*	*Terman* *($cm^{-2}\ eV^{-1}$)*	*Conductance* *($cm^{-2}\ eV^{-1}$)*	*Reported values [11-21]*
SiO_2 –Thermal (20 nm ± 1 nm)	$(1.2-1.5)\times10^{10}$	$(1.1-2.2)\times10^{10}$	$(1.0-1.5)\times10^{10}$	$(1-10)\times10^{10}$
SiO_2 –PECVD (20 nm ± 2 nm)	$(2.5-2.9)\times10^{10}$	$(2.3-3.5)\times10^{10}$	$(2.2-3.2)\times10^{10}$	$(5-30)\times10^{10}$
Si_3N_4-PECVD (20 nm ± 2 nm)	$(1.3-1.7)\times10^{11}$	$(1.6-2.7)\times10^{11}$	$(1.3-2.4)\times10^{11}$	$(5-50)\times10^{10}$
Al_2O_3-Thermal (15 nm ± 0.1 nm)	$(1.1-1.2)\times10^{11}$	$(1.0-1.6)\times10^{11}$	$(1.9-2.3)\times10^{11}$	$(6-10)\times10^{10}$
Al_2O_3 –Plasma (15 nm ± 0.1 nm)	$(1.6-1.8)\times10^{11}$	$(1.7-2.1)\times10^{11}$	$(2.9-3.3)\times10^{11}$	$(8-20)\times10^{10}$

2.4 Minority carrier lifetime measurements

In order to quantify the effective carrier lifetime measurements of each dielectric layer under test, the dielectric films were deposited on both sides of the double side polished p-type c-silicon wafer to maintain structural symmetry. Obtained carrier lifetime results indicate good level of passivation quality that is independent of injection level for thermally grown SiO_2 on silicon surfaces. This can be attributed to the extremely low levels of D_{it} in the range of (1.2-1.5) x 10^{10} cm^{-2} eV^{-1}. Additionally, the quality of surface passivation is analyzed by effective surface recombination rates (SRV), estimated from the lifetime measurement curves at a particular injection level. For instance, in our experiments we have considered an injection level of $\Delta n = 5\times10^{15}$ cm^{-3} (within 1-sun AM1.5 spectral conditions) as a common injection point for the all dielectric films considered, for the sake of comparison purposes [11-15, 39-43].

$$\frac{1}{\tau_{eff}} = \frac{1}{\tau_{bulk}} + 2\left(\frac{S_{eff}}{W}\right) \qquad (2.4)$$

where W is the thickness of the substrate.

Assuming an infinite bulk lifetime due to the use of HR wafers, equation (2.4) can be simplified and the maximum $S_{eff_{max}}$ can be calculated by

$$S_{eff_{max}} \leq \left(\frac{W}{2\tau_{eff}}\right) \qquad (2.5)$$

the lower limit being the case when there is no recombination. In reality the value of S lies in-between ($0 < S < S_{eff_{max}}$) depending on the chosen injection level (Δn).

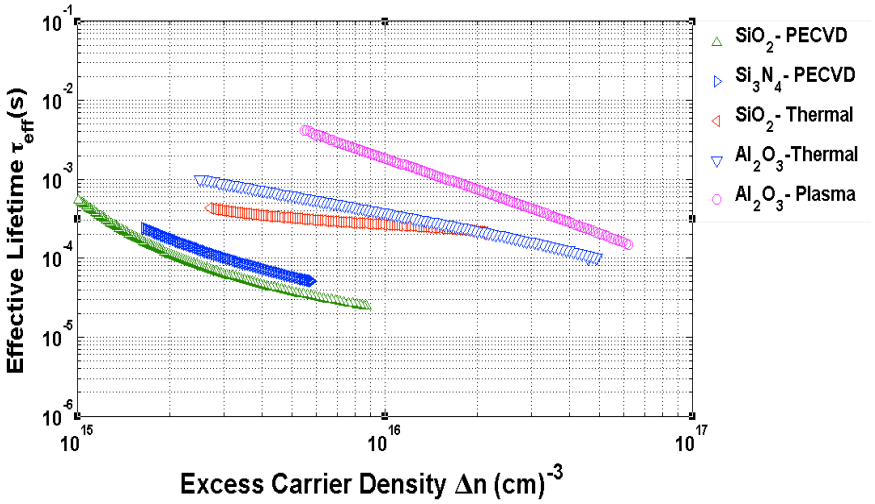

Figure 2.4: Injection-dependent effective minority carrier lifetime measurements for various dielectric materials

The corresponding SRV values extracted from the lifetime measurements with different dielectric films are given in Table 2(c).

Table 2 (c): Extracted τ_{eff}, $S_{eff,max}$ from various lifetime measurements at an injection point of $\Delta n = 5\times10^{15}$ cm^{-3}

Dielectric layer	τ_{eff} (Δn)	$S_{eff,\,max}$ (cm s^{-1})	***Reported values [11-21]*** $S_{eff,\,max}$ (cm s^{-1})
SiO_2 – Thermal (20 nm)	324	31	10-70
SiO_2 – PECVD (20 nm)	36	277	80-400
Si_3N_4 – PECVD (20 nm)	36	178	30-1000
Al_2O_3 – Thermal (15 nm)	613	17	5-30
Al_2O_3 – Plasma (15 nm)	3790	3	2-20

From Table 2(c), it can be observed that the samples with PE-ALD indicate the lowest SRV amongst the various dielectrics that were employed in our experiments. However, the samples with PE-ALD also indicated higher values of D_{it} from the C-V-G extraction procedures. On the other hand, T-ALD Al_2O_3 films on silicon surface also attained good level of surface passivation. Such level of surface passivation attained by the Al_2O_3 films can be attributed to the presence of high density of negative fixed charges (> 1x10^{12} cm^{-2}) within the films. This will eventually relax the detrimental effect of higher D_{it} at the silicon interface. The origin of these negative fixed charges in Al_2O_3 film is attributed to the trapped hydroxyl groups (OH) that were found at the $Si/SiO_X/Al_2O_3$ interfaces during the

deposition process [30]. Other reasons from the literature also include the presence of Al vacancies and oxygen interstitials within the bulk of Al_2O_3 films that are of acceptor type defects (-ve charged) [11-14,43-45]. The passivation mechanism of Al_2O_3 can be described as a combination of both chemical passivation (due to lower D_{it}) and field effect passivation (high $-Q_f$). Moreover, from the experimental analysis undertaken, it was observed that Al_2O_3 films like any other dielectric, will passivate the silicon dangling bonds chemically by releasing hydrogen atoms during the annealing process, thereby reducing the interface trap concentration. Additionally, due to the presence of high density of negative fixed charges within the bulk of Al_2O_3 films, field-effect passivation due to Coulomb repulsion will drive the silicon surface towards the accumulation mode (i.e. accumulation of holes and repulsion of electrons for p-type surfaces) creating a built in-electric field. This built-in electric field will indeed shield the minority carriers (electrons) from being recombining at the surface [13,15,40,43].

The field effect is more effective in the low injection regime, whereas at high injection, while photo-generated excess charges compensate the fixed charges that induced the field effect, and mainly the “chemical passivation” is dominant [43].

The shape of the $\tau(\Delta n)$ curves (Fig. 2e) can indeed reveal information regarding the involved interface passivation mechanism[43]. Moreover, in Fig 2.4 we can observe two distinct groups of curves, two lower curves corresponding to SiO_2 -PECVD and Si_3N_4 -PECVD and three others.

I. From table 2 (a) and 2 (b), T-ALD and PE-ALD Al_2O_3 layers have almost the same level of interface density $D_{it} \sim (1-3) \times 10^{11}$ $cm^{-2}eV^{-1}$. Thus the difference in lifetime behavior especially at lower injection range can be attributed to field passivation due to negative fixed charges. Comparing Q_f for the two Al_2O_3 deposition processes, PE-ALD ($Q_f \sim -5\times10^{12}$ cm^{-2}) is more efficient compared to T -ALD ($Q_f \sim -2 \times 10^{12}$ cm^{-2}).

II. On the other hand, PECVD $-Si_3N_4$ layers depicted poor chemical passivation ($D_{it} \sim 2 \times 10^{11}$ cm^{-2} eV^{-1}) in combination with higher density of positive fixed charges ($Q_f \sim + 4 \times 10^{12}$ cm^{-2}). The counter-field effect passivation due to positively fixed charges are considered to be less effective, in comparison to the field effect passivation due to negative fixed charges on the p-type substrates (i.e. the accumulation of majority carriers beneath the silicon surface due to negative charges is more efficient in reducing recombination, when compared to the inversion-layer that is being formed due to positive charges). This difference is attributed to the additional depletion layer that is being formed beneath the inversion layer (due to positive charges) where the hole (p_s) and electron (n_s) surface concentration achieve similar levels (max SRV point).

III. Furthermore, low fixed positive charges in PECVD-SiO_2 and thermally grown SiO_2 films will lead the silicon surface either into inversion or depletion mode and the resulting field effect

is not efficient. However, SiO_2-thermal lifetime curves exhibit almost injection independent behavior meaning that the dominant passivation mechanism involved at the interface is due to chemical passivation (i.e. lowest $D_{it} \sim 2\times10^{10}$ cm^{-2} eV^{-1}).

2.5 Dependency of field-effect passivation on the interfacial SiO_2 layer thickness

Kessels et al. [58] reported that a thin interfacial SiO_2 (~1−2 nm) layer is formed naturally between Si surface and Al_2O_3 layer. The thickness of this naturally formed SiO_2 is considered to be too thin to effectively passivate the interface states (i.e. the interfacial oxide may not necessarily produce the same quality as that produced by the thermal oxidation of Si surfaces). The purpose of my experiment is to chemically passivate the Si surface through thermal growing of the SiO_2 followed by thin ALD-layer deposition. This has been performed in order to effectively investigate the tradeoff between concurrent D_{it} and Q_f reductions through the introduction of thermally-grown SiO_2 layers with two different thickness of (8nm and 20 nm) [43,58].

A 15 nm thick layer of Al_2O_3 was deposited on the thermally grown SiO_2 (8nm and 20 nm) samples using PE-ALD mode. The deposition was also performed directly on the Si as a reference sample (i.e. no thermally grown SiO_2 layer). All the samples were treated under same annealing conditions as in the previous experiments on both C-V-G and lifetime measurement samples. The resulting SRV values demonstrated that the SiO_2 (8 nm)/Al_2O_3 (15 nm) stacks exhibit

lower SRV values comparatively to other samples [i.e. SiO_2 (20 nm)/Al_2O_3 (15 nm) and only Al_2O_3 (15 nm)].

The chemical passivation at the interface of Al_2O_3/Si occurs during the process of annealing, when a very thin interfacial Al_xSiO_y layer is created in between the two materials (Al_2O_3/Si). The formation of this thin interfacial layer is not well understood to date, however it was predicated that both oxygen and hydrogen play an important role in the formation of the surface hydroxyl groups (O-H) on the silicon surface, there by passivating the open dangling bond network.

In this direction of research work, the consequences of growing 8nm effective SiO_2 layer demonstrate positive impact on the overall reduction of the SRV~ 4 cm s^{-1}, and is solely attributed to one order of magnitude reduction in the electrically active interface traps D_{it} ~ (6.4−8.2)×10^{10} eV^{-1} cm^{-2} while subsequently maintaining adequate field effect passivation Q_f ~ − (3.9−4.4) × 10^{11} cm^{-2}. On the other hand, the reference sample (with only 15nm PE-ALD layers) exhibits positive V_{fb} and the corresponding Q_f and D_{it} values extracted from C-V-G are estimated to be around 8.5 × 10^{12} cm^{-2} and 2.7×10^{11} eV^{-1} cm^{-2} respectively. These results clearly indicate (see table 2d) that the extracted D_{it} values on reference samples are amongst the highest compared to other samples considered in our experiments. Nevertheless, extremely low SRV~ 9 cm. s^{-1} (from lifetime measurements) were still obtained, meaning that the field-effect passivation is predominant in reference samples and thereby relaxing the requirement for lower D_{it} values [43,58].

In comparison to reference sample, SiO_2 (8nm)/Al_2O_3 (15nm) samples, indicated negative fixed charges that were *twenty times lower*, while the obtained D_{it} values were *reduced by almost four times* as a result of the use of the 8nm thermal SiO_2 (which in essence reduces the defects). The reduction in the effective field effect passivation, while using 8nm SiO_2 layer can be explained from the fact that (i) the effective charge centroid in these samples were driven away from the silicon surface with increasing thickness of the SiO_2 and/ or (ii) due to the contribution of positive fixed charges ($+Q_f$) from the 8nm SiO_2 layer, reducing the net negative charge density. However, tradeoffs between D_{it} and Q_f obtained eventually leads to an effective reduction in the SRV at all the injection levels.

In case of the thicker SiO_2 (20nm) /Al_2O_3 (15 nm) samples, the quality of "chemical passivation" between Si and SiO_2 were similar to those obtained on SiO_2 (8 nm)/Al_2O_3 (15 nm) samples, while it can be observed (from Figure 2f) that the effective lifetimes were affected over the complete range of injection levels (injection-independent). This is underpinned by the C-V measurement, which indicate a reduction in the interface trap charge density ($D_{it} \sim 2.1 \times 10^{10}$) as well as the fixed charge density $Q_f - (1.4-2.2) \times 10^{11}$ cm^{-2}. Meaning that the effective field effect passivation due to negative fixed charges has been lost and that the only means of passivation in these samples is due to excellent chemical passivation.

Table 2 (d): Extracted parameters on SiO_2/Al_2O_3 stacks

Stack Type	$V_{fb}(V)$	$Q_{fixed}(cm^{-2})$	D_{it} $(cm^{-2}\ eV^{-1})$	τ_{eff} (μs)	$S_{eff,Max}$ $(cm\ s^{-1})$
Al_2O_3 (15nm± 0.1nm)	1.6	$-(8.3-8.7)\times10^{12}$	$(2.4-3.1)\times10^{11}$	1110	9
SiO_2 (8nm±1nm) + Al_2O_3 (15nm± 0.1nm)	−0.65	$-(3.9-4.4)\times10^{11}$	$(6.4-8.2)\times10^{10}$	2320	4
SiO_2 (20nm±1nm) + Al_2O_3 (15nm± 0.1nm)	−0.1	$-(1.4-2.2)\times10^{11}$	$(1.6-2.3)\times10^{10}$	316	32

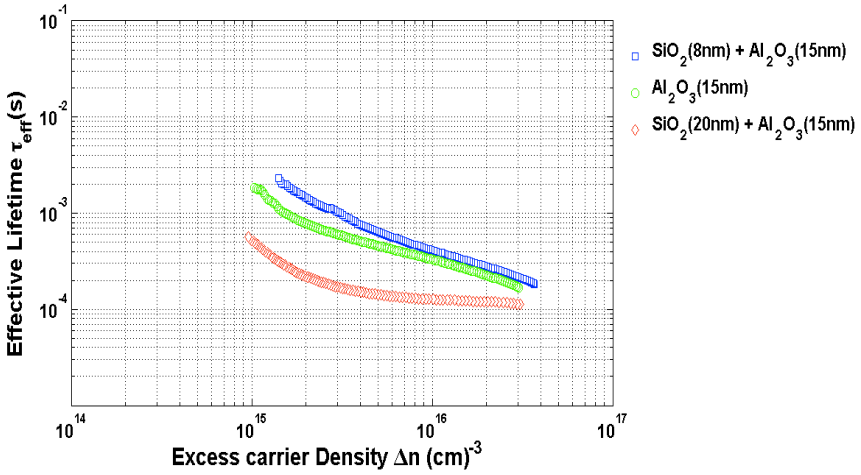

Figure 2.5: Injection-dependent effective minority carrier lifetime measurements on Al_2O_3/SiO_2 stacks

2.6 Summary

To summarize the obtained results, the electronic properties (Q_f, D_{it}) of different dielectrics were extracted using three different methods. In addition, parasitic C-V-G corrections were applied on the raw measurement data prior to the D_{it} extraction procedure for

accurate estimations. Extracted parameters were discussed and compared with lifetime measurements to understand the passivation mechanisms involved at the interface. In case of the PE-ALD Al_2O_3 layer, the extracted fixed charge density is negative (Q_f -5.2×10^{12} cm^{-2}), which provides an effective field-effect passivation by impeding the minority carriers from being recombined at the silicon surface. Extracted interface trap density (D_{it}) is found to be around 3×10^{11} cm^{-2} eV^{-1} as a mean value within the depletion gate-voltage range. Such high negative fixed charge density resulted in surface recombination velocity less than 3 cm s^{-1}, thanks to the formation of accumulation regime under the silicon surface.

Furthermore, the dependency of field-effect passivation on the thickness of SiO_2 interfacial layer has been studied. From the C-V-G parameter extractions and lifetime measurement results, it can be concluded that a SiO_2 (here 8 nm) reduces the interface state densities, while still maintaining adequate amount of field-effect passivation. Thicker SiO_2 layers (~20nm) will eventually reduce the net negative charge effect on the silicon surface and may even results in the loss of field-effect passivation. Finally, it was also observed that accumulation mode underneath the silicon surface will lead to better surface passivation than inversion mode (on p-type silicon surfaces). More generally, for any given dielectric film (with fixed charges), the field-effect passivation is predominant under low injection levels, while the chemical passivation at higher injection levels.

CHAPTER 3: SURFACE PASSIVATION AND THERMAL STABILITY ANALYSIS OF DC-SPUTTERED Al_2O_3 FILMS

3.1 Introduction

Despite the advantages associated with the use Atomic layer deposited (ALD) passivation schemes such as excellent surface passivation for both the *p* and *n* type c-Si solar cells due to low SRV as a result of high negative fixed charges and low density of interface states, the use of Al_2O_3-ALD technique is associated with various limitations. For instance, due to slow rates of deposition (1 Angstrom/cycle) and high cost of flammable precursors (TMA). However, the introduction of spatial- Al_2O_3-ALD deposition technique provides good level of surface passivation as well as industrial adaptability. As an alternative to ALD deposition technique, in this section, we will evaluate and quantify the passivation quality achieved by the use of DC (Direct current)-sputtered Al_2O_3 films on silicon surfaces (p-type here). This deposition technique offers cost-effective surface passivation technology with higher rates of deposition (7-10 nm/min) [59-63].

The second part of the experiment investigates the thermal stability analysis of DC sputtered -Al_2O_3 films, which involves high-temperature firing (600ºC-900ºC) of the deposited films. This has been carried out to (i) activate the passivation mechanism and (ii) study the resultant thermal stability of the films. The analysis involved a critical assessment on the formation, evolution of the blisters (i.e.

delamination of the film) as well as the influence of blisters on overall surface passivation quality [35,36]. Moreover, it's important to investigate the passivation quality and thermal stability of DC-sputtered films due to its process adaptability to thin-film solar cell processing (which will be discussed in detail in Chapter 4).

3.2 Sample preparations and Methodology

The experiment involved the deposition of DC sputtered aluminum oxide films on various batches of FZ p-type, 200µm silicon wafers, through the use of Al (99.9%) sputter target with Oxygen and Argon gas mixtures during the sputtering process. The aluminum target was sputtered with Oxygen (5 sccm) and argon gas (40 sccm) at a pressure of 1.5 mTorr. The experimental process involved the use of 120W DC power with a monitored current of approximately 300 mA. The deposition process was carried at room temperature. In order to perform the lifetime characterizations, the wafers were coated on both sides with Al_2O_3 with a thickness of 35nm to maintain symmetry, followed by forming gas anneal at 430ºC for a duration of 30 minutes to activate the interface passivation mechanism. The thermal stability analyses on annealed samples were carried out in two distinct atmospheric conditions (O_2 and N_2) at four different temperatures (T_1 = 600ºC, T_2 = 700ºC, T_3 = 800ºC, T_4 = 900ºC) for duration of 5 minutes [43-45].

The effective surface recombination rate was obtained through lifetime characterization of minority carriers through the use of Sinton W-120 in both quasi-static and transient modes. The corresponding electronic properties at the interfaces were evaluated using C-V

measurements. After performing the carrier lifetime measurements, same samples were used to realize M-I-S structures by removing the Al_2O_3 film on one side of the wafer using Hydroflouric (HF) acid to enable back contact for the mercury pobe (Hg) set-up, while the front gate-metal is realized by a 907μm diameter mercury dot. All the measurements were recorded using B1500A Agilent semiconductor analyzer [43,59].

The fixed charge densities were obtained from the flat-band voltage of low frequency (1kHz) C-V and the interface trap charge densities using high frequency (1MHz) C-V curve Terman method. Optical analyses on the fired samples were performed using Scanning Electron Microscopy (SEM) to study the evolution and growth of blisters under different firing temperatures and atmosphere conditions. Additionally, concentration depth profiling of the films were investigated using Time-Of-Flight Secondary-Ion-Mass-Spectroscopy (TOF-SIMS). TOF-SIMS sputtering was performed with Cs+ primary ion beam energy of less than 1keV [43-52].

3.3 Results and discussions

Figure 3.1(a, b) depicts the injection dependent minority carrier lifetime measurements performed on double side passivated FZ- c-Si, p-type, <100> samples using 35nm DC sputtered -Al_2O_3 films under different firing conditions (i.e. FG+N_2 and FG+O_2) and temperatures (i.e. To, T_1, T_2, T_3 and T_4). All the samples (#8) initially received a standard forming gas annealing at T_0 = 430 ^{0}C for a duration of 30 minute, followed by high-temperature firing (T_1-T_4) in N_2 or O_2 atmosphere and the obtained lifetime curves are shown in Fig

3.1(a, b) respectively. Furthermore, the extracted SRV values at Δn = $2x10^{15}$ cm^{-3} for both firing conditions were shown in Fig 3.1(c) [11-13,39-42,59-63].

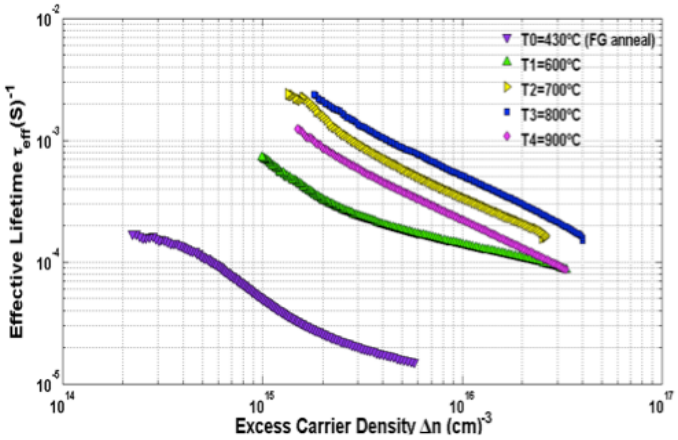

Fig 3.1(a): Injection dependent minority carrier lifetime measurements on the samples that underwent firing in N_2 atmosphere.

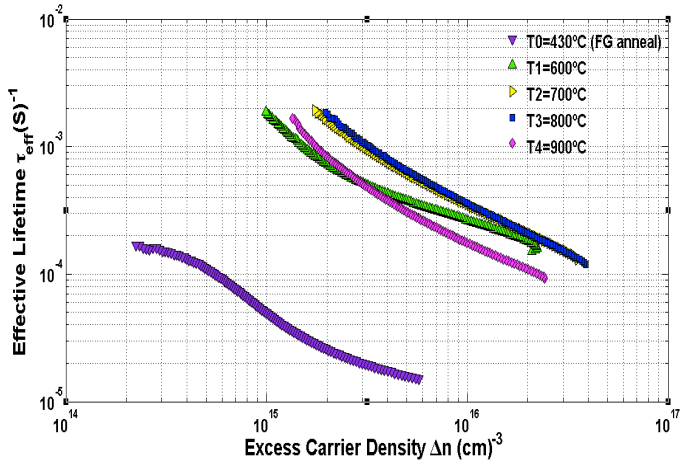

Fig 3.1(b): Injection dependent minority carrier lifetime measurements on the samples that underwent firing in O_2 atmosphere.

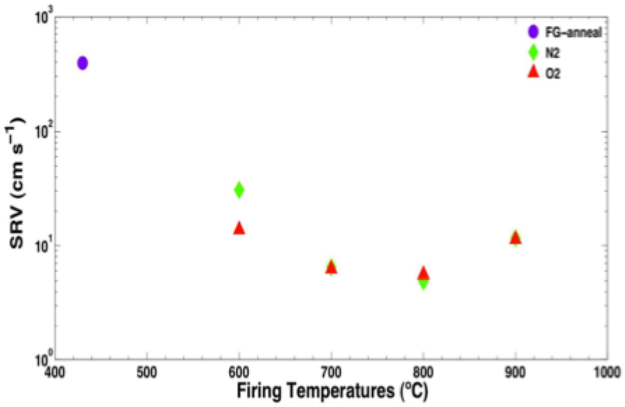

Fig 3.1(c): Estimated effective SRV values as function of firing temperatures at $\Delta n = 2 \times 10^{15}$ cm^{-3} for both atmospheric (N_2 and O_2) conditions.

These results clearly demonstrate: (i) poor passivation quality with an SRV~394 cm s^{-1} on the samples that received only FG-anneal. However, (ii) samples that have undergone high-temperature firing steps (700°C-900°C) for a duration of 4.5 minutes achieve excellent surface passivation quality SRV<10 cm s^{-1} for both N_2 and O_2 atmospheric conditions [59-64].

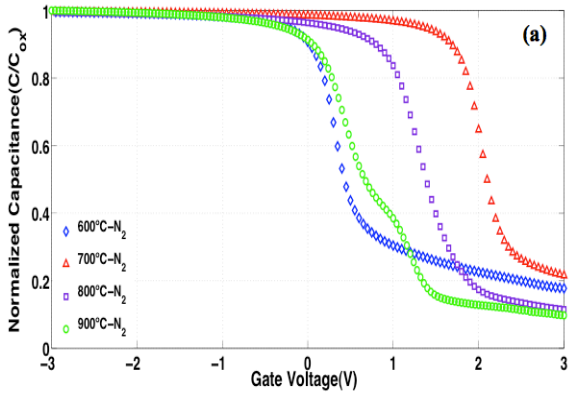

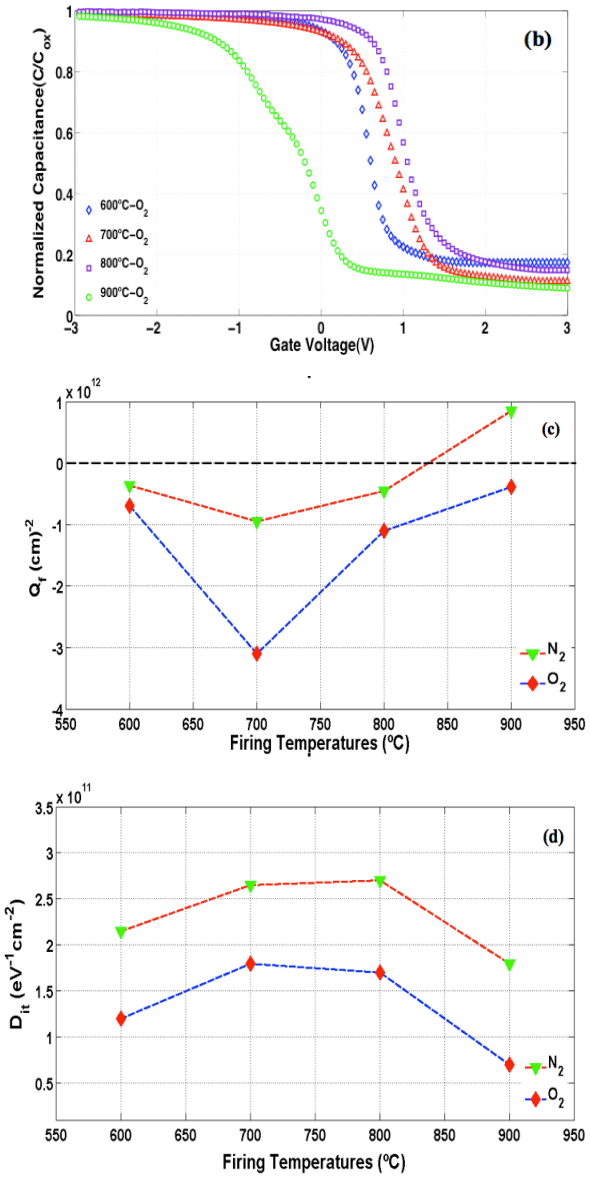

Fig 3.2 (a-d): shows the 1 MHz C-V characteristics after firing in (a) N_2 (b) O_2, (c) extracted Q_f and (d) D_{it} values vs firing temperatures under N_2 and O_2 atmospheric conditions.

C-V-G measurement results shown in Fig 3.2 (a-d) clearly demonstrates a positive flatband voltage (V_{fb}) shift trend (i.e. more negative fixed oxide charges) with increasing firing temperatures up to 800°C. Further increase in temperature (900ºC) lead to negative V_{fb} shift of the C-V curves (i.e. less negative or even positive charges). Samples that were fired at 600ºC in N_2 and O_2 exhibit almost same level of negative fixed charges in the range of $Q_f \sim -(3.4 - 6.1) \times 10^{11}$ cm^{-2}. While O_2 fired samples exhibit slightly lower $D_{it} \sim 1.2 \times 10^{11}$ $cm^{-2}eV^{-1}$ values compared to N_2 fired samples ($D_{it} \sim 2.5 \times 10^{11}$ $cm^{-2}eV^{-1}$), leading to excellent level of surface passivation quality with an SRV of 10 $cm.s^{-1}$ and 31 $cm.s^{-1}$ respectively. The D_{it} values extracted on the samples that were fired at 700°C and 800°C in N_2 exhibit similar range of values, but the density of negative fixed charges varies, being more negative at 700°C than 800°C. A similar trend was also observed for samples that were fired in O_2 atmosphere. More interesting results were observed on the samples that were fired at 900°C, the value of D_{it} being the lowest in both N_2 and O_2 cases, i.e. about 1.8×10^{11} $cm^{-2}eV^{-1}$ (in the case of N_2) and 8×10^{10} $cm^{-2}eV^{-1}$ (in the case of O_2). Such low D_{it} values will indeed promise a good level of interface chemical passivation at the Al_2O_3/Si interface. Nevertheless, the amount of net fixed negative charge densities reduces and even becomes positive ($Q_f \sim +8 \times 10^{11}$ cm^{-2}) in the case of O_2. Such reduction in Q_f can be explained by the fact that: the charge centroid in Al_2O_3 film is driven away from the silicon surface with increasing SiO_2 thickness (observed from TOF-SIMS) at the interface, as well as by the contribution of fixed positive charges in the

thermally-grown 5nm SiO_2 layer. However, the trade-off obtained between Q_f and D_{it} values at these firing conditions (N_2 and O_2 at 900ºC) still exhibited good passivation quality with SRV's ~12 $cm.s^{-1}$ solely attributed to the formation of interfacial SiO_2 layer (chemical passivation) [43,59,65-69]. Furthermore, to study the thermal stability properties of DC-sputtered Al_2O_3 films, we have intentionally performed a forming gas annealing step (containing 10% Hydrogen) at T_0=430ºC for a duration of 30 minutes to effectively passivate the open dangling bonds at Al_2O_3/SiO_2 interface [11-14]. Followed by this, a high-temperature firing step is performed in one of the two different atmospheric conditions (N_2 and O_2). During this high-temperature firing step, hydrogen within the bulk of Al_2O_3 film will diffuse to the silicon interface, thereby reducing the overall $D_{it.}$ This may also explain the reason for very low $D_{it} < 3x10^{11}$ $cm^{-2}eV^{-1}$ values obtained on fired samples. However, at firing temperatures >700°C, local delamination of the Al_2O_3 films also know as "blistering" takes place [58,59,66-68]. From the experimental SEM image analysis (see Fig 3.3 (a-f)), we can clearly observe that the blistering phenomenon takes place only in N_2 atmospheric conditions for temperatures beyond 700ºC, while no blisters formation is observed in O_2 atmospheric conditions even for relatively high temperatures (i.e. 900ºC). This confirms our hypothesis that oxygen plays a vital role in avoiding the blister formation mechanism and the interfacial OH groups play an important role in chemically passivating the surface silicon atoms. Furthermore, samples with blisters (fired in N_2-atmosphere) achieve the same level of passivation as that of without blisters (fired in O_2-

atmosphere), since no degradation in the minority carrier lifetimes were observed due to the formation of local blistering [58,59,67,68].

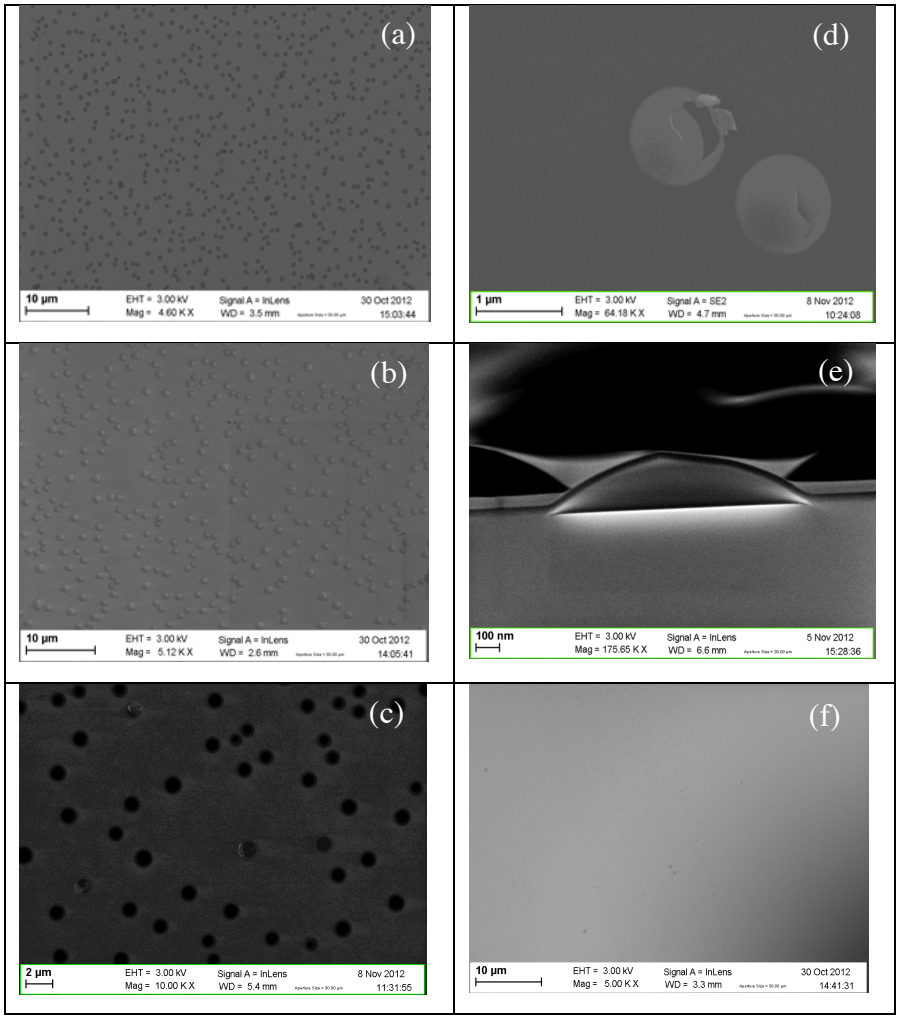

Fig 3.3: Scanning Electron Microscopy (SEM) images of the Al_2O_3 films fired in N_2 and O_2 atmosphere: Fired at (a) 700°- N_2 atmosphere (b) 800°- N_2 atmosphere (c) 900°- N_2 atmosphere (d) Delamination of Al_2O_3 film from the silicon surface when fired at 900°- N_2 atmosphere (e) Cross-sectional view of the blister (f) fired at 900°C- O_2 atmosphere.

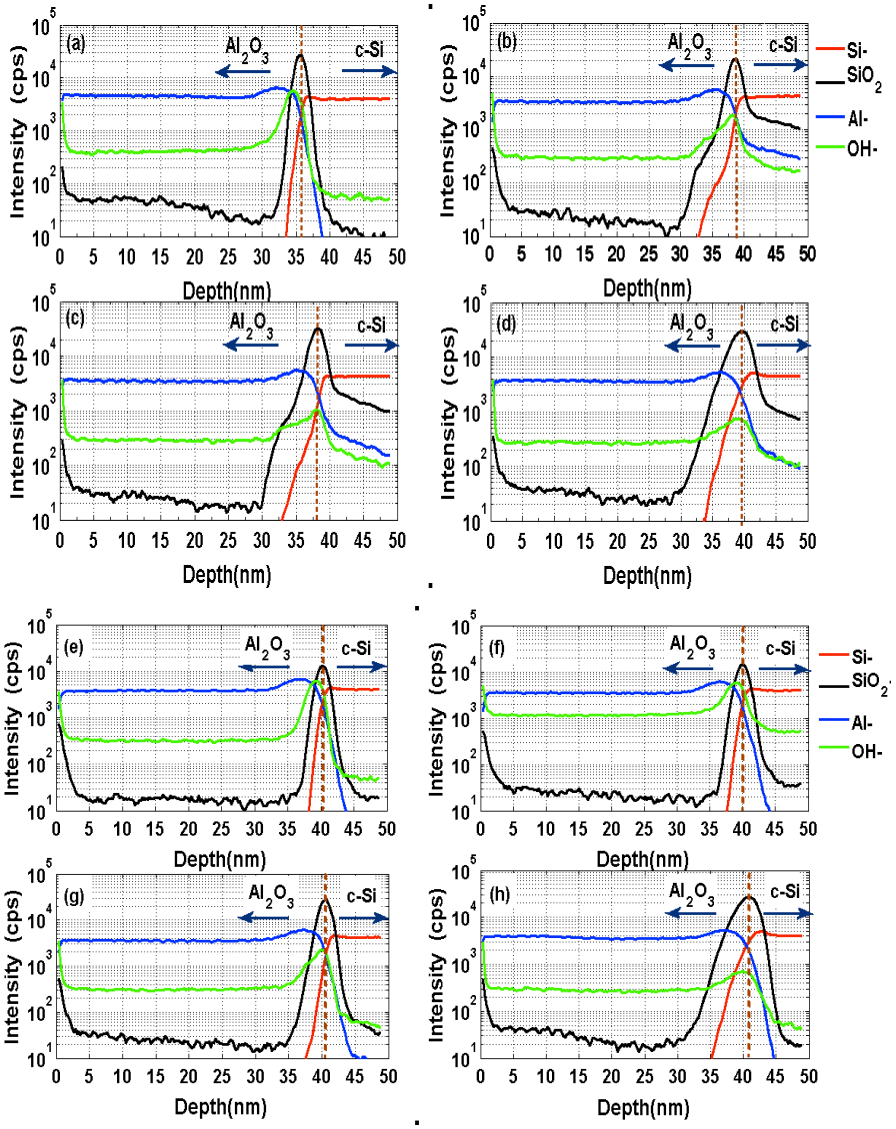

Figure 2.6.4 (a-h). The time of flight secondary Ion mass spectroscopy profiling of Al_2O_3 films depth fired at differed atmosphere and temperatures a. 600°- temperature and N_2 atmosphere (b) 700° temperature and N_2 atmosphere (c) 800° temperature and N_2 atmosphere (d) 900° temperature and N_2 atmosphere (e) 600° temperature and O_2 atmosphere (f) 700° temperature and O_2 atmosphere (g) 800° temperature and O_2 atmosphere (h) 900°-O_2 atmosphere.

To understand the involved passivation mechanism at the interface, Time-Of-Flight Secondary-Ion-Mass- Spectroscopy (TOF-SIMS) depth profiling was performed on all the samples and the depth scale origins from the Al_2O_3 surface. The TOF-SIMS indicated the presence of following elements in Al_2O_3 films among others: Si-, SiO_2-, Al-, OH-, O-, F-, C-. However, only relevant elements were shown in Figure 3.4 (a-h) for discussion [69-70].

Due to the energy of the Cs+ analysis ion beam and the sputtering yield versus element species, the quantification of the Al_2O_3 surfaces and interfaces are not calibrated for all the sputtered ions. Nevertheless, the location of the Al_2O_3/Si interfaces can be clearly seen from the abrupt change in the intensity. TOF-SIMS results show a higher concentration of hydroxyl groups (OH) present at the Al_2O_3/SiO_2 interface after the firing procedures, while its concentration decreases with increasing firing temperatures both in N_2 and O_2 samples. This could be due to silicon bonds breaking at high temperatures leading to out-diffusion of hydrogen element from the Al_2O_3 layer as atomic hydrogen (H°) or molecular hydrogen (H_2) [39,40]. Nevertheless, strong concentration of OH is still present at the interface under both atmospheric conditions (N_2, O_2) in all samples. The lower D_{it} ($<3x10^{11}$ $cm^{-2}eV^{-1}$) values obtained from C-V extractions on all fired samples suggest that the OH group existence at the interface is playing an important role in passivating the dangling bonds. Other interesting results observed from the TOF-SIMS include the interfacial oxidation of silicon with increasing temperature. The thickness of interfacial Al-Si-O_x layer formed during deposition is

typically 1-2 nm. However, upon high-temperature firing steps, the thickness of this layer is increased to 5nm (in the case of samples fired at 900°C in O_2) resulting in lowest D_{it} ~$8x10^{10}$ cm^{-2} eV^{-1} amongst all the samples [43,58,59,70,71].

3.4 Summary

To summarize, a detailed electrical and physical characterization was carried out on DC-sputtered Al_2O_3 films, in order to comment and quantify the surface passivation quality and its thermal stability properties. Experimental results showed that; samples annealed in FG followed by a high temperature firing step >700°C resulted in excellent silicon surface passivation. C-V measurement results shows high negative Q_f ~ -3.2 x 10^{12} cm^{-2} and low D_{it} ~ $2.8x10^{11}$ cm^{-2} eV^{-1} resulting in an SRV of 6.5 cm s^{-1} (for samples fired in N_2 atmosphere). Similar level of passivation is also achieved on samples fired in O_2 with Q_f ~ $-1x10^{12}$ cm^{-2} and D_{it} ~ $1.7x10^{11}$ $cm^{-2}eV^{-1}$. Furthermore, we propose an alternative solution to avoid the local delamination of the Al_2O_3 films by firing the samples in O_2 atmosphere, rather than using conventional PECVD-capping layer (Si_3N_4 or SiO_2) over Al_2O_3 films. From our experimental results, no significant influence of blister growth on the minority carrier lifetime was observed, since samples fired in both atmosphere (N_2 and O_2) exhibit the same effective lifetime. Current state of the art DC-sputtered Al_2O_3 films exhibit high-density of interface states (D_{it} > 10^{12} cm^{-2} eV^{-1}) with SRV > 30 cm s^{-1}. While, with our experimental approach and diagnosis, we have shown that the quality of these films can be largely improved by a subsequent firing step at higher temperatures either in N_2 or O_2

atmosphere conditions. The resulting surface passivation quality of DC-sputtered Al_2O_3 films with an overall SRV~ 6.5 cm s^{-1} can be well matched with those obtained by ALD deposition [61-71].

CHAPTER 4: SURFACE PASSIVATION OF CIGS SOLAR CELLS USING GALLIUM GRADING SCHEMES

4.1 Introduction

This chapter critically evaluates the effects of in-depth variation of the Ga/[Ga+In] ratios ("*also know as Ga-grading"*) on the copper indium gallium di-selenide (CIGS) solar cell performance. As discussed briefly in Section 1.5.2 of Chapter 1, depending on the Ga-grading concentration and profile, one can create and alter the built-in electric (E) field forces within the bulk of CIGS thin-films. And the electric-field creation/modification is mainly attributed to the reformed position (relative) of the conduction-band edge with respect to the vacuum level (i.e. bandgap engineering). In principle, to implement effective fields within the absorber films, it is necessary to tailor either the bandgap or the doping profiles [72-78]. In the former case, i.e. bandgap engineering towards the rear (CIGS/Mo back-contact) or front surface (CdS/CIGS) will create an up-stream (barrier) for the minority carriers (electrons) without being recombined at the surfaces (i.e. reducing the surface recombination rate). Hence, in order to understand the involved surface field modifications and there overall impact on the cell parameters (such as V_{oc}, J_{sc} FF and efficiency), we have considered CIGS-solar cells with three different Ga-profiles. Advanced electro-optical characterization techniques have been performed on these cells to evaluate the degree of positive and determinate effects (i.e. requirements for "notch" position

accuracy, creation of deep-defect states and free-carrier recombination) due to the use of gallium grading. And finally, we will summarize the Chapter by proposing an alternative approach for the effective passivation of the CIGS/Mo interface using negatively-charged ALD/DC-Al_2O_3 films, and their advantages compared to the conventional Ga-grading schemes.

4.2 Ga-grading schemes in CIGS solar cells

Over the span of the past two decades, many research groups have reported that the overall performances of the $Cu(In,Ga)Se_2$ cells can be significantly improved, when an optimized Ga-grading profile schemes were implemented compared to the ungraded profile schemes [72-78]. Ga-gradings in $CuIn_{1-x}Ga_xSe_2$ films are achieved by altering the in-depth variation of gallium to gallium plus indium ratio, GGI=Ga/(Ga+In) from 0 to 1, thereby resulting in a band-gap variation in the range from 1.04 to 1.67eV corresponding to the Ga content within the CIGS film [29,72-74]. For instance, Wei and Zunger [79] have theoretically (i.e. by using simulations) shown that the band-gap widening effect with increasing GGI ratio is mainly due to an increase in the conduction band minimum, with an estimated conduction band offset (ΔEc) of 0.6eV when increasing the GGI ratio from 0 to 1 (i.e. from CIS to CGS). In support to their work, several experimental and numerical simulation results also reported that the open circuit voltage (V_{oc}) increases for increasing GGI from 0 to 0.3 and high performance CIGS solar cells typically have a Ga content around GGI=0.3 [72-78]. However, further increase in GGI beyond 0.3 will result in a reduced cell performance, due to decreased short

circuit current and no further improvement in V_{oc} [29,75]. Additionally, many research groups working on CIGS bandgap modification through Ga-grading schemes have come up with different grading schemes. Amongst the many available schemes, in this Chapter we will focus and discuss the most widely used and accepted grading schemes and their reciprocity with the solar cell parameters. Those include: the (i) Uniform Grading (UG) profile, (ii) Back Surface Grading (BSG) profile (i.e. increase in GGI ratio towards the back surface) and (iii) Double Sided Grading (DSG) profile (i.e. increase in Ga ratio both towards back and front surfaces) as illustrated in Fig 4.1 below.

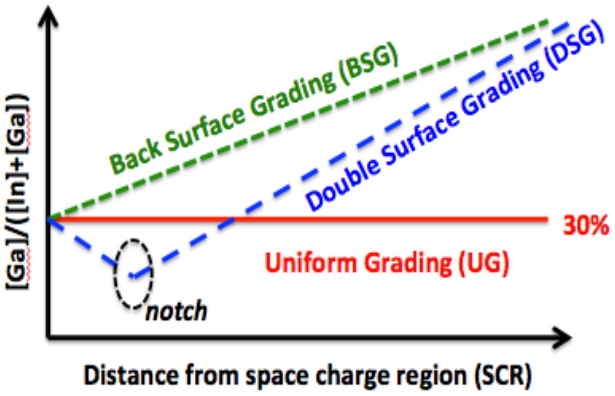

Figure 4.1: Gallium-grading schemes in CIGS absorber

Considering the case of UG profile schemes, the variation in GGI ratio throughout the CIGS absorber is kept constant (typically 30%). Hence, no localized electric fields will be formed (due to constant band-gap) to reduce the effective recombination unlike BSG or DSG schemes [73-76]. While in the case of BSG profiling schemes,

the band-gap is increased from front (SCR) to back (CIGS/Mo-back contact). Under illumination (i.e. non-equilibrium conditions), electrons will be excited to the conduction band edge (CB) and will immediately be drifted (i.e. "rolled down") towards the front SCR, thereby reducing the back surface recombination. And the push of the electrons towards the SCR is provided by the additional quasi-electric field (ξ_A) as a result of the potential difference in CB (ΔE_g) as illustrated in figure 4.2 [29,78-82].

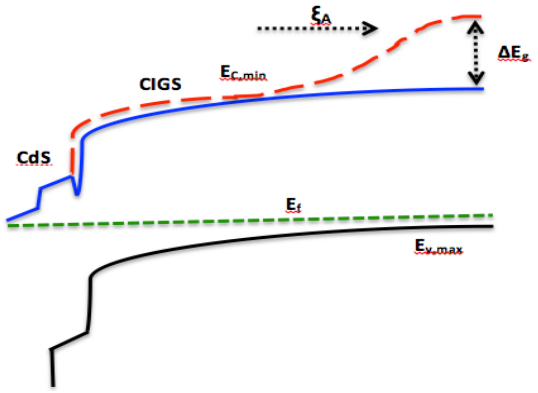

Figure 4.2: Energy band diagram of BSG grading scheme

On the other hand, referring to DSG grading scheme, it is anticipated that the double surface profiling structure will absorb photons with energies higher than Eg_1; furthermore, due to a decreasing energy gap as a function of depth, one can expect photons with energies as low as Eg_2 to be absorbed ($Eg_1 > Eg_2$). Hence, the structure has the potential for optimized photon absorption in a specific photon energy range and the possibility of attaining higher V_{oc} due to the presence of a wider band-gap absorber material near the

junction [44-46]. The two energy gaps at the front of the DSG profiling scheme (Eg_1 and Eg_2 in Fig. 4.3) can be engineered to match certain bands of the solar spectrum (AM1.5) in order to capture more efficiently from the blue and red spectral regions. The improved quantum efficiency in such a device will translate into enhanced current generation (i.e. improvement in the collection probability J_{sc}). An additional enhancement of current generation could also come from a field assisted collection, in other words, the increasing CB edge towards the back of the absorber can provide an effective force field for electrons drifting toward the back contact (similar to the BSG profiling scheme discussed above) [73,77].

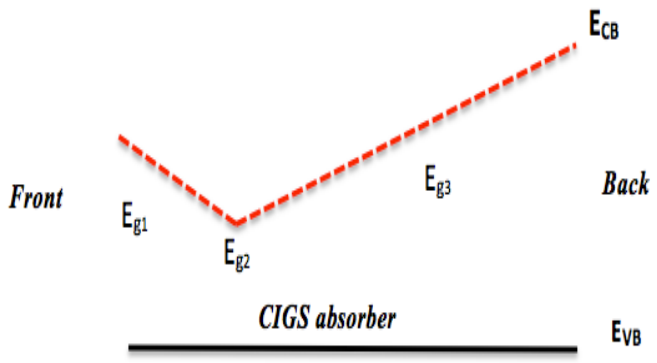

Figure 4.3: Energy band diagram of DSG grading scheme

4.3 Solar cell fabrication and characterization

In our experiments, three different Ga grading schemes were employed: (1) a Uniform Grading (UG) profile (i.e. no variation in Ga ratio throughout the CIGS absorber), (2) Back Surface Grading (BSG) profile (i.e. increase in Ga ratio towards the back surface) and (3) Double Sided Grading (DSG) profile (i.e. increase in Ga ratio both

towards back and front surfaces). In addition to the surface grading effects, the Ga content in the bulk of the absorber is slightly higher for compositionally graded devices when compared to ungraded devices [29,73-77].

An overview of the fabrication steps involved for the above mentioned Ga schemes CIGS solar cell is as follows: After a glass-cleaning step, a Mo layer is deposited as the rear cell contact in an in-line sputtering system. It has a sheet resistance of 0.6 Ω/□ and a typical thickness of 350 nm. The CIGS layer (2 μm) is deposited in a high-vacuum chamber equipped with open-boat evaporation sources while evaporation rates are monitored using a mass spectrometer. Detailed descriptions of the UG, BSG and DSG CIGS layers can be found in Refs. [29,73], respectively. Next, the buffer layer is deposited using a standard CBD (Chemical Bath Deposition) CdS process. Then the shunt reducing intrinsic ZnO layer (i-ZnO), and subsequently the Al-doped ZnO (ZnO:Al) front contact are sputtered. As front contact grid, a Ni/Al/Ni stack is deposited by evaporation through a shadow mask. This ZnO and Ni/Al/Ni stack have a total thickness around 400 and 3000 nm, respectively. Finally, 0.5 cm^2 solar cells are defined by mechanical scribing.

The influence of Ga grading on the overall cell performance was evaluated by the following opto-electronic characterization techniques: current-voltage (J-V) under an AM 1.5 spectrum at 100 mW/cm^2 illumination and spectral quantum efficiency (QE). Furthermore, low-temperature junction capacitance techniques, i.e.

drive-level capacitance profiling (DLCP) and Admittance spectroscopy (AS), were used to analyze spatial and energetic profiling of the defects. More detail information regarding the extraction techniques could be found in Ref's [83-88].

4.4 Characterization of graded and ungraded CIGS Solar cells

Fig.4.4 shows the elemental depth profile of the GGI ratio as measured by glow discharge optical spectroscopy (GDOES) for UG, BSG and DSG devices. Table 4.1 gives the average and standard deviation of cell characteristics results of ten CIGS solar cells with and without Ga grading. Fig 4.5 shows the external quantum efficiency (EQE) results for all the devices considered. Table 4.2 details the devices with best efficiencies with and without grading; (i) device parameters extracted using different measurement techniques. Fig 4.6 (a,b) and Fig 4.8 shows the temperature dependent junction capacitance measurements and the corresponding Arrhenius plots, to estimate (ii) spatial distribution of free-carrier hole densities and deep defect concentration as a function of distance to barrier interface (from DLCP measurements), and (iii) to examine the energy distribution of the defects, to investigate the type of defects, and to estimate the density of states (DOS) (from AS measurements), can be found in Fig. 4.7 and Fig.4.9, respectively.

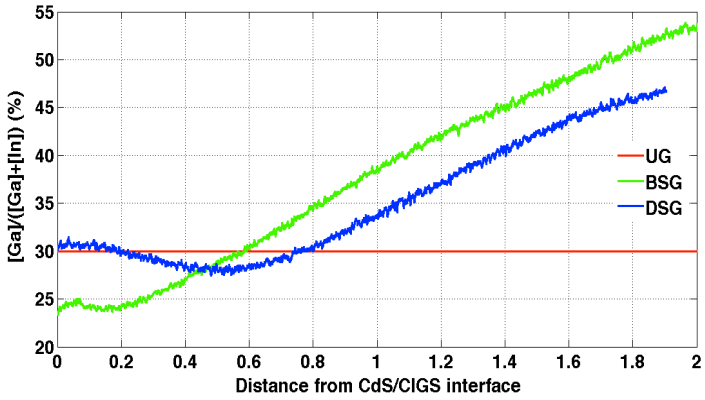

Figure 4.4: Elemental depth profile of [Ga]/([Ga] + [In]) measured by glow discharge optical spectroscopy (GDOES) for graded devices.

4.5 Influence of Ga-grading on CIGS solar cell performance

Table 4.1: J-V parameters (average and standard deviation of ten devices) for devices with and without Ga grading

J-V Parameter	**UG**	**BSG**	**DSG**
V_{oc} (mV)	614 ± 41	659 ± 5	684 ± 6
J_{sc} (mA/cm^2)	32.2 ± 1.1	35.2 ± 0.2	35.1 ± 0.2
FF (%)	72.3 ± 2.9	76.1 ± 0.5	74.4 ± 1.2
η (%)	14.4 ± 1.9	17.7 ± 0.2	17.8 ± 0.4

From Table 4.1: we observe a clear dependency of cell performances on the grading schemes. In the case of BSG, we observe improved cell performance due to increasing Ga content towards the back surface (CIGS/Mo contact). Such a grading profile scheme results in an increased energy conduction band minimum towards the back surface and successively an increased band-gap energy [29,73-77]. The gradient in band-gap will produce an additional quasi-electric field (ξ_{drift}), which repels the photo-generated minority carriers that reach the back Mo contact, thereby reducing the back surface recombination rate and significantly improving the cell Voc. Furthermore, the ξ_{drift} will increase the diffusion length of the minority carriers due to E-field-enhanced-diffusion mechanism, thereby assisting the carriers towards the junction, as a whole improving the current collection probability (J_{sc}) [29,73].

In the DSG scheme, a significant gain in cell V_{oc} (23-117mV) is obtained compared to UG devices, due to additional front surface grading (FSG) in combination with the BSG. This FSG results in increased bang-gap energy at the front surface and in turn a higher barrier height within the SCR, thereby lowering the recombination rates in this region, resulting in an improved V_{oc} [29,73-75]. However, due to front surface layer band gap widening, carriers are generated much deeper in the CIGS layer (i.e. away from the SCR). Hence, the collection probability in this grading scheme will be relatively small and mainly rely on the diffusion mechanism. Thankfully, due to the presence of BSG, the additional drift field (ξ_{drift}) will assist the minority carriers towards the junction without any significant loss in

the collection probability [29,73]. Nevertheless, from the extracted J-V cell parameters (table 4.1), a slight decrease in J_{sc} (0.1-0.4mA) and FF (0-3.4%) was observed for the DSG samples, when compared to the BSG devices. Nevertheless, the differences between the two were not significant. This makes us to believe that in DSG devices, the edge of the front surface-grading region (i.e. notch) is optimally placed within the SCR, and not affected by the conduction band barrier, that significantly effects the carrier collection beneath this region (front surface graded region) [75]. In support to the above discussions, X-Ray Fluorescence (XRF) measurements (please see Appendix B) also revealed that the compositional diffusion length of the FSG profiles was placed within 250nm from the barrier interface. However, further optimization of the depth and position of the gradient edge within the SCR may yield better cell performances (i.e. Jsc, FF and η) [76]. Additionally, experimental QE measurements (see Fig.4.5) reveal that for wavelengths longer than 800nm, there is an improvement in the carrier collection due to addition electric field by implementing DSG profiles, when compared to the UG profile schemes. The carrier collection amongst the two compositional graded profile schemes (BSG and DSG) remains almost the same and with no significant losses due to additional FSG in the DSG devices [72-76].

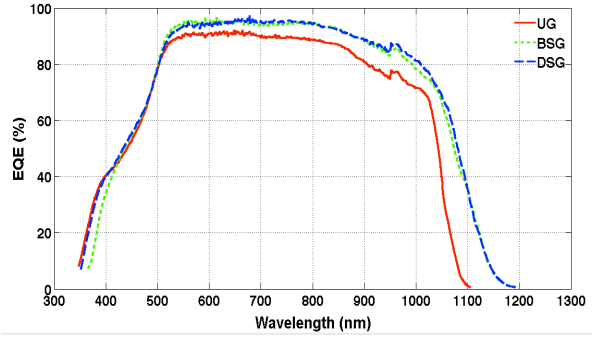

Figure 4.5: External Quantum Efficiency (EQE) measurements for devices with and without Ga grading.

Table 4. 2: Extracted cell parameters with best efficiencies for devices with and without Ga grading.

Measurement Technique	Extracted Parameter	UG	BSG	DSG
J-V	V_{oc} (mV)	645	669	692
	J_{sc} (mA/cm^2)	33.3	35.7	35.3
	FF (%)	75.2	76.8	76.3
	η (%)	16.1	18.0	18.4
EQE	E_g (eV)	~1.18	~1.13	~1.12
C-V (Also see Appendix B)	U_d (mV)	700 ± 15	780 ± 08	740 ±05
	W_d (µm)	243 ± 16	347 ± 18	366 ± 13
AS	E_a (eV)	113	255	263
	ξ_o (s^{-1})	3.6 x 10^{11}	7.2 x 10^{11}	8.9 x 10^{11}
	N_{AS} (cm^{-3})	(5-7) x 10^{15}	(3-5) x 10^{15}	(1-3) x 10^{14}
DLCP (Also see Appendix B)	N_{DLCP} (cm^{-3})	(3.2-42) x 10^{15}	(1.3-2.5) x 10^{15}	(8.6-36) x 10^{14}
	p (cm^{-3})	(3.5-20) x 10^{15}	(0.92-1.10) x 10^{15}	(2.1-9.8) x 10^{14}
	$N_{T,\ SCR-0.4\ \mu m}$ (cm^{-3})	4x10^{16}	2x10^{15}	8.6x10^{14}
XRF (Also see Appendix B)	CGI (%) at (0.8-1.6) µm	0.97	1.05-0.91	1.01-0.83
	GGI (%) at (0.8-1.6) µm	0.33	0.45-0.38	0.43-0.37

4.6 Temperature-dependent junction capacitance measurements

To yield a better understanding of the grading effects on the cell performances, junction capacitance measurements were performed on the devices with best efficiencies (Table 4.2). In order to estimate the spatial distribution of free hole carrier densities and deep- acceptor concentrations, a set of DLCP profiles were taken at a fixed frequency (10kHz), varying DC biases (V_{dc}) from -1V to +0.9V, in 0.1V increments and varying amplitude of the ac voltage ($V_{ac,rms}$) from 14 mV to 144mV, in 10mV increments, over a broad range of temperatures (80K-260K with a step of 20K) [48,50]. However, in Figure 4.7, we will show the results at only two temperatures (80K and 260K) to avoid DLCP-profile overlapping. We have investigated the influence of defect densities on the overall cell performances by examining the DLCP data at two distinctive probing distances away from the barrier interface: (i) ~0.4 μm (i.e. close to the SCR region) and (ii) >0.8 μm (i.e. in the bulk of the absorber where the electric field is nearly zero). In particular, a probing distance of 0.4μm has been chosen in our analysis due to the fact that the SCR widths for the above-considered devices fall within 0.4 μm, as indicated by the C (V) measurements (please see Table 4.2, Fig 4.6(a) and Appendix B).

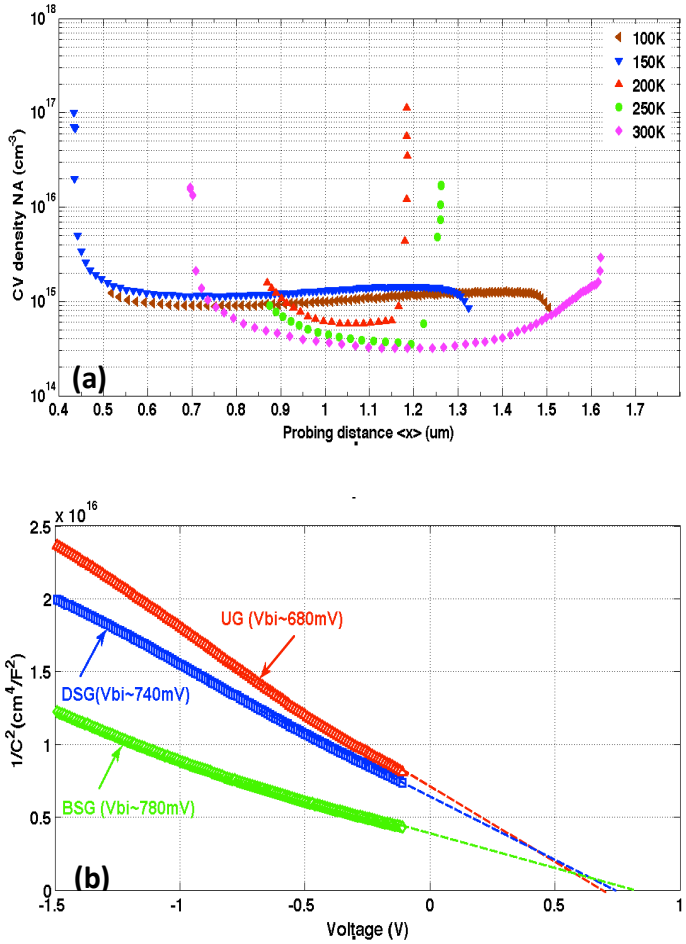

Figure 4.6: Sample (a) CV- profiling as a function of temperatures on UG devices (b) Mott-Schottky plots for devices with and without Ga grading.

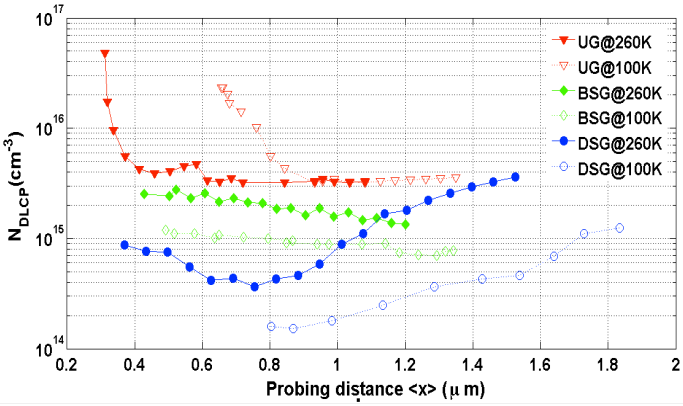

Figure 4.7: Drive-level response for devices with and without Ga grading.

From Figure 4.7, the low-temperature DLCP profiles (open markers) represent the free carrier densities for the three graded profiles. We can clearly see that far away from the barrier interface (>0.8μm), the free carrier densities remains spatially uniform for the uniformly graded samples, while its concentration is lower for other two compositionally graded devices due to reduced copper to gallium plus indium CGI=Cu/(Ga+In) ratio for almost similar concentration of Ga (0.45-0.37). It's also important to note that the magnitude of these free carriers decreases from UG to DSG profile schemes, making the two compositionally graded profile schemes, less conductive for the majority carrier (holes), within the part of absorber where the power generation is less active. Nevertheless, a slight increase in the free carrier concentration was observed for the DSG sample close to the

back Mo contact (~1.8 um), making the hole Fermi level close to the E_v [29,86,88,89].

On the other hand, the deep-defect densities (N_{dlcp}) were estimated from the high-temperature DLCP data (filled markers). Interestingly, there exists an inverse correlation between extracted defect deep densities and the cell V_{oc} (Table 4.2) close to the depletion region (i.e. ~ 0.4um). The V_{oc} starts increasing from UG devices (645mV) to BSG devices (669mV) and to DSG (692mV) devices, with decreasing deep-defect densities close to the depletion region (i.e. from $4x10^{16}$ to $2x10^{15}$ and to $8.6x10^{14}$ cm^{-3}). This behavior can be explained as follows, under open-circuit conditions, the dominant recombination mechanism in the depletion region is governed by Shockley-Read-Hall (SRH) recombination, due to excess-carrier recombination via deep defects. Presence of higher concentrations of deep-level defects in this region reduces the electron (E_{Fn}) and hole (E_{Fp}) quasi-Fermi levels splitting and thereby ($\Delta E= E_{Fn} - E_{Fp}$), which reflects the maximum V_{oc} of the solar cell ($-qV_{oc}= \Delta E$), q being the elementary charge [90,91]. Hence, the influence of FSG on the cell performance can be explained by comparing the experimentally extracted V_{oc} and N_{dlcp} results of UG and DSG samples.

These results clearly indicate that, with decreasing Ga content away from the front surface, the cell V_{oc} increases due to reduced deep-level defect concentration in the SCR. Since, the high-temperature DLCP signal is a result of the sum of all states, i.e. both the free carriers (p) and the deep-trapping states (N_T) [11]. Moreover,

the N_T is extracted from the difference between maximum of the high temperature DLCP signal and the low-temperature DLCP signal. Interestingly the N_T extraction also shows inverse correlation trends with increasing V_{oc} (i.e due to reduced recombination) from UG to BSF and to DSG devices (Table 4.2)[29].

In addition, to the study of spatial variation of deep defect densities, we have also performed AS to examine the energy distribution of defects, investigate the type of defects existing, and finally estimate the density of states (DOS) [49]. This involves measurement of junction capacitance with varying frequency (f) ranging from 1kHz to 1MHz over a temperature (T) scan (80K to 240K with a step of 20K), at fixed DC bias (0V) and modulating voltage (35 mV_{rms}). For the temperature range mentioned above, the inflation frequencies (ω_o) were extracted by taking the maxima of the derivative ($-\omega dC/d\omega$) from the angular frequency-dependent capacitance C (ω) spectra. Arrhenius plots were obtained by plotting the $\ln(\omega_o T^{-2})$ vs T^{-2}. The extracted activation energies (E_a) and the pre-exponential factor (ξ_o) from the Arrhenius plots (see Fig 4.8) were listed in Table (4.2) for the respective samples [29].

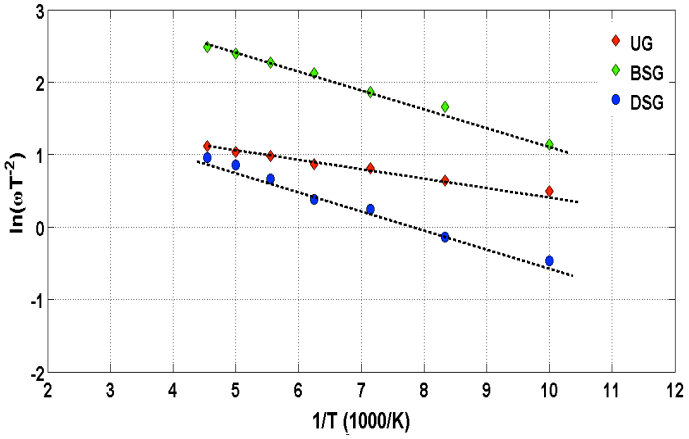

Figure 4.8: Arrhenius plots for devices with and without Ga grading

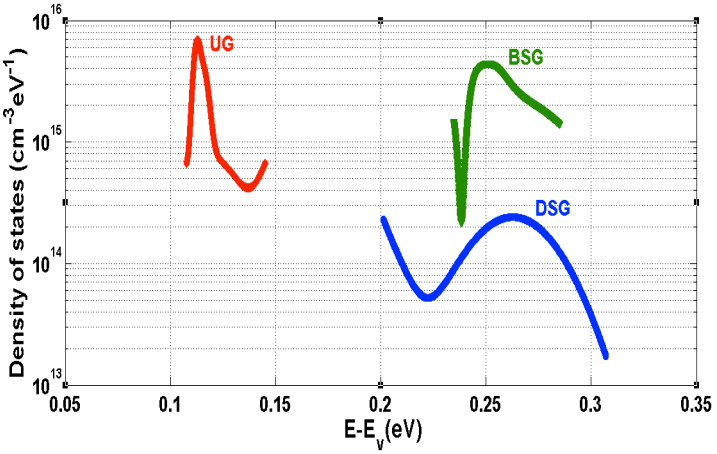

Figure 4.9: Density of states (DOS) calculated from Admittance spectroscopy (AS) using Gaussian fitting for devices with and without Ga grading.

Figure 4.9 represents the estimated defect distribution using parabolic band (ideal for an n^+p junction) approximation (please see Appendix B) [29,88,89]. Other parameters like depletion width (W_d) and built-in voltage (U_d), that are required to estimate the parabolic band approximation were taken from the C(V) measurements (table1). From the above results shown in Fig 4.7 and 4.9, UG sample exhibits the lowest E_a of 113 meV away from the valence band edge (E_v) with a deep-defect density roughly about 6 $x10^{15}cm^{-3}$. The other two compositionally graded samples (BSG and DSG) show E_a near 255 meV and 263 meV with deep-defect densities roughly about $3x10^{15}$ cm^{-3} and $2x10^{14}$ cm^{-3} respectively. The densities of trapping states extracted from AS are in good agreement compared to those extracted from DLCP measurements. Based on the extracted E_a values, we assume that the UG devices exhibit defects of type N1 (interface defects), and the other two compositionally graded devices of type N2 (bulk defects) [29,83-89]. An interesting correlation can be drawn between the extracted E_a from AS and to the free carrier densities (p) estimated from the low-temperature DLCP signal. As mentioned above, due to decreasing CGI ratio (i.e. copper poor) in the bulk of the absorber from UG to DSG devices, the free-carrier densities decrease due to increasing resistivity in the bulk of the absorber and therefore increasing Ea. Hence, the compositionally graded devices (BSG and DSG) have relatively low carrier emission rates from the trapping states, which are more likely to participate in the recombination mechanisms, when compared to UG devices. Despite having deeper defect states and not able to provide additional free carrier holes, the

DSG devices however exhibit low- deep defect densities in the SCR resulting in an enhanced cell performance. On the other hand, UG device by itself with an E_a of 113meV is less likely to get ionized at room temperature and contribute for additional hole carriers. Additionally, the type of defects found in UG devices being interface type could be another possible reason for such reduced V_{oc} [83-89].

4.7 Summary

To summarize the chapter, from the obtained experimental results and analyses, we have demonstrated the benefits of gallium (Ga) grading on Cu(In,Ga)Se_2 (CIGS) solar cell performance when compared to the ungraded CIGS cells. Devices with DSG profile schemes exhibit higher cell performances (18.4%) when compared to BSG (18%) and ungraded devices (16.1%). Significant improvement in DSG devices is mainly due to enhanced cell V_{oc}, due to reduced recombination rates both in the SCR and at the back surface (CIGS/Mo contacts), without any significant loss in the J_{sc} values. On the other hand, BSG devices exhibit satisfactory cell performances (18.0%) with an overall gain in V_{oc} of 24mV compared to UG devices, due to reduced back surface recombination and deep defect states by a factor of two in the SCR. Additionally, a gain in J_{sc} ~2.4mA in these devices is due to the additional drift field (ξ_{drift}) created by the back surface grading. Finally, ungraded devices shows the lowest V_{oc} among the three devices, due to enhanced SRH recombination with in the SCR region and also due to the absence of additional drift field (ξ_{drift}) to improve the carrier collection probability. DLCP-extracted defect densities near the depletion region support with the above

discussion. Additionally, through the use of AS analysis, the type and density of states in these devices have been probed. In the case of UG devices, the defects are found to be of type N1 (interface) and compositionally graded devices of type N2 (bulk).

Additionally, from the obtained results, it's clearly evident that the parameter most constraining the cell's V_{oc} is found to be the deep-defect density close to the space charge region (SCR). In ungraded devices, high deep-defect concentrations (4.2×10^{16} cm^{-3}) were observed near the SCR, offering a source for Shockley-Read-Hall recombination, reducing the cell's V_{oc}. In graded devices, the deep-defect densities near the SCR decreased by one order of magnitude ($2.5x10^{15}$ cm^{-3}) for back surface graded devices, and almost two orders of magnitude ($8.6x10^{14}$ cm^{-3}) for double surface graded devices, enhancing the cell's V_{oc}. In compositionally graded devices, the free-carrier density in the absorber's bulk decreased in tandem with the ratio of GGI= Ga/(Ga + In), increasing the activation energy, hindering the ionization of the defect states at room temperature and enhancing their role as recombination centers within the energy band. This brings us to a convincing conclusion that Ga-grading is ideally not the best choice to reduce the rear surface recombination at the CIGS/MO back contact due to its unwanted detrimental effects (i.e. deep-defects, reduced free carrier density etc.). Hence, to overcome these setbacks (due to Ga-grading), an alternative cell design approach is proposed and analyzed (based on the obtained solar cell results) in ***Chapter 5.*** The idea basically includes the implementation of PERC cell concept in thin film (CIGS) solar cell processing. Similar to the

silicon PERC cell architectures (please see Fig 1.3 of Chapter 1), the PERC-CIGS cell architectures consist of rear Mo-back contact with point contacts to the absorbing material (CIGS) through a negatively charged dielectric film (Al_2O_3). Followed by the conventional CIGS solar cell processing (i.e. CdS/i-ZnO/Zno:Al/Ni-Al-Ni). This way, the Al_2O_3 passivation layer will provide both chemical and field effect passivation at the CIGS/Mo interface, thereby reducing the overall rear surface recombination rate down to S_b <100 cm s^{-1}.

CHAPTER 5: PASSIVATION EFFECTS OF ALD/DC-SPUTTERED Al_2O_3 FILMS ON ULTRA-THIN CIGS SOLAR CELL PERFORMANCE

5.1 Introduction

The concept of passivating CIGS surfaces using Al_2O_3 films is based on previous experience gained from c-Si solar cell technologies [16,17,19]. The surface passivation of c-Si surfaces using Al_2O_3 films has drawn intense attention from the silicon photovoltaic community due to its ability to effectively passivate the p-type silicon surfaces [11-15, 43]. And the passivation ability is attributed to a high density of negative Q_f (10^{12}–10^{13} cm^{-2}) in the Al_2O_3 bulk (field-effect passivation) in combination with a low interface-trap charge density D_{it} (10^{10}–10^{12} eV^{-1} cm^{-2}) at the Al_2O_3/Silicon interface (chemical passivation), resulting in an overall effective SRV < 5 cms^{-1} on p-type surfaces [40-43]. Owing to these capabilities on p-type surfaces, within the course of this research work, we *have* expanded *our research focus on the surface passivation effects of Al_2O_3 films on p-type CIGS absorbers. And this has been accomplished by (i) realizing an* innovative solar cell structure followed by (ii) an in-depth investigation of the electronic properties at the CIGS/Al_2O_3 interface.

Moreover, it's clearly evident from the obtained opto-electrical cell characterization results presented in Chapter 4, that the thin-film PV research community needs to adapt new cell processing and/or

architectures in order to: (i) limit the use of excess Ga-concentrations and their determinantal effects, (ii) reduce the rear surface recombination rates (S_b) and (iii) to improve the rear internal reflection (R_b) for an enhanced cell performance. As an attempt to address these challenges, in Section 5.1 of this chapter, we will present a comprehensive introduction to the innovative thin-film (CIGS) cell architecture (i.e. PERC-CIGS), their sequence of process steps, and the corresponding cell characterization results. Followed by Section 5.2, with an in-depth discussion (solar cell results) on the (a) rear surface passivation layer quality, (b) passivation layer thickness and (c) rear surface reflectance, against the unpassivated reference cells with two different thickness (0.4 and 1.8 um). Additionally, in Section 5.3, we will quantify the electronic properties and comment on the involved, dominant passivation mechanism at the CIGS/Al_2O_3/Mo interface, using experimentally obtained C-V characterization results on M-I-S structures. Next in Section 5.4, we will introduce, validate and discuss about a simplified 1D–SCAPS simulation model that has been developed especially to address and relate the influence of (i) interface chemical passivation (ii) field effect passivation and (iii) the CIGS layer thickness dependency on the obtained experimental cell results. Finally in Section 5.5, we will conclude this chapter by review the major improvements offered by PERC-CIGS cell technologies when compared to the unpassivated CIGS solar cells.

5.2 PERC-CIGS Solar Cell Fabrication

In order to realize the PERC-CIGS cell concept, the solar cells were fabricated at Ångström Solar Center (University of Uppsala) using their standard CIGS baseline process parameters [29,32,93-97]. However, the rear surface DC (direct current)-sputtered Al_2O_3 films were deposited at Winfab platform (UCL) [59]. To begin with the process sequence of PERC-CIGS solar cells, we have considered rigid 1mm thick soda lime glass (SLG) as the base substrate. Prior to the back contact formation, the SLG undergoes a thorough cleaning process. As back contact, a Molybdenum (Mo) layer is deposited in an in-line sputtering system with a sheet resistance of 0.6Ω/□ and a typical thickness of 350 nm. The advanced back contact design combines a rear surface passivation layer and CBD (Chemical Bath Deposition) of CdS to generate nano-sized point openings. More detailed information about the particle-rich point formation can be found in Ref's [32, 93-96]. On top of this rear contact structure, first a 15 nm NaF layer is evaporated, followed by co-evaporation of the ungraded CIGS absorber layer of desired thickness. These ungraded CIGS absorbers with uniform low Ga concentration are favored to assess rear surface passivation, due to (i) their high reproducibility, (ii) their characteristic high minority carrier diffusion length, and (iii) to exclude complementary rear surface passivation effects (e.g., Ga-grading). The buffer layer is deposited using a standard CBD CdS process. Next, the shunt reducing intrinsic ZnO layer (i-ZnO) and subsequently the Al-doped ZnO (ZnO:Al) front contact are sputtered. As front contact grid, a Ni/Al/Ni stack is deposited by evaporation

through a shadow mask. The ZnO and Ni/Al/Ni stack have a total thickness around 400 and 3000 nm, respectively. Finally, 0.5 cm^2 area solar cells were defined by mechanical scribing followed by 110 nm MgF_2 anti-reflective coating evaporation (to avoid interference fringes). Fig 5.1 illustrates the Transmission Electron Microscopy (TEM) cross-section image of the point-contact PERC CIGS solar cell with ALD-Al_2O_3 layer deposited in a temporal ALD reactor at standard temperatures (300°C) using trimethylaluminum (TMA) and water (H_2O) as precursors, resulting in a typical 1Å/cycle growth rate. While for the case of DC-sputtered Al_2O_3 films, the deposition was carried from an Al (99.9%) target in an Ar/O_2 gas mixture. These depositions are performed at room temperature and at constant total pressure, having a deposition rate of around 5nm/min [95].

To understand the influence of the rear surface passivation layer (i.e. quality, thickness, rear reflectance and unpassivated CIGS absorber layer thickness) on the cell performance, various combinations of rear surface passivation schemes were employed. Those include: (a) 25nm and (b) 50 nm of DC-sputtered Al_2O_3 films, (c) 60 nm (MgF_2)/ 5nm (ALD-Al_2O_3) stack and (d) unpassivated CIGS/Mo–interface with two different absorber layer thickness (0.4 μm and 1.8 μm). Fig 5.1 shows the sample TEM cross-sectional image of the proposed PERC-CIGS solar cell [95].

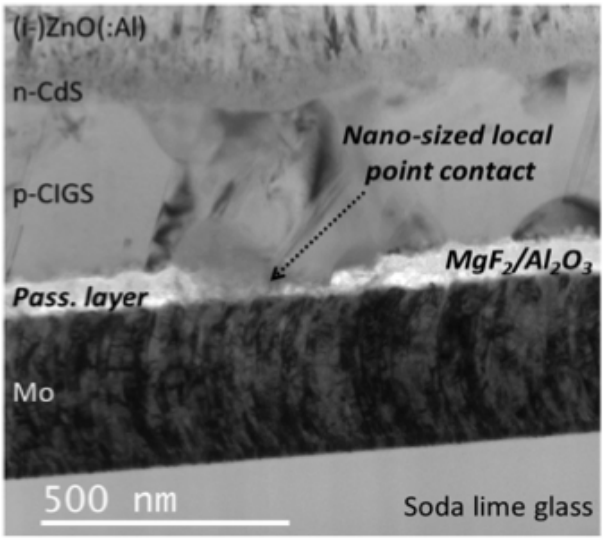

Figure 5.1: Sample TEM cross-section picture of a 60nm (MgF_2)/5nm(ALD-Al_2O_3) rear surface passivated Cu(In,Ga)Se_2 solar cell with nano-sized local rear point contacts (Courtesy of B. Vermang and University of Uppsala [taken from ref 95]).

5.3 PERC-CIGS Solar Cell Characteristics

In order to understand the influence of rear surface passivation effects on the overall cell performance, several opto-electrical characterization techniques were performed on the above-mentioned solar cells. Those include mainly the illuminated J–V characteristics, external quantum efficiency (EQE) and the rear reflectance (R_b) calculations (please see ref 95) for various combinations of rear passivation schemes.

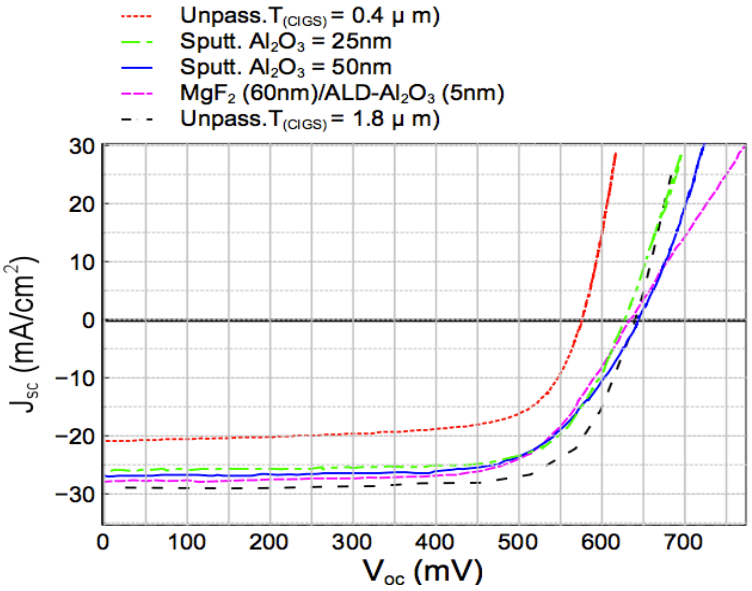

Figure 5.2: J-V characteristics of the unpassivated (0.4 um, 1.8um) and (MgF_2/) Al_2O_3 rear surface passivated Cu(In, Ga) Se_2 solar cells [taken from ref 95]

In principle, for unpassivated CIGS solar cell, reducing the absorber layer thickness eventually leads to a drop in the cell performance (see Table 5.1) mainly attributed due to low R_b and high S_b (no passivation). Table 5.1 also shows the extracted cell parameters for MgF_2/Al_2O_3 (65 nm) and for Al_2O_3 (25 or 50 nm) rear passivated CIGS (~0.385 μm) solar cells, compared to unpassivated standard CIGS (1.8 μm). From the obtained cell results, it can be clearly seen that there is a significant loss in both V_{oc} and J_{sc} when the CIGS absorber layer thickness is reduced from 1.8 μm to 0.4 μm in the case of unpassivated reference cells [95].

Table 5.1: ***Extracted cell parameters (AM 1.5G) from J-V characteristics for unpassivated (0.4 um, 1.8um) and (MgF_2/) Al_2O_3 rear surface passivated Cu(In, Ga) Se_2 solar cells [taken from ref 95]***

Rear passivation scheme	**# cells**	**t_{CIGS} (μm)**	**Voc (mV)**	**Jsc (mA/cm^2)**	**FF (%)**	**η (%)**
None (unpass)	6	0.4	576 ± 2	23.2 ± 0.3	67.7 ± 0.7	9.1 ± 0.1
Sputtered Al_2O_3 (25nm)	6	0.4	624 ± 2	29.0 ± 0.4	72.6 ± 0.5	13.1 ± 0.2
Sputtered Al_2O_3 (50nm)	6	0.4	644 ± 6	30.2 ± 0.8	67.8 ± 1.7	13.2 ± 0.4
MgF_2 (60nm)/ALD-Al_2O_3 (5nm)	6	0.4	633 ± 2	31.1 ± 0.1	68.7 ± 1.9	13.5 ± 0.4
None (unpass)	6	1.8	639 ± 7	32.8 ± 0.5	74.1 ±1.2	15.6 ± 0.7

One possible reason that can be put forward to explain such reduction is due to high S_b and low R_b CIGS/Mo interface gets closer to the active region of the solar cell (i.e. SCR). However, these losses due to high S_b and low R_b for ultra-thin CIGS layers can be minimized significantly by applying highly reflective MgF_2/Al_2O_3 (65nm) stack between CIGS and Mo-back contact (i.e. CIGS (385nm)/MgF_2/Al_2O_3(65nm)/Mo back-contact).

The thick MgF_2/Al_2O_3 (65nm) will enhance the rear R_b and lowers the S_b considerably when compared to the unpassivated cells. This eventually led to an absolute improvement in both V_{oc} (57mV) and J_{sc} (7.8 mA/cm^2), when compared to the unpassivated CIGS of almost same thickness (0.4 um). Such an improvement in V_{oc} can be attributed to the interface passivation offered by the 5nm-ALD Al_2O_3 films, while the gain in J_{sc} can be attributed to the enhanced rear reflection provided by the 60nm-MgF_2 layers [95].

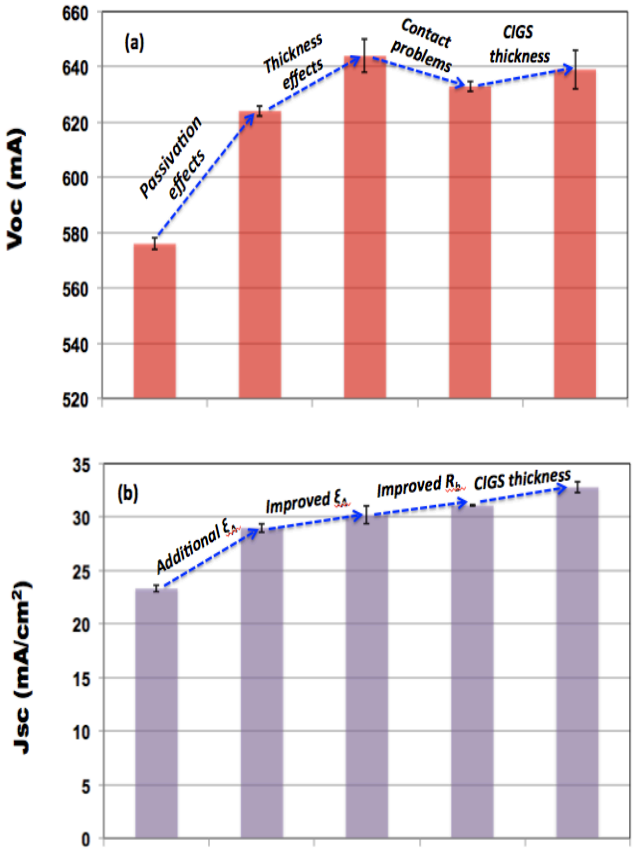

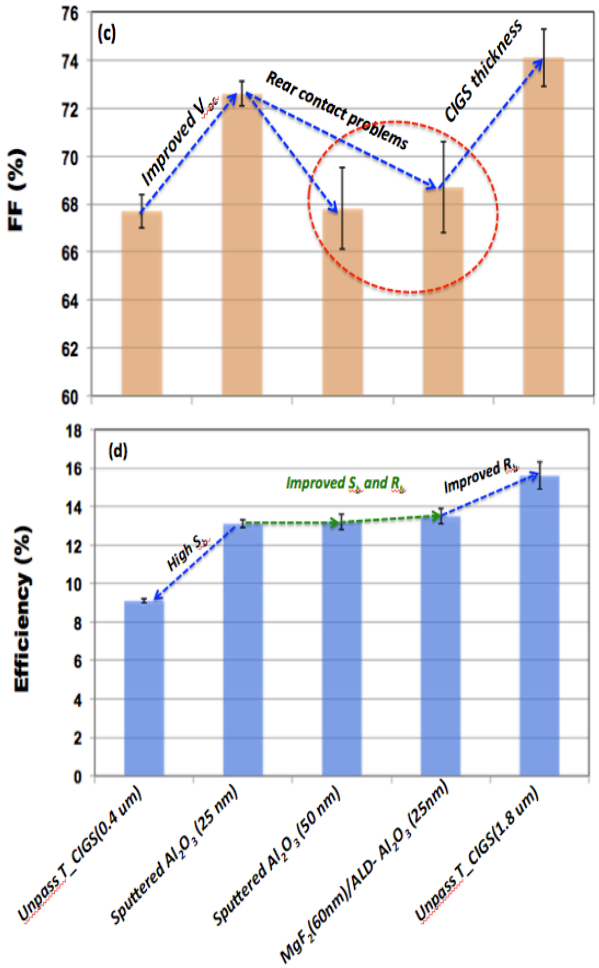

Figure 5.3: Average on 6 samples (a) open circuit voltage (b) short circuit current (c) fill factor and (d) cell efficiencies for 0.5 cm^2 upassivated and rear surface passivated CIGS solar cells, standard deviation is shown as error bars.

25nm-DC-sputtered Al_2O_3 rear passivated cells also exhibit an improvement in both V_{oc} (~48mV) and J_{sc} (~5.8 mA/cm^2), when compared to the unpassivated CIGS of same thickness (0.4 um) [95]. The enhancement in V_{oc} once again clearly demonstrates the

improvement in S_b, while the gain in J_{sc} is due to the additional-electric field (ξ_A) created by negative fixed charges in bulk of the Al_2O_3 films, which assists the minority carriers towards the space charge region (SCR), thereby increasing the current collection probability (please see EQE measurements in Fig 5.4).

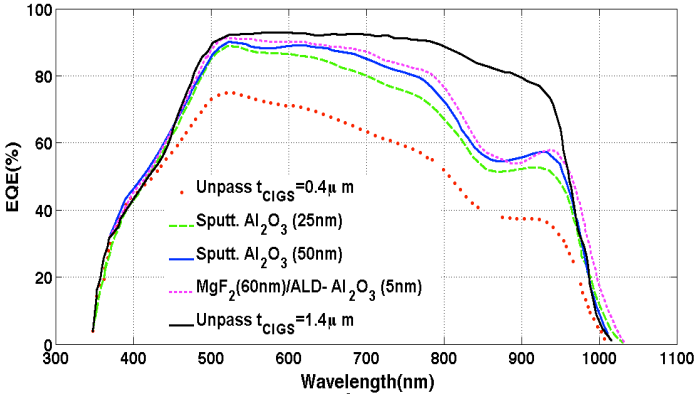

Figure 5.4: *External Quantum efficiency measurements for upassivated reference cells and passivated (MgF_2/) Al_2O_3 rear surface passivated CIGS solar cells (Courtesy of B. Vermang and Universität Uppsala [95])*

On the other hand, when comparing the results of 25nm with 50 nm Al_2O_3 passivated cells, there is a considerable improvement in V_{oc} (~20-24 mV) and little improvement in Jsc (~0.8-2.4 mA) in the former cells (i.e. 50nm Al_2O_3). This could be due to enhanced interface passivation (chemical) with increasing thickness (i.e. reduced S_b), improvement in R_b and almost similar ξ_A (saturation in negative fixed charges for both 25 nm and 50 nm Al_2O_3 films). On the other hand, the average V_{oc} of the DC-sputtered Al_2O_3 rear passivated

cells is quite low in case of a 25nm Al_2O_3 passivation layer and increases as a function of Al_2O_3 thickness (50nm) [95]. This can be explained by DC-sputtering being a lower quality deposition technique compared to the ALD-Al_2O_3 films. Nevertheless, increasing the thickness leads to an enhanced interface passivation. Furthermore, as a result of improved V_{oc} in all passivated cells, the average fill factor (FF) also improved when compared to the reference unpassivated cells with equivalent thickness (0.4um). Nevertheless, the FF tends to decrease with increasing rear surface passivation layer thickness (see Fig 4.2 and Fig 4.3), due to increasing serial resistance (R_s). This increase in R_s can be explained by a lack of contact openings for thicker passivation layers, as the CdS point contact opening approach becomes slightly less effective [93-97].

5.4 Investigating the electronic properties of CIGS/ALD-Al_2O_3/Mo- interface

From the obtained solar cell results in Section 5.2, it is clearly evident that Al_2O_3 rear-surface passivation of ultra-thin CIGS solar cells can significantly enhance the open-circuit voltage (V_{oc}) due to a reduced rear surface recombination velocity at the CIGS/Mo interface, ultimately leading to a notable enhancement in cell efficiency [i.e., by more than 4.5% (abs.)] compared with corresponding unpassivated reference cells. Additionally, in support to the arguments and deliberations presented in Section 5.2, the rear surface recombination rate has been qualitatively addressed in Ref. [98] by means of photoluminescence (PL) measurements, where an elevated PL

intensity by one order of magnitude was seen for passivated CIGS absorbers compared with unpassivated. Such improvements in the cell efficiencies and PL intensity led us to characterize the electronic properties of the CIGS/ALD-Al_2O_3/Mo interface and the dominant passivation mechanism involved. W.W. Hsu et al. [99] reported that introducing ALD Al_2O_3 passivation films on CIGS surfaces could reduce the effective surface recombination velocity (S_{eff}) to 14–44 cm/s. Such low S_{eff} values for Al_2O_3 passivated CIGS surfaces are attributed to an adequate field-effect passivation in combination with an improved chemical passivation. Therefore, in the case of CIGS surface passivation by ALD-Al_2O_3, experimentally extracting these electronic properties is important (i) to evaluate the passivation quality involved, and (ii) to understand the dominant passivation mechanism involved.

From the experiments undertaken, we will also present for the first time experimentally extracted Q_f and D_{it} values for ALD-Al_2O_3 passivated CIGS surfaces. These values were extracted by characterizing capacitance vs. voltage and frequency (C–V–ω) and conductance vs. frequency and temperature (G–ω–T) at different voltages on metal–insulator–semiconductor (MIS) structures [43-45, 59, 100].

5.4.1 CIGS/ALD-Al_2O_3/Mo (M-I-S) capacitor fabrication

The MIS structures (illustrated in Fig 5.5) consists of a 350 nm thick molybdenum back contact sputtered on a soda-lime glass (SLG) substrate, followed by a 2 μm thick CIGS absorber layer (with

uniform gallium profile) co-evaporated at 510°C. A 22.5 nm thick Al_2O_3 film was deposited on the CIGS surfaces in a temporal ALD reactor at 300°C using trimethylaluminum and water as precursors. The thickness of the Al_2O_3 film was monitored by the growth rate (0.9 Å/cycle). Finally, aluminum front contacts, with a contact area of 7.8 × 10^{-3} cm^2, were evaporated through a shadow mask.

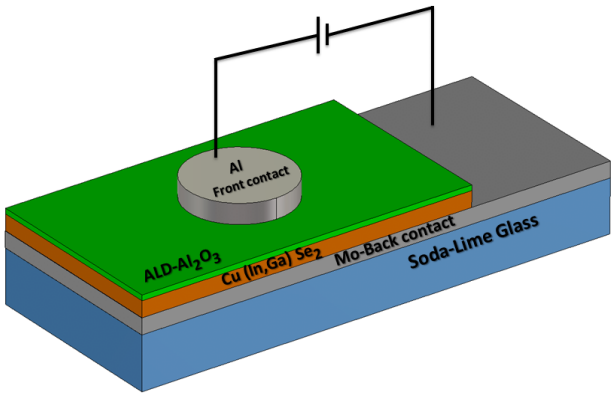

Figure 5.5: Schematic of Al/ALD-Al_2O_3/CIGS/Mo-back contact (M-I-S) capacitor

The influence of annealing treatment on the passivation quality was examined by fabricating two sets of MIS structures: (i) As-deposited (AD) Al_2O_3 films (i.e., non-annealed) on CIGS surfaces and (ii) post-deposition annealed (PDA) Al_2O_3 films (at 510°C in a selenium (Se) atmosphere) on CIGS surfaces. At this point it is important to note that the post-deposition annealing treatment performed in our experiments is not a "special anneal" but "a way to mimic the processing of rear passivated CIGS solar cells", where the CIGS layer is grown (at the same temperature and in the same Se atmosphere as

the anneal used) on top of the passivation layer. On the other hand, it also enables us to investigate the effects of annealing treatment on the electronic properties of CIGS/ Al_2O_3/Mo- interface [100].

5.4.2 Electrical characterization of the CIGS/ALD-Al_2O_3/Mo (M-I-S) capacitor

To quantify and evaluate the electronic properties of the AD and PDA films, a detailed electrical characterization was performed using *C–V–G* measurements on MIS structures to extract the Q_f and D_{it} values. Fig. 4.6 (a) depicts the *C–V* characteristics of the AD and PDA films measured at 10 kHz and fig. 4.6 (b) shows the *C–V* curves at different frequencies for the PDA films. In the case of the AD films, a depletion/weak-inversion transition region occurring at negative applied gate voltages was observed, whereas the transition region occurred at positive gate voltages for the PDA films. The corresponding flatband voltage (V_{fb}) positions are attributed to the polarity and concentration of Q_f present in the films [43-45,59,100].

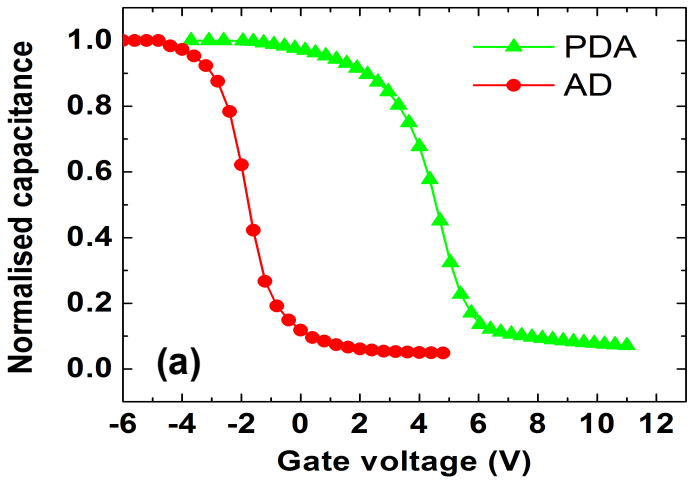

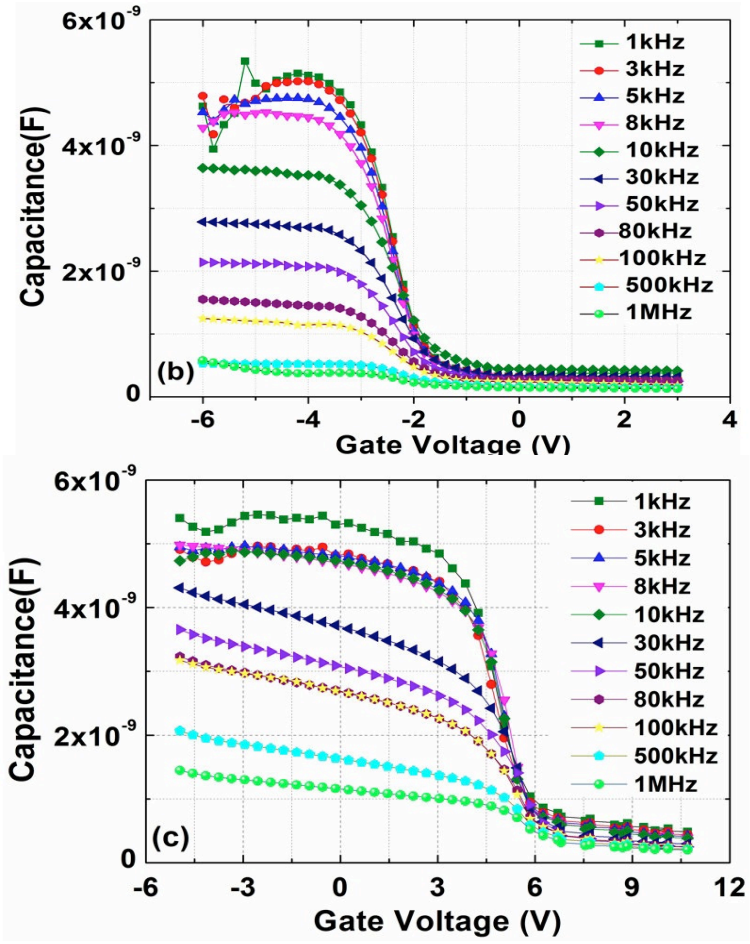

Figure 5.6: *(a) Normalized capacitance–voltage (C–V) plots at 10kHz for AD and PDA films, C–V as a function of frequency for (b) AD and (c) PDA films.*

As can be seen in Figs 5.6(b) and (c), the C-V curves show strong frequency dispersion effects in the accumulation regime. One possible explanation from the literature that can be put forward to explain the observed parasitic effects is due to the "oxide, near interface traps and

border traps," residing in the oxide [92-94]. These traps communicate with the underlying semiconductor electrons/holes by tunneling mechanism and the associated time constant depends on the trap distance to the interface, giving rise to frequency dispersion [100]. These parasitic effects will alter the measured capacitance-conductance (C-G) values, which will in turn affect the interpreted D_{it} up to an order of magnitude. Therefore, to minimize the influence of these effects on the extracted interface electronic properties, all the measured C-V-G curves were first corrected for parasitic free C-V-G curves using "dual-frequency five-element circuit model" proposed in Ref. [101]. The effective fixed charge density (Q_f) for both AD and PDA films was estimated from the flatband voltage (V_{fb}) of the low frequency C-V curve using the following equation [44,45]:

$$Q_f = \frac{C_{ox}(W_{ms} - V_{fb})}{A * q} \qquad (5.1)$$

where W_{ms} = −0.97 V is the estimated work function difference between metal (Al) and semiconductor (CIGS) for an acceptor concentration of N_A= 5× 10^{15} cm^{-3} (from C-V see Appendix B), C_{ox} is the oxide capacitance, q is the elementary electric charge and A is the top Al gate area. The extracted V_{fb} values as a function of temperature for the AD and PDA films are in the range of -2.1 to -2.7 V and +3.3 to +3.6 V, resulting in a fixed oxide charge density of +1.6 to +2.5 × 10^{12} cm^{-2} and -9.4 to -11.0 × 10^{12} cm^{-2}, respectively. These results reveal that the field-effect passivation due to negative fixed charges is

activated only for post-deposition annealed Al_2O_3 films, and that the extracted negative fixed charge density Q_f is within a range similar to that observed on silicon surfaces [9-12]. This indicates that the field-effect passivation quality achieved by the PDA films on CIGS surfaces is comparable to that achieved by ALD Al_2O_3 films on silicon surfaces [11-15,43]. Furthermore, because of the presence of highly negative Q_f values in the PDA films, the net concentration of minority carriers (n_s) at the CIGS surface will be reduced, thereby satisfying one of the requirements to reduce the surface recombination rate (U_s) according to the Shockley–Read–Hall formalism [7,43,58].

Another possibility for reducing U_S is to reduce the interface trap charge density (D_{it}) at the Al_2O_3/CIGS interface, since it reflects the chemical passivation quality at the interface. Reliable estimations of D_{it} on the AD and PDA films were obtained using normal and full conductance methods over limited band energies (i.e., near band edge) [44-45,103]. Figs 5.7 (a) and (b) show the normalized interface-trap parallel conductance over angular frequency (G_p/ω) as a function of the small-signal ac frequency (f) for the AD and PDA films, respectively. The plots of G_p/ω vs. f were generated for a broad range of temperatures (100-260 K, in steps of 20 K) for depletion gate voltages. The D_{it} values were estimated from the peak maximum of the G_p/ω vs. f plot, which corresponds to the energy loss at the interface as a consequence of trapping and de-trapping mechanisms. The relation between G_p (ω) and the trap density D_{it} is given as [44,45]:

$$\frac{G_p(\omega)}{\omega} = \frac{qD_{it}}{2\omega\tau_{it}} \ln\left[1 + (\omega\tau_{it})^2\right] \quad (5.2)$$

from which one can deduce:

$$D_{it} = \frac{2.5}{A * q}\left(\frac{G_p}{\omega}\right)_{max} \quad (5.3)$$

where $(G_p/\omega)_{max}$ is the maximum $(G_p(\omega)/\omega)$ value and τ_{it} is the interface-trap response time constant. The extracted D_{it} values as a function of temperature for the AD and PDA films are in the range of (1.4–2.2) × 10^{12} $eV^{-1}cm^{-2}$ and (8.3–11.0) × 10^{11} $eV^{-1}cm^{-2}$, respectively, and the corresponding D_{it} as a function of energy bandgap is shown in Fig. 5.7(c).

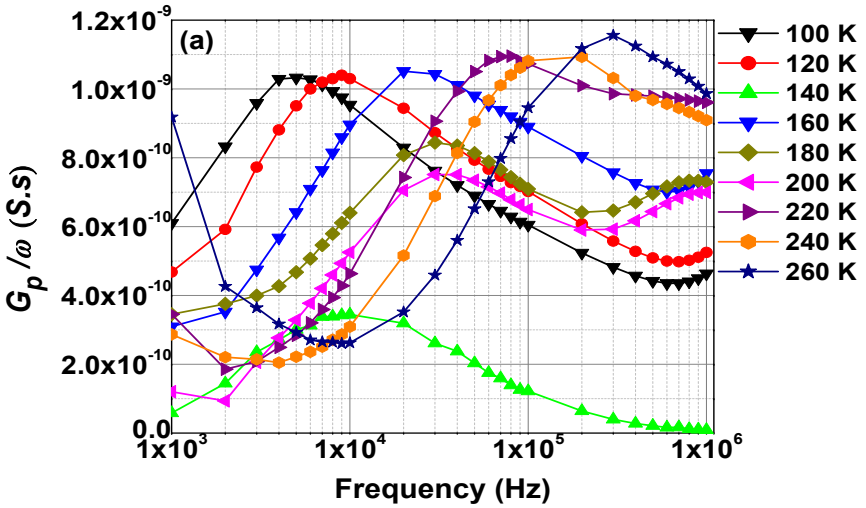

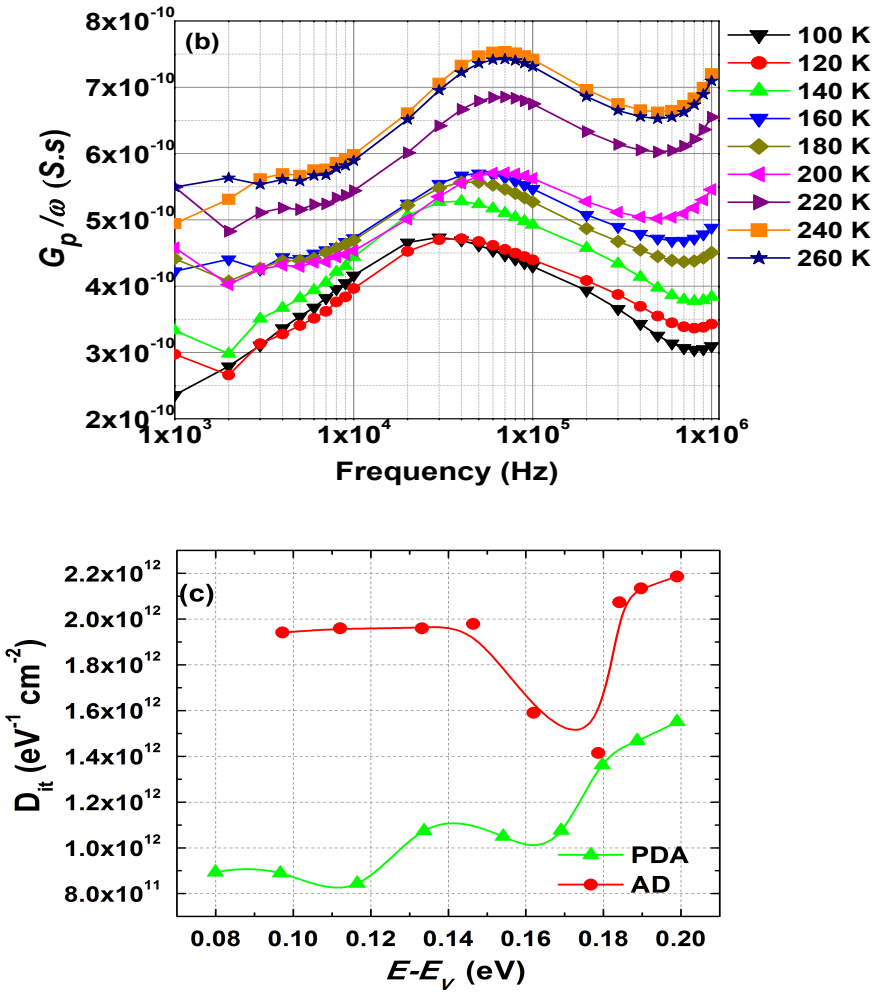

Figure 5.7: Measured G_p/ω as a function of applied AC frequency at different temperatures for the (a) AD films, (b) PDA films and (c) extracted interface-trap charge density as a function of the band-gap energy.

Table 5.2: Extracted Q_f and D_{it} at 300K for AD and PDA films. The + and − polarities represent positive and negative fixed charges in the Al_2O_3 film, respectively.

Sample	**No. of samples**	Q_f **(cm^{-2})**	D_{it} **(eV^{-1}cm^{-2})**
AD	10	$+ (8.1–33.0) \times 10^{11}$	$(1.2–3.4) \times 10^{12}$
PDA	10	$- (9.4–20.0) \times 10^{12}$	$(8.1–15.0) \times 10^{11}$

Table 5.2 represents the range of Q_f and D_{it} values extracted for the AD and PDA films in the depletion to mid-gap voltage regimes at 300 K on several devices (mapping). These results indicate an improved chemical passivation for the PDA samples compared with the AD samples. However, the D_{it} values obtained for the PDA samples are slightly higher than those obtained for the ALD Al_2O_3 films on silicon surfaces [9-12]. One possible reason for such low D_{it} values on silicon surfaces is the growth of a thin (1–2 nm) SiO_x interfacial layer, which improves the chemical passivation quality at the Al_2O_3 /*c*-Si interface [58]. This leaves sufficient room for further research on the interface chemistry of Al_2O_3 /CIGS that is beyond the scope of this study.

The passivation quality achieved by the AD and PDA films were further investigated by estimating the minority carrier concentration at the CIGS surface. These estimations were performed

using a one-dimensional numerical solar cell capacitance simulator (SCAPS-1D) model of an Al/Al_2O_3/CIGS/Mo structure. In order to maintain the electrical contact in such 1D simulations, the Al_2O_3 films were modeled with characteristics similar to the CIGS thin film; these films differ only with respect to thickness (22.5 nm). The mean values of the experimentally extracted Q_f and D_{it} range shown in Table 5.2 were inputted as bulk (i.e. in the 22.5nm Al_2O_3 layer) and interface (i.e. in-between Al_2O_3/CIGS) charges in the simulator, respectively, where the CIGS baseline parameters for the simulations were obtained from Ref. [103] and is given in Appendix C.

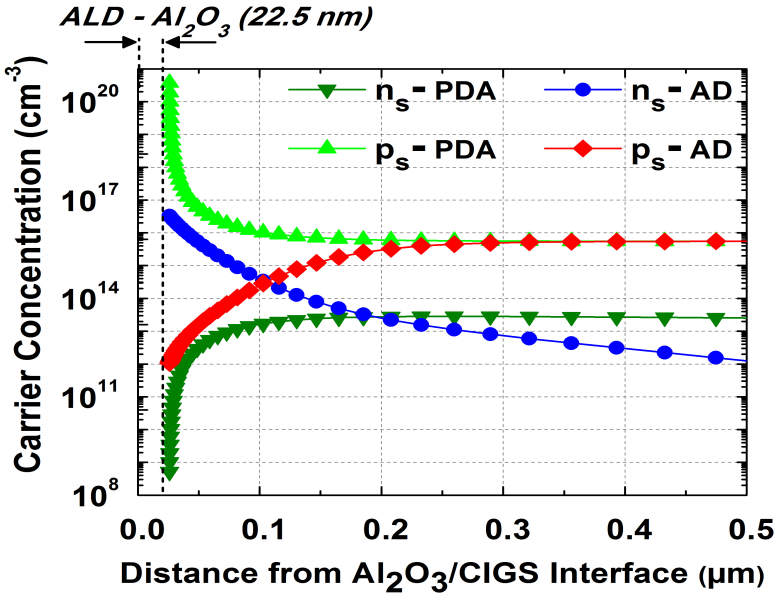

Figure 5.8: Numerically simulated surface concentration of electrons and holes for the AD and PDA films for a uniform CIGS acceptor concentration of $N_A = 5 \times 10^{15}$ cm^{-3} under one-sun illumination conditions (100 mW/cm^2, air mass 1.5).

Fig. 5.8 represents the n_s and p_s concentration profiles estimated using SCAPS simulations for the AD and PDA films as a function of distance from the Al_2O_3/CIGS interface. These estimations were performed using the films corresponding Q_f and D_{it} values. The results suggest that for the AD films, because of the presence of positive fixed charges (Q_f), an inversion layer of minority charges (i.e., $n_s > p_s$) is formed beneath the Al_2O_3 film. In contrast, in the PDA films, the high density of negative Q_f in the bulk of the Al_2O_3 film drives the CIGS surface into accumulation mode (i.e., $p_s > n_s$). Under such accumulation conditions, the valence and conduction bands bend upwards, resulting in a built-in electric field that hinders the minority carriers (i.e., up hill for electrons) from recombining at the interface [98]. The surface concentration of minority carriers (n_s) for the PDA films is approximately eight orders of magnitude lower than that for the AD films. Indeed this can reduce the surface recombination rate to a great extent, depending on the magnitude and ratio of electron-to-hole capture cross-sections (σ_n /σ_p) at the Al_2O_3/CIGS interface, reaching levels comparable to those obtained on p-type c-Si surfaces with ALD-Al_2O_3 passivation schemes [9-12].

5.5 Development of the one dimension (1-D) SCAPS simulation Model

In addition to the solar cell results (with a fixed absorber layer thickness of t_{CIGS}=0.4 μm) presented in Section 5.2, other solar cells with varying absorber layer thickness (i.e. t_{CIGS}=0.24 μm, 0.40 μm, 1.10 μm, 1.58 μm) were realized and the corresponding V_{oc} and J_{sc} results against the reference (unpassivated cells) were given in Table

5.3. Interestingly, these cell results exhibit an increasing gain (abs%) in the cell performance (i.e. V_{oc} and J_{sc}) for decreasing absorber layer thickness (i.e. from 1.58 μm to 0.24 μm).

Table 5.3: ***shows the average values of V_{oc} and J_{sc} for 0.5 cm^2 unpassivated reference cells (ref cell) and Al_2O_3 passivated cells (pass cell) for different CIGS thickness [98].***

t_{CIGS} (um)	# cells	V_{oc} (mV)		J_{sc} (mA/cm^2)	
		ref cell	*pass cell*	*ref cell*	*pass cell*
0.240	*4*	*602*	*659*	*19.6*	*23.3*
0.500	*6*	*576*	*644*	*23.2*	*30.2*
1.100	*10*	*608*	*645*	*29.4*	*29.0*
1.580	*10*	*627*	*640*	*30.5*	*29.0*

Hence, to fully understand the underlying mechanisms for such *absorber layer thickness dependent passivation effects*, a simplified one-dimensional (1-D) SCAPS simulation model has been developed by inserting the rear Al_2O_3 film in between the CIGS and Mo back contact, where the Al_2O_3 film in the SCAPS simulation model accommodates the experimentally extracted electronic properties given in Table 5.2 of Section 5.3.

Implementing the negative fixed charges in the SCAPS-Al_2O_3 layer is achieved based on the well know fact "Al_2O_3 films contain excess Al vacancies and/or oxygen interstitials that are of *deep acceptor types"* [100]. Hence for the sake of simulation purposes (i.e.

to sustain the electrical contact in such 1D simulations), Al_2O_3 films with similar characteristics to the CIGS film were chosen; but only differ in thickness (15nm), while the Q_f and D_{it} in the Al_2O_3 film are implemented as a uniform distribution of *single-acceptor type* in the bulk of the Al_2O_3 films and neutral Gaussian type distribution at the CIGS/Al_2O_3 interface, respectively [98-101].

5.5.1 Validation of the one dimension (1-D) SCAPS simulation Model

In order to validate the passivation effects of Al_2O_3 films on the CIGS absorber, the proposed 1-D simulation model is first validated on a simplified M-I-S structure consisting of Mo/Al_2O_3/CIGS. Capacitance Voltage (C-V) characteristics were generated for varying densities of Q_f and D_{it} for a fixed absorber thickness (1 μm).

Fig. 5.9 shows the simulated C-V characteristics at 10 kHz for Al_2O_3 passivated CIGS MIS capacitor biased from -5V to 5V for a fixed D_{it} of $1x10^{12}$ (cm^{-2} eV^{-1}) and varying Q_f. It is observed that the flat-band voltage of the C-V curves shift towards positive gate voltages, with increasing acceptor type defect density in the bulk of the Al_2O_3 layer, meaning that the negative fixed charges in the SCAPS-Al_2O_3 layer was effectively implemented [103-105].

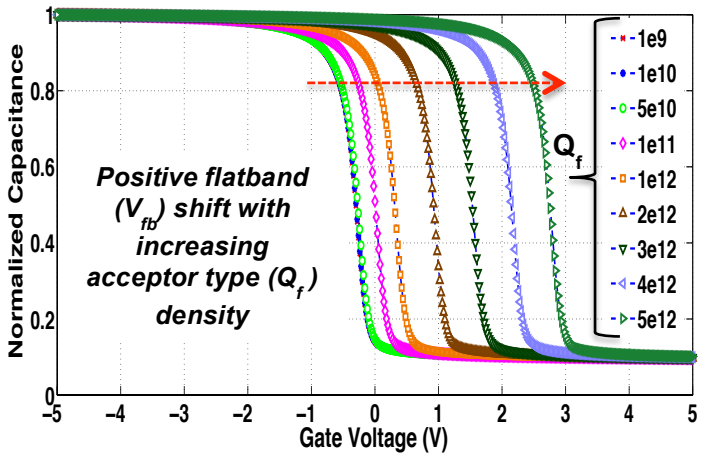

Figure 5.9: Simulated C-V characteristics of $Mo/Al_2O_3/CIGS$ (M-I-S) capacitor using 1D-SCAPS simulation model for varying Q_f and fixed D_{it} =1x10 ^{12} eV^{-1} cm^2

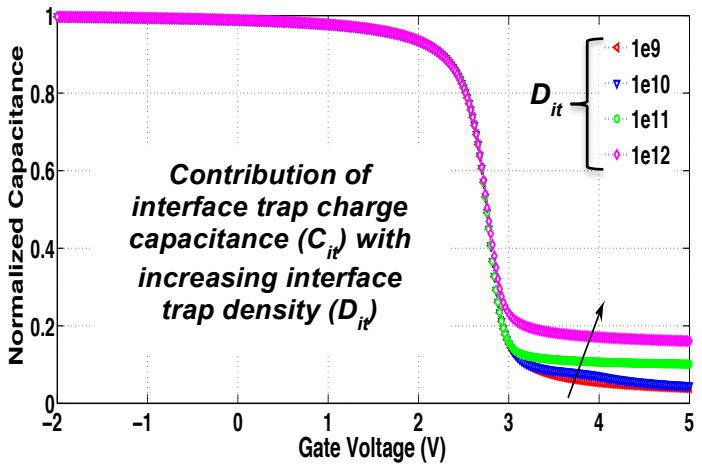

Figure 5.10: Simulated C-V characteristics of $Mo/Al_2O_3/CIGS$ (M-I-S) capacitor using 1D-SCAPS simulation model for varying D_{it} and fixed Q_f = - 8x10 ^{12} cm^{-2}

Secondly, Fig. 5.10 shows the C-V characteristics at 1kHz for varying interface trap charge densities (D_{it}) for a constant Q_f= -8x10^{12} cm^{-2}. This has been accomplished by varying the defect density at the CIGS/Al_2O_3 interface. From the obtained C-V characteristics, we observed the contribution of interface trap charges capacitance (C_{it}) in the inversion voltage regime with increasing D_{it} (i.e. the SCAPS-model accommodates well the chemical passivation effect) [105].

5.5.2 Analysis of Al_2O_3 rear surface passivation effects using 1D-SCAPS

After validating the Al_2O_3 passivation effects on CIGS absorber layers using simplified M-I-S structures: SCAPS simulations were performed on complete solar cell structures to investigate the influence of *absorber layer thickness dependent passivation effects* (i.e. Al_2O_3 passivation effects for varying absorber layer thickness).

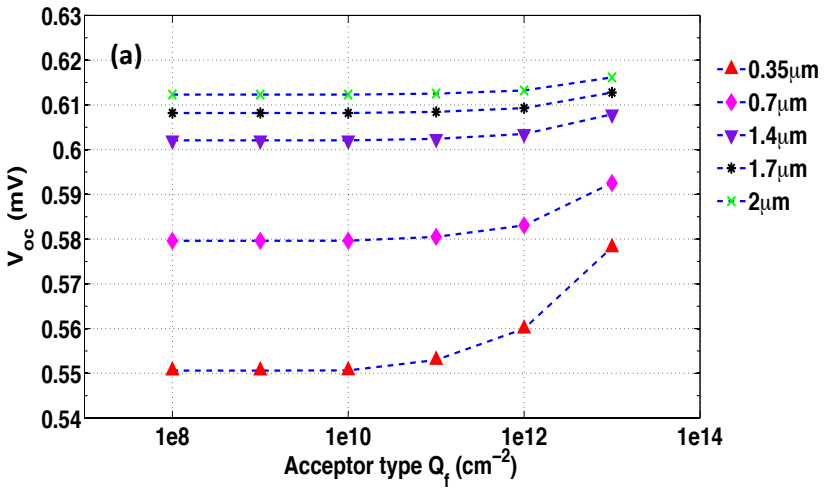

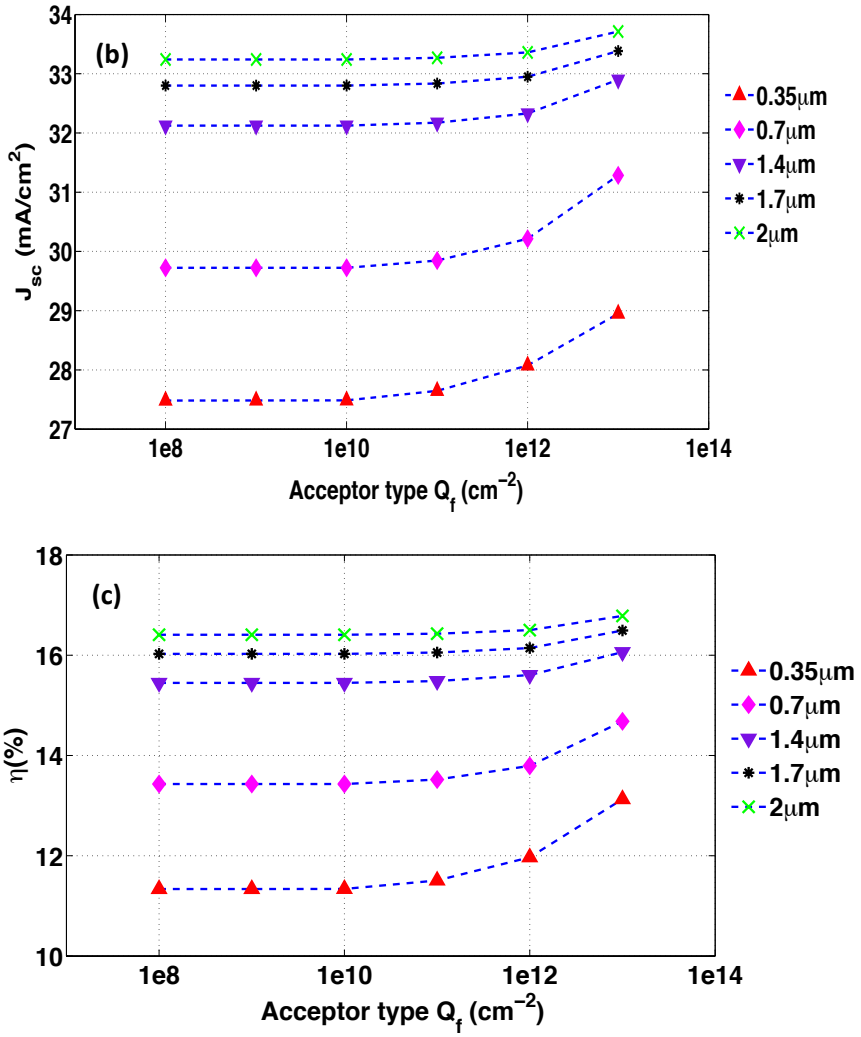

Figure 5.11: Simulated cell parameters; (a) open circuit voltage (b) short circuit current and (c) cell efficiencies as a function of acceptor type (Q_f) densities and CIGS absorber thicknesses.

For this purpose, the Al_2O_3 films are introduced as a rear surface passivation layer in-between the CIGS/Mo back contact (i.e. in a complete CIGS solar cell structure consisting of Mo/Al_2O_3/CIGS/CdS/i-ZnO/ZnO:Al) [105]. Solar cell performance

were analyzed at fixed D_{it}=1x10^{12} cm^{-2} eV^{-1} values (mean values from Table 5.2) and for varying Q_f and CIGS absorber layer thickness as shown in Fig 5.11.

Figs 5.11 (a, b and c) show the simulated cell characteristics of Al_2O_3 passivated CIGS solar cells under illumination. Interestingly, we observe that the influence of field effect passivation is *more predominant for thinner* CIGS absorber layers than the thicker, which agrees well with the experimentally obtained results. This can be explained as follows: From Table 5.1 we observe that the CIGS solar cell performance exhibits strong dependency on the absorber layer thickness variations i.e. thinner absorber films show significant improvement in both V_{oc} and J_{sc} than thicker films with Al_2O_3 rear surface passivation. Firstly, the decrease in V_{oc} with increasing absorber thickness can be explained as follows; due to Al_2O_3 passivation of CIGS/Mo interface, the rear surface recombination velocity (S_b) of the CIGS solar cell gets reduced depending on the quality of both chemical and field-effect passivation. However, the minimum S_b that can be achieved for Al_2O_3 passivated CIGS solar cells is <1x10^2 cm/s [103-107].

Under such low S_b conditions, if the CIGS absorber layer thickness becomes comparable to or even lower than the bulk diffusion length of the minority carriers, then there will be a significant gain in V_{oc} due to considerable *enhancement in the effective diffusion length* of the CIGS solar cell. Contrarily, for CIGS absorber layers thicker than the bulk diffusion length of minority carriers, the influence of lower S_b is

less significant on the effective diffusion length **(**due to increased recombination**)** and therefore only a limited gain in V_{oc} of the solar cell [73,100,101,104].

On the other hand, Table 5.3 also shows a significant gain in J_{sc} for lower thickness. Such dependence of J_{sc} on absorber layer thickness can be explained as follows: for thicker CIGS absorber layers the photo generation of carriers deeper into the CIGS is relatively small and hence lower collection probability. However, for thinner absorber layers due to the presence of high density of negative fixed charges in the bulk of Al_2O_3, the CIGS surface is driven into accumulation mode and both conduction (E_c) and valence (E_v) band-edges are bend up. This band bending at the CIGS/Al_2O_3 have two potential advantages: (i) reduced rear surface recombination due to shielding of minority carriers and maintain high conductivity of majority carriers thereby resulting in an increased V_{oc} (ii) creating *additional drift electric field* (ξ_{drift}) that assists the minority carriers towards the space charge region (SCR) as shown in Fig 5.12.

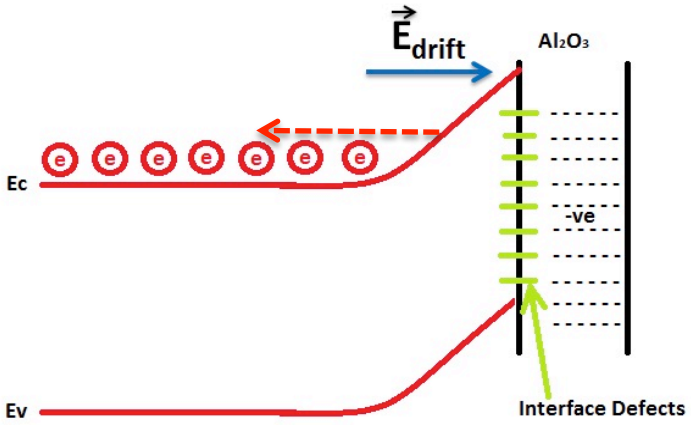

Figure 5.12: Schematic representation of the energy band-diagrams at the CIGS/Al_2O_3 interface

This additional electric field will drift the minority carriers towards SCR by providing *additional diffusion length* (i.e. drift assisted diffusion length enhancement). Hence, significant increase in the collection probability thereby increased J_{sc} for thinner absorber layers due to reduced minority carrier propagation length to the SCR [73,104].

Fig 5.13 represents cell efficiencies for passivated and unpassivated CIGS solar cells for varying absorber thickness. It is observed that significant gain in cell efficiencies have been obtained for thinner absorber thickness due to reduced rear surface recombination in combination with improved collection probability of the minority carriers. Moreover, it was also observed that, the minimum net density of negative fixed charge density (Q_f) required in order to have significant influence on the CIGS cell performances is

around 1x10 ^{12} cm^{-2} [100,104].

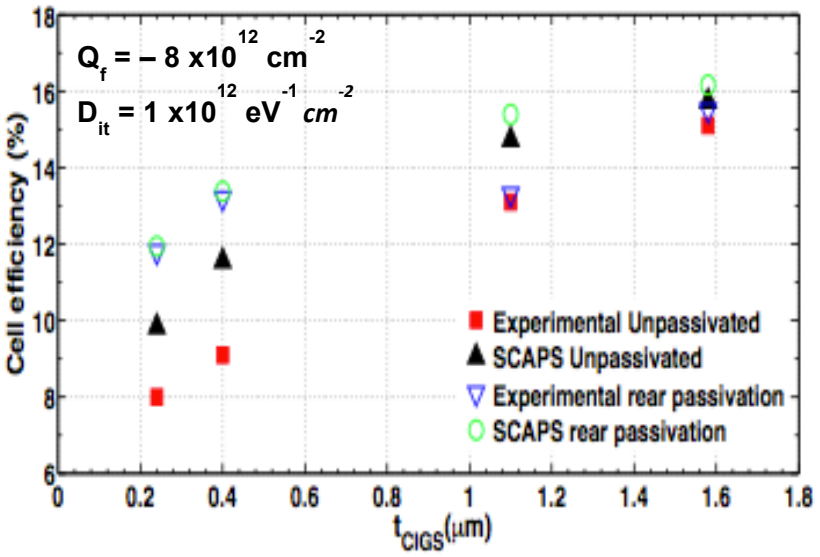

Figure 5.13: Solar cell efficiencies for varying CIGS absorber thickness: experimental (vs) the proposed 1D-SCAPS model

5.6 Summary

Firstly, this work focuses on the progressive cell design concepts from Si solar industry to advance CIGS solar cell performance. DC sputtered Al_2O_3 films (25nm and 50nm) and the unconventional MgF_2/Al_2O_3 and rear surface passivated ultra-thin (t_{CIGS} = 385 nm) CIGS solar cells with nano-sized local rear point contacts are developed, showing a significant increase in V_{oc} and J_{sc} compared with corresponding unpassivated reference cells. This improvement in V_{oc} and J_{sc} has been explained by Al_2O_3 being an adequate surface passivation layer for CIGS interfaces and the thick (MgF_2/)Al_2O_3 layer being highly reflective, respectively. Accordingly,

average solar cell efficiencies of 13.5% are realized for ultra-thin CIGS absorber layers, compared to 9.1% efficiency for the matching unpassivated reference cells. EQE measurements show a clear improvement in absorption of the passivated cells compared with the reference cells, but also indicate that yet again analogous to Si solar cell design further technological improvements can be made to increase J_{sc} even more. This proposed cell design appears to be more complex, but also holds the potential to reduce material/production costs (ever thinner absorber layers) and to increase solar cell efficiencies.

Secondly, the electronic properties of the ALD Al_2O_3/CIGS surfaces and interface have been experimentally extracted for the first time. On the basis of *C–V* and *G-f* measurements, the PDA films exhibit a high density of negative fixed charges in combination with slightly lower interface trap charges as compared to the AD films. This results in a significant reduction of the surface recombination velocity at the Al_2O_3/CIGS interface. Through experimental extractions and numerical simulations, it is evident that the passivation quality improves considerably from AD to post-annealed films, primarily due to the negative fixed charge-induced field-effect passivation over chemical passivation in post-annealed films. This result indicates that the annealing of the ALD Al_2O_3 film plays a vital role in activating the field-effect passivation and in reducing the overall recombination losses at the interface. As a consequence of the excellent passivation quality of the optimized (annealed) ALD Al_2O_3 films, they can be considered as a promising candidate to passivate the CIGS/Mo

interface to substantially enhance the cell performance. we assume that, this work will not only help to understand the passivation mechanism involved at ALD Al_2O_3/CIGS interface, but also to quantify the rear surface passivation quality of the CIGS solar cells i.e. Mo/Al_2O_3/CIGS interfaces in a better way.

Finally, a simple 1D-SCAPS-simulation model has been proposed and validated (using experimental results) to analyze the influence of field effect passivation (i.e. Q_f) on the cell performance for varying CIGS absorber thickness. Through the use of 1D-SCAPS models, we have experimentally and numerically shown that rear surface passivation of CIGS solar cells using Al_2O_3 films plays a vital role in improving the cell performance for thinner CIGS absorber layers. A significant gain was observed in both V_{oc} and J_{sc} for ultra-thin (0.24 um, 0.4 um) absorber films attributed to the additional field-effects introduced by the Al_2O_3 films i.e. accumulation of CIGS surface due to high $Q_{f.}$ offering enhancement in the effective diffusion length of the minority carriers and reducing the rear surface recombination at the CIGS/Al_2O_3/ Mo interface.

CHAPTER 6: SUMMARY AND FUTURE WORKS

6.1 Summary

This thesis work investigates the surface passivation effects of aluminum oxide films on ultra-thin CIGS surfaces and solar cells, in order to reduce the overall electronic recombination losses at the rear CIGS/Mo-interface. And this has been accomplished in a strategic way by choosing the right passivation material based on their (i) interface passivation properties (i.e. SRV, Q_f, D_{it} and thermal stability), (ii) adaptability to CIGS (p-type) surfaces, (iii) deposition properties (i.e. deposition temperatures), and (iv) industrial viability (i.e. deposition rates) for large-scale deployment.

In **Chapter 2**, based on the experimental capacitance-voltage (C-V) and minority carrier lifetime measurements, we have quantified and compared the surface passivation quality of a wide range of conventionally used passivation films; these include the thermally grown-SiO_2, PECVD based SiO_2/Si_3N_4 films, Plasma/Thermal-ALD and DC-sputtered Al_2O_3 films.

Additionally, we have provided the ***figures of merits*** for choosing the best passivation materials taking into account the feasibility and adaptability they offer. The major conclusions that can be drawn from Chapter 2 include (but are not limited to): Al_2O_3 films deposited by both plasma and thermal-ALD deposition technique offer exceptional surface passivation quality on p-type c-Si surfaces with an effective ***SRV < 5 cm.s^{-1}***.

In **Chapter 3**, we show that Al_2O_3 films deposited by ***DC-sputtering technique*** can achieve ***excellent surface passivation properties*** by carefully tuning the deposition, post–deposited annealing conditions. The key findings and conclusions from this chapter include (but not limited):

(i) Optimizing the passivation-activation conditions (i.e. the firing temperatures, duration, gas-flow rate, and atmospheric conditions) for DC-sputtered Al_2O_3 films resulted in an extremely low ***SRV < 7 cms^{-1}*** (***lowest reported value to date for sputtered Al_2O_3 films***).

(ii) The thermal-stability of DC-sputtered Al_2O_3 films was thoroughly examined using various state-of-the-art measurement techniques and characterization tools to investigate the temperature-induced ***interface modifications and their impact*** on the minority carrier lifetime values.

(iii) An alternative method to ***avoid the blister formation*** (due to high temperature firing steps in the solar cell processing) has been proposed, without the use of additional capping layers (such as PECVD-SiO_2, Si_3N_4).

(iv) And finally, it was also shown that the ***passivation quality of DC-sputtered films shows no dependency on the blister formation and evolution***, which is a key finding while considering passivation schemes for CIGS solar cells. Since CIGS deposition (co-evaporated or co-sputtered) undergoes a high temperature *selenization* step (~550ºC for approximately 20 min), where the considered passivation

layer qualification in terms of the thermal stability and quality is of outmost importance (i.e. not to lose its passivation ability).

In **Chapter 4,** we have discussed the benefits offered by gallium (Ga)-grading schemes when implemented in the bulk of CIGS solar cells and their positive impact on the overall cell performances. The key findings in this chapter mainly include (but are not limited to):

(i) Ungraded profile schemes exhibit ***high deep-defect concentrations*** (N_{DLCP}) ~ (5-7) x 10^{15} cm^{-3} close to the depletion region (0.4 um), in addition to ***high densities of trapping states (DOS)*** ~ 4 x 10^{16} cm^{-3} with a trap energy of 113meV (from the valence band) exhibiting defects of type N1 (interface). These electronic properties eventually resulted in an inferior cell performances (16.1%) compared to the other two grading schemes.

(ii) On the other hand, solar cells with back surface grading schemes (BSG) exhibit enhanced cell performance (18.0%) due to gain in both V_{oc} and $J_{sc.}$ The gain in V_{oc} is attributed to the ***slight improvement*** **(i.e. decrease) in the** ***deep-defect concentrations*** (N_{DLCP}) ~ (1.3-2.5) x 10^{15} cm^{-3} and more than ***one-order of magnitude decrease in the DOS*** ~ 2 x 10^{15} cm^{-3}. The gain in J_{sc} can be attributed to the additional drift-electric field, which has been created due to Ga-graded band-gap engineering at the rear surface of the solar cell. Additionally, this shields the minority carrier from being recombined at the CIGS/Mo-interface and will drift the carriers towards SCR (i.e. improved current collection probabilities).

(iii) Finally double sided graded profile scheme exhibits the highest cell performance (18.4%) due to significant increase in both V_{oc} and J_{sc} mainly due to ***further reduction in the DOS*** ~ 8.6 x 10^{14} cm^{-3} ***and deep-defect densities*** (N_{DLCP}) ~ (8.6-35) x 10^{14} cm^{-3} being relatively low when compared to the other grading schemes (UG, BSG).

(iv) Although Ga-grading schemes offer significant enhancements in cell performances, the effects of ***excess-gallium content*** with the bulk of the film can be ***devastating***. Ga itself considered, as an impurity dopant will introduce unwanted deep-defects states within the active region of the solar cells. These unwanted deep defects would act as an ***effective source for the SRH recombination (R-centers),*** thereby reducing the free carrier densities and ***increasing the resistivity of CIGS films***. On the other hand, reducing the usage of gallium is of utmost importance, since the supply of such metals might become an issue if CIGS thin-film solar cells are produced in large volumes due to other industrial applications linked to the gallium usage (ex: LED, jewelry, high-speed switching circuits, infrared circuits, etc.).

Chapter 5 reports several important advancements in ultra-thin CIGS solar cells. And the major findings and *conclusions drawn* from the *results* includes:

(i) Ultra-thin (0.4 µm) *PERC-CIGS solar cells with different* rear surface passivation schemes i.e. *DC-Al_2O_3 (25nm, 50nm), MgF_2 (60nm)/ALD-Al_2O_3 (5nm)* exhibit enhanced cell performance (***an absolute 4.5% improvement)*** compared to the unpassivated reference cells. This improvement is mainly attributed due to the reduced rear

surface recombination (S_b <10^2 cms^{-1}) and increased internal reflection (R_b ~ 40%, 55% and 70%) compared to the unpassivated surfaces (~20%). Moreover, it's also ***important to note that*** the quality achieved by the ***industrial relevant DC-sputtering technique is comparable*** to the low-throughput, expensive precursor (TMA) based conventional ALD deposition technique (based on Chapter 1 SRV < 7 $cm.s^{-1}$ and Chapter 4 improvement (4.1-4.5)% in cell results).

(ii) The ***electronic properties*** at the CIGS/Al_2O_3/Mo-interface have been ***experimentally characterized*** using M-I-S capacitor structures. Very high densities of negative fixed charges Q_f ~ (9.4–20) x 10^{12} cm^{-2} and moderate interface trap densities D_{it} ~ (8.1–15.0) × $10^{11}eV^{-1}$ cm^{-2} were obtained for the post-deposition annealed (PDA) samples (i.e. the ALD-Al_2O_3 films were annealed in selenium (Se) atmosphere at 510ºC to mimic the CIGS cell process as close as possible).

Additionally, SCAPS simulations performed with the extracted interface electronic values show the ***surface concentration of minority carriers (n_s)*** for the PDA films is approximately ***eight orders of magnitude lower*** than the unpassivated as-deposited (AD) films. Indeed this can reduce the surface recombination rate to a great extent (i.e. S_b < 10^2 $cm.s^{-1}$).

(iii) To address the ***influence of Al_2O_3 passivation effects on the CIGS absorber thickness dependency***, we have ***developed and validated a simplified one-dimensional (1-D) SCAPS simulation model***. Experimentally extracted Q_f and D_{it} from C-V characterization were used to validate the proposed model (i.e. implementation of both

chemical and field-effect passivations). Cell characteristics were simulated under AM (1.5) spectral conditions for varying Q_f and CIGS absorber thickness. Simulation results show good agreement with experimental cell results. Moreover, the underlying physical phenomenon that resulted in a predominant gain in the cell performance for thinner absorber layers when compared to the thicker CIGS solar cells has been explained by using the energy band diagrams of CIGS/Al_2O_3 interface. Under low S_b <10^2 cm.s^{-1}, if the CIGS absorber layer thickness becomes less than or even comparable to the bulk diffusion length there will be a significant gain in V_{oc} due to considerable enhancement in the effective diffusion length. Contrarily, for thicker absorber layers, the influence of lower S_b is less significant therefore limiting the gain in V_{oc}. A significant gain in J_{sc} for thinner CIGS with rear passivation can be explained as follows. In thick films, fewer carriers are generated deep into the CIGS absorber layers and have reduced collection probability at the space charge region (SCR). However, for thinner absorber layers, the minority carriers generated beyond the SCR will be drifted towards the SCR due to the additional electric field (ξ_A) induced by the high density of Q_f in the bulk of Al_2O_3.

6.2 Conclusions

In conclusion, this thesis presents significant progress in CIGS surface passivation using industry relevant DC-sputtering and conventional ALD deposited Al_2O_3 films. Together with experimental results and theoretical explanations, we have qualitatively addressed the underlying fundamental mechanisms and their impact on the cell

CIGS cell performance. Furthermore, the results presented in this thesis open new research opportunities/directions to ***reduce the CIGS material usage (by 4-5 times)*** and to further ***improve the cell performances (~ 20%)*** for future low-cost TeraWatt CIGS solar cell production.

6.3 Future works

It is recommended for future work to implement and/or investigate the **(a)** optimal design conditions for the rear-point contact, **(b)** industrial relevant rear-point contact openings, **(c)** effects of nanoparticle (NP) based light reflection techniques, **(d)** choosing the optimal CIGS absorber layer thickness and **(e)** develop and validate 2/3-dimensional simulation models to understand the underlying fundamental mechanisms.

(a) Optimizing the rear contact design: Depending on the quality of the absorbing CIGS film (i.e. diffusion lengths), the rear contact opening pitch needs to be optimized for an effective hole carrier collection. In this case, the passivation layer requires closely spaced (1-2 um pitch) nano-sized (100-400 nm) point openings for electrical contacting. The point contact design should take into account several considerations such as the specific contact resistance, Na diffusion, lateral carrier resistance, passivation and contact coverage area (%), hole mobility, electron diffusion length and the CIGS thickness.

Figure 6.1: Schematic of the rear point contact design

(b) Industrial relevant rear point-contact openings: The dimensions of both point contacts and spacing between contacts are below the limit of conventional photolithography methods and therefore challenging. Roll-to-roll nano-imprint lithography and electron beam (E-beam) lithography are two well-known techniques, which can offer *nano-scale* scalability. However, the former E-beam techniques do not provide industrial viability. Alternatively, more industrially feasible patterning methods should be developed and tested: Nanoparticle lift off, where nano-particles are deposited on top of the Mo back contact, followed by Al_2O_3 passivation layer deposition. And the passivation-layer- covered nano-particles are removed by either chemical etching or by mechanical stress. Nano-particles consisting of CdS have been successfully tested, but also methods using other types of nano-particles such as plastic, glass nano-beads, or nano-colloidal silver, alumina particles should be tested.

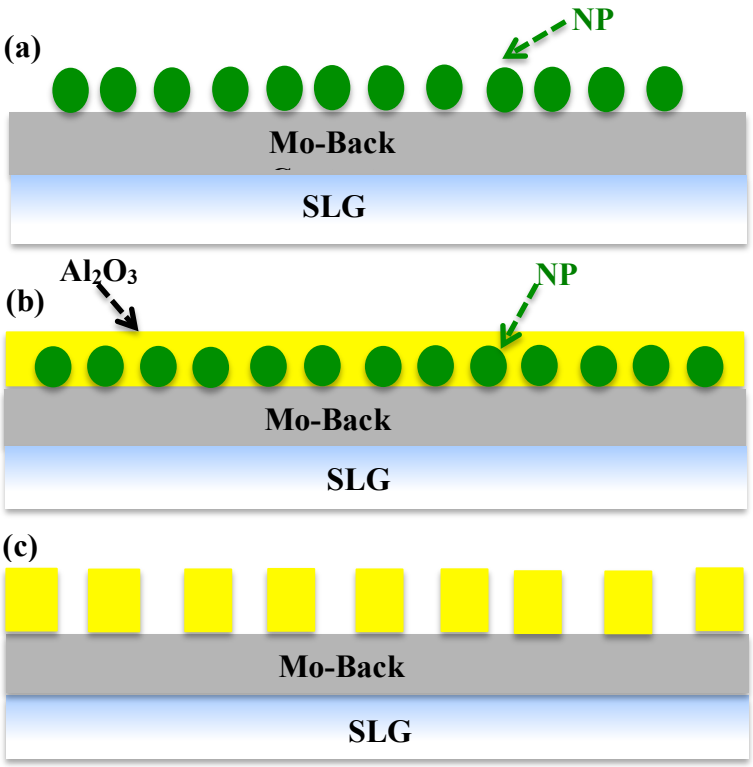

Figure 6.2: (a) Nanoparticle deposition on Mo-back contact, (b) Al_2O_3 passivation layer deposition (c) after removing the nanoparticles using chemical etching and/or by mechanical stress

(c) Nano-structuring the rear metal electrode: Deployment of highly reflective rear surfaces are necessary to overcome the absorption losses in ultra-thin CIGS absorber layers. The investigation should include the optimization of the optical properties of the back electrode metal as well as the nano-structuring of this metal electrode. Optical simulations should be used to optimize the reflection of the rear surfaces within the whole device stack. The rear electrode nano-structuring can performed by using hole colloidal lithography (HCL),

nano-imprint lithography (NIL) in combination with either dry or wet chemical etching.

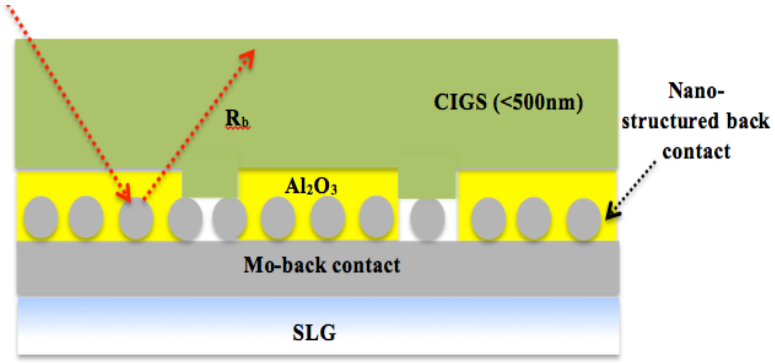

Figure 6.3: Schematic of nano-structured rear metal electrode for enhanced internal reflection.

(d) Optimizing the CIGS quality and thickness: Last but not the least, the quality of CIGS films needs to be improved further for enhanced diffusion lengths. This can be achieved by producing larger grain sizes (by incorporating slightly excess but optimal Cu (%), adequate Na supply, optimal Ga (%)…etc.). Secondly, the CIGS film thickness should be optimized (taking into account the rear field-effect conditions) based on the intrinsic diffusion lengths. Lastly, the stability and reliability of these films needs to be thoroughly addressed using opto-electrical and material characterization techniques.

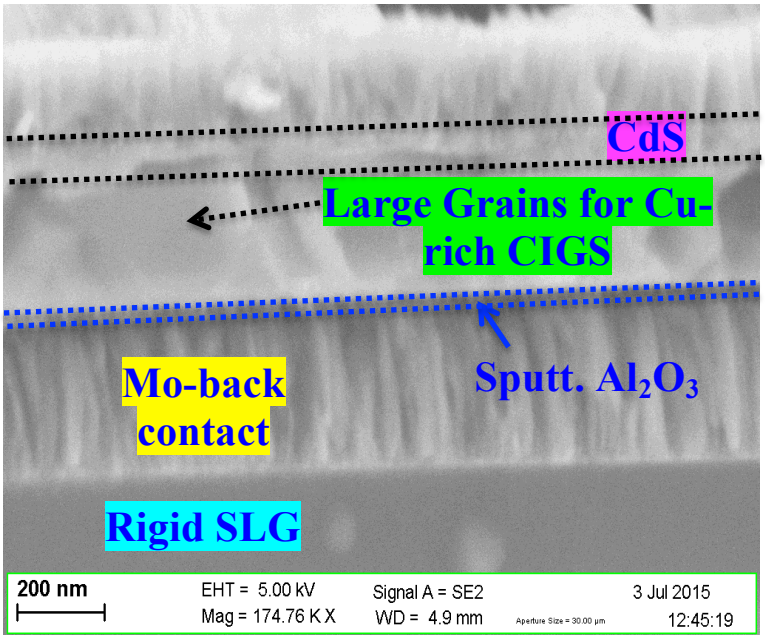

Figure 6.4: Scanning electron microscope (SEM) cross-sectional image of the Cu- rich (large-grain) PERC-CIGS solar cell

(e) To develop and validate simulation models: Due to 2/3-dimensional (D) nature of the highly reflective rear contact and rear interface passivation layers, and polycrystalline structure of the CIGS absorber, the capability of modeling thin-film solar cells in 2/3-D is vital, as opposed to the more commonplace 1D-SCAPS simulations. Additionally, these 2/3-D simulation models assist in providing more realistic learning pathways, to implement the above-mentioned concepts (a-d). Moreover, it is necessary to interpret the impact of each concept, their optimal conditions, and the underlying fundamental mechanisms for a deeper understanding and experimental optimization.

LIST OF PUBLICATIONS

[1] Ratan Kotipalli, Bart Vermang, Viktor Fjällström, Marika Edoff, Romain Delamare, and Denis Flandre "***Influence of Ga/(Ga+In) grading on deep-defect states of Cu(In,Ga)Se$_2$ solar cells***," *Phys. Status Solidi RRL, 1–4 (2015) / DOI 10.1002/pssr.201510024.*

[2] Ratan Kotipalli, Bart Vermang, J.Joel, Rajkumar Jaiswar, Marika Edoff and Denis Flandre, **"*Investigating the electronic properties of Al2O3/Cu(In,Ga)Se2 interface.*"** AIP Advances 5, 107101 (2015); *http://dx.doi.org/10.1063/1.4932512*

[3] R. Kotipalli, R. Delamare, O. Poncelet, X. Tang, L. A. Francis and D. Flandre, **"*Passivation effects of atomic-layer-deposited aluminum oxide",*** *European Physical Journal (EPJ)- Photovoltaics, 4, 45107 (2013), doi:10.1051/epjpv/2013023.*

[4] R. Kotipalli, P. Descamps, R. Delamare, V. Kaiser, G. Beaucarne ,D. Flandre,***"Electronic properties of negatively charged SiO_x films deposited by Atmospheric Pressure Plasma Liquid Deposition for surface passivation of p-Type c-Si Solar Cells***", (article under review for *Thin Solid Films)*

Articles under prepration:

[1] Ratan Kotipalli, Bart Vermang, Marika Edoff and Denis Flandre, **"*On the development and analysis of a 1-D simulation model to address the Al_2O_3 rear surface passivation effects on CIGS solar cells"*** (*for Phys. Status Solidi RRL solar-2016*).

[2] Ratan Kotipalli, Bart Vermang, L.A Francis, O. Poncelet, F. Ureña, J.P Raskin, Marika Edoff, and Denis Flandre, "***Influence of Mo back contact schottky barrier rectification on Cu-rich CIGS solar cell performance***" (*for RCS advances- 2016).*

[3] Ratan Kotipalli, Bart Vermang, Marika Edoff and Denis Flandre, ***"Deep-level capacitance profiling (DLCP) of CIGS absorber layers using simplified M-I-S structures"*** (for *Applied Phys letters -2016*).

Contributions:

[1] B. Vermang, J. T. Wätjen, V. Fjällström, F. Rostvall, M. Edoff, **R. Kotipalli**, F. Henry and D. Flandre, **"*Employing Si solar cell technology to increase efficiency of ultra-thin Cu(In,Ga)Se$_2$ solar cells***", *Progress in Photovoltaics: Research and Applications published,* 22, 1023–1029 (2014), doi:10.1002/pip.2527.

[2] Bart Vermang ,Jörn Timo Wätjen,Viktor Fjällström, Fredrik Rostvall, Marika Edoff, Rickard Gunnarsson, Iris Pilch, Ulf Helmersson, **Ratan Kotipalli**, Frederic Henry, Denis Flandre, **"*Highly reflective rear surface passivation design for ultra-thin Cu(In,Ga)Se$_2$ solar cells***", *Thin Solid Films, Volume 582, 1 May 2015, Pages 300–303, doi:10.1016/j.tsf.2014.10.050*

[3] Pierre Descamps, Salman Syed Asad, Vincent Kaiser, Frederik Campeol, Izabela Kuzma- Filipek, Filip Duerinckx, Jozef Szlufcik, Denis Flandre, **Raja Kotipalli,** Romain Delamare, Guy Beaucarne**,** **"*Deposition of a SiO_X film showing enhanced surface passivation*",** *Energy Procedia, Vol-55, 769-776 (2014),*

[4] O. Poncelet, G. Tallier, S. R. Mouchet, A. Crahay, J. Rasson, **R. Kotipalli**, O. Deparis, L. A. Francis,"***Vapour sensitivity of an ALD hierarchical photonic structure inspired by Morpho***" (*under review for IOP science Bioinspiration & Biomimetics- Jan 2016*)

Patent:

[1] EU-patent (process started with the LTTO of UCL): **"Surface passivation of trap-rich black silicon surfaces"**

Conferences proceedings/posters:

[1] R. Delamare, M. Yedji, J. Demarche, G. Terwagne, **R. Kotipalli**, D. Flandre, ***High-Density Array of Size-Controlled Silicon Nanodots for Si Solar Cells***, In: *Proceedings of the 26th European Photovoltaic Solar Energy Conference* and *Exhibition, Hamburg*, Germany-2011.

[2] Kotipalli, Ratan; Delamare, Romain; Haslinger, M.; Francis, Laurent; Flandre, Denis. ***"Passivation study of aluminium oxide deposited by atomic layer deposition"***, In: *Posters session of the 2012 Photovoltaic Technical Conference (PVTC) Aix-en-Provience, France*-2012.

[3] Kotipalli, Ratan, Delamare, Romain, Francis, Laurent Flandre, Denis. ***"Study of passivation mechanisms induced by negative charge Al2O3 films"***. In: *Proceedings of the* 27th European Photovoltaic Solar Energy Conference and Exhibition, Frankfurt Germany- 2012.

[4] Kotipalli, Ratan, Delamare, Romain, Henry, Frédéric, Proost, Joris, Flandre, Denis. "***Thermal stability analysis of DC-sputtered Al2O3 films for surface passivation of C-Si solar cells".*** In: *Proceedings of the 28th European Photovoltaic Solar Energy Conference and exhibition, Paris, France-2013*.

[5] Kotipalli, Ratan, Delamare, Romain, Henry, Frédéric, Proost, Joris, Flandre, Denis. "***Thermal stability analysis of DC-sputtered Al2O3 films for surface passivation of C-Si solar cells".*** In: *Posters session (S4.78) of the MRS Spring Meeting & Exhibit April 1-5, San Francisco, California, USA-2013*.

[6] Vermang, Bart, **Kotipalli, Ratan**, Flandre, Denis, Gordon, Ivan and Edoff, Marika ***Electrical passivation of thin film solar cell interfaces.*** *32nd European Photovoltaic Solar Energy Conference and exhibition, Munich, Germany-2016*

Invited/Oral Presentations:

[1] R. Kotipalli, B. Vermang, M. Edoff and D. Flandre " ***Review on the rear surface passivation of Cu(In,Ga)Se2 solar cells***"(Invited speaker at Thin-Films Conference–Singapore, July-2016.

[2] Ratan Kotipalli, Bart Vermang, Marika Edoff, Rajkumar Jaiswar and Denis Flandre, "***On the development and analysis of a simulation model for Al_2O_3 rear surface passivated Cu(In,Ga)Se_2 solar cells*****"** (oral presentation at PVTC-France –May 29 at 11.30 am, 2015) .

[3] Ratan Kotipalli, Bart Vermang, Marika Edoff, and Denis Flandre "***Electrical characterization of graded and Al_2O_3 passivated CIGS solar cell".*** International seminar on Solar Photovoltaic Research and Applications: Ångström Solar Center, Uppsala University-Sweden, Feb-4th, 2015

[4] Ratan Kotipalli, Bart Vermang, Marika Edoff, and Denis Flandre, "***Surface Passivation of High Efficiency CIGS Solar Cells by DC-Sputtered Al_2O_3 Films"***, 2-WINFAB day, Louvain, Belgium- 2014.

BIBLIOGRAPHY

[1] International Energy Agency (IEA) Publications: Technology Roadmap: Solar Photovoltaic Energy - 2014 edition, IEA Publication, Paris, France, 2014.

[2] G. Masson, M. Latour, M. Rekinger, I.-T. Theologitis, and M. Papoutsi, "EPIA: Global Market Outlook for Photovoltaics 2013-2017," European Photovoltaic Industry Association, Brussels, 2014

[3] RM Swanson, "Approaching the 29% limit efficiency of silicon solar cells," Proceedings of 31st IEEE Photovoltaic Specialists Conference, Lake Buena Vista, FL, USA, pp. 889-894, 2005

[4] M. Taguchi, Ayano, S. dohodak. Matsuyama, Y. Nakamura, T. Nishiwaki, K. Fujita, and E. Maruyama, "24.7% Record Efficiency HIT Solar Cell on Thin Silicon Wafer," IEEE Journal of Photovoltaics, vol. 4, pp. 96-99, 2014

[5] AG Aberle, PP Altermatt, G. Heiser, SJ Robinson, AH Wang, JH Zhao, U. Crookshanks, and MA Green, "Limiting loss mechanisms in 23-percent efficient silicon solar cells," Journal of Applied Physics, vol. 77, pp. 3491-3504, 1995.

[6] AG Aberle, "Surface passivation of solar cells Crystalline Silicon: A Review," Progress in Photovoltaics, vol. 8, pp. 473-487, 2000.

[7] R. B. M. Girisch, R. P. Mertens, and R. F. De Keersmaecker, "Determination of Si-SiO2 interface recombination parameters using a gate-controlled point- junction diode under illumination," IEEE Transactions on Electron Devices, vol. 35, pp. 203-222, 1988.

[8] F. W. Chen, "PECVD Silicon Nitride for n-type Silicon Solar Cells," PhD thesis, University of New South Wales, Sydney, Australia, Sydney, 2008.

[9] J. Tan, A. Cuevas, S. Winderbaum, and K. Roth, "Thermal stability of the passivation of phosphorus diffused silicon surfaces by PECVD silicon nitride," Proceedings of 20th European Photovoltaic Solar Energy Conference, Barcelona, Spain, pp. 1297-1300, 2005.

[10] R. Hezel and K. Jaeger ,"Low-temperature surface passivation of silicon for solar cells," Journal of the Electrochemical Society, 136 (2), 518–523 (1989).

[11] G. Agostinelli, A. Delabie, P. Vitanov, Z. Alexieva, H. F. W. Dekkers, S. De Wolf, and G. Beaucarne, "Very low surface recombination velocities on p-type silicon wafers passivated with a dielectric with fixed negative charge," Solar Energy Materials and Solar Cells, vol. 90, pp. 3438-3443, 2006.

[12] B. Hoex, JH Gillis, MCM van de Sanden, and WMM Kessels, "On the c-Si surface passivation mechanism by the negative-charge-dielectric Al2O3," Journal of Applied Physics, vol. 104, pp. 113703-113707., 2008.

[13] G. Dingemans, M. C. M. van de Sanden, and W. M. M. Kessels, "Excellent Si surface passivation by low temperature SiO_2 using an ultrathin Al_2O_3 capping film," Physica Status Solidi – Rapid Research Letters, vol. 5, pp. 22-24, 2011.

[14] J. Schmidt, F. Werner, B. Veith, D. Zielke, R. Bock, V. Tiba, P. Poodt, F. Roozeboom, A. Li, A. Cuevas, and R. Brendel, "Industrially Relevant Al_2O_3 Deposition Techniques For The Surface Passivation Of Si Solar Cells", pp. 4–7, September 2010.

[15] J. Schmidt, A. Merkle, B. Hoex, M. C. M. van de Sanden, W. M. M. Kessels, and R. Brendel, "Atomic-layer-deposited aluminum oxide for the surface passivation of high-efficiency silicon solar cells," IEEE Photovoltaic Specialists Conference (PVSC), pp. 1–5, May 2008.

[16] F. Colville, “PERC capacity hits 2.5GW and offers new technology buy cycle option”, PV-Tech, August 2014.

[17] E. Urrejola, R. Petres, J. G. Reichenbach, K. Peter, E. Wefringhaus, H. Plagwitz, G. Schubert," High Efficiency Industrial PERC Solar Cells with all PECVD-Based Rear Surface Passivation”, in Proc. 26th European Photovoltaic Solar Energy Conference and Exhibition (EU PVSEC), pp 2233 – 2235, 2011.

[18] J. Zhao, A. Wang, and M. A. Green, "24·5% Efficiency silicon PERT cells on MCZ substrates and 24·7% efficiency PERL cells on FZ substrates," Progress in Photovoltaics: Research and Applications, vol. 7, pp. 471-474, 1999.

[19] G. Agostinelli, J. Szlufcik, P. Choulat, and G. Beaucarne, “Local contact structures for industrial PERC-type solar cells,” in Proc. 20th European Photovoltaic Solar Energy Conference and Exhibition (EU PVSEC)., 2005, pp. 942–945.

[20] Beaucarne, G., Schubert, G., Hoornstra, J., Horzel, J., and Glunz, S.W., “*Summary* of the *Third Workshop* on *Metallization* for *Crystalline Silicon Solar Cells*,” *Energy Procedia,* Volume 21, 2012, Pages 2–13, 2012.

[21] K.O. Davis, K. Jiang, C. Demberger, H. Zunft, H. Haverkamp, D. Habermann, and W. V. Schoenfeld, “Investigation of the internal back reflectance of rear-side dielectric stacks for c-Si solar cells,” IEEE Journal of Photovoltaics, vol. 3, no. 2, pp. 641–648, April 2013.

[22] A. Lorenz, J. John, B. Vermang, E. Cornagliotti, and J. Poortmans, “Com- parison of illumination level dependency and rear internal reflectance of PERC-type cells with different dielectric passivation stacks,” in *Proc. 26th Eur. Photovoltaic Sol. Energy Conf.*, 2011, pp. 1486–1488.

[23] Udai P. Singh and Surya P. Patra, “Progress in Polycrystalline Thin-Film Cu(In,Ga) Solar Cells,” International Journal of Photoenergy, vol. 2010, Article ID 468147, 19 pages, 2010.

[24] P. Reinhard, A. Chirila, P. Blosch, F. Pianezzi, S. Nishiwaki, S. Buecheler, and A. N. Tiwari, “Review of progress toward 20% efficiency flexible CIGS solar cells and manufacturing issues of solar modules,” IEEE J. Photovoltaics, vol. 3, no. 1, pp. 572–580, Jan. 2013.

[25] P. Jackson, D. Hariskos, E. Lotter, S. Paetel, R. Wuerz, R. Menner, W. Wischmann, and M. Powalla, “New world record efficiency for Cu(In,Ga)Se2 thin-film solar cells beyond 20%,” Prog. Photovoltaics, Res. Appl., vol. 19, pp. 894–897, 2011.

[26] M. A. Contreras et al., "On the role of Na and modifications to Cu(In,Ga)Se2 absorber materials using thin-MF (M=Na, K, Cs) precursor layers [solar cells]," 26th IEEE PVSC, pp. 359-362,1997.

[27] D. Rudmann et al., “Effects of NaF coevaporation on structural properties of Cu(In,Ga)Se-2 thin films,” *Thin Solid Films,* **431**,pp. 37-40, 2003.

[28] D Soubane, A Ihlal, G Nouet,"The Role Of Cadmium Oxide Within The Thin Films Of The Buffer Cds Aimed At Solar Cells Based Upon CIGS Films Fabrication",Journal of Condensed Matter, 9, 2007.

[29] R. Kotipalli, B.Vermang, V. Fjällström, M.Edoff, R.Delamare and D.Flandre,"Influence of Ga/(Ga + In) grading on deep-defect states of Cu(In,Ga)Se2 solar cells",(RRL) - Rapid Research Letters,Volume 9, Issue 3, pp 157–160, March 2015

[30] A. Chirilă, P. Reinhard, F. Pianezzi, P. Bloesch, A. R. Uhl, C. Fella, L. Kranz, D. Keller, C. Gretener, H. Hagendorfer, D. Jaeger, R. Erni, S. Nishiwaki, S. Buecheler, and A. N. Tiwari, "Potassium-induced surface modification of Cu(In,Ga)Se_2 thin films for high-efficiency solar cells", Nature Materials 12, 1107 (2013).

[31] National Center for Photovoltaics, "NREL," 2013.

[32] B. Vermang, V. Fjallstrom, J. Pettersson, P. Salome´, and M. Edoff, "Devel- opment of rear surface passivated Cu(In,Ga)Se2 thin film solar cells with nano-sized local rear point contacts," Solar Energy Mater. Solar Cells, vol. 117, pp. 505–511, 2013.

[33] M. L. Green, E. P. Gusev, R. Degraeve, and E. L. Garfunkel, "Ultrathin (< 4 nm) SiO(2) and Si-O-N gate dielectric layers for silicon microelectronics: Understanding the processing, structure, and physical and electrical limits," Journal of Applied Physics, vol. 90, pp. 2057-2121, 2001.

[34] A. Cuevas, M.J. Kerr, J. Schmidt,"Passivation of crystalline silicon using silicon nitride", Proc. 3rd World Conf. Photovoltaic Solar Energy Conversion, Osaka, Japan, pp. 913–918,2003.

[35] S. Duttagupta, F.-J. Ma, B. Hoex, and A. G. Aberle, "Excellent surface passivation of heavily doped p+ silicon by low-temperature plasma-deposited SiOx/SiNy dielectric stacks with optimised antireflective performance for solar cell application," Solar Energy Materials and Solar Cells, vol. 120, Part A, pp. 204-208, 2014.

[36] C. Leguijt, P. Lölgen, J. A. Eikelboom, A. W. Weeber, F. M. Schuurmans, W. C. Sinke, P. F. A. Alkemade, P. M. Sarro, C. H. M. Marée, and L. A. Verhoef, "Low temperature surface passivation for silicon solar cells," Solar Energy Materials and Solar Cells, vol. 40, pp. 297-345, 1996.

[37] U. K. Das, M. Z. Burrows, M. Lu, S. Bowden, and R. W. Birkmire, "Surface passivation and heterojunction cells on Si (100) and (111) wafers using dc and rf plasma deposited Si:H thin films," Applied Physics Letters, vol. 92, pp. 063504, 2008.

[38] M. Reed and J. Plummer, "Chemistry of Si-SiO_2 interface trap annealing," Journal of Applied Physics, vol. 63, pp. 5776-5793, 1988.

[39] J. Schmidt, A. Merkle, R. Brendel, B. Hoex, M.C.M. van de Sanden, W.M.M. Kessels,"Surface passivation of high-efficiency silicon solar cells by atomic-layer-deposited Al2O3," Prog. Photovolt. Res. Appl., 16, p. 461,2008.

[40] B. Hoex, S.B.S. Heil, E. Langereis, M.C.M. van de Sanden, W.M.M. Kessels,"Ultralow surface recombination of c-Si substrates passivated by plasma-assisted atomic layer deposited Al2O3," Appl. Phys. Lett., 89, p. 042112,2006.

[41] N.M. Terlinden, G. Dingemans, M.C.M. van de Sanden, W.M.M. Kessels,"Role of field-effect on c-Si surface passivation by ultrathin (2-20 nm) atomic layer deposited Al2O3", Appl. Phys. Lett., 96, p. 112101,2010.

[42] F. Werner, B. Veith, D. Zielke, L. Kühnemund, C. Tegenkamp, M. Seibt, R. Brendel, J. Schmidt,"Electronic and chemical properties of the c-Si/Al2O3 interface, J. Appl. Phys., 109, p. 113701,2.011.

[43] R. Kotipalli, R. Delamare, O. Poncelet, X. Tang, L.A. Francis, D. Flandre, "Passivation effects of atomic-layer-deposited aluminium" EPJ Photovoltaics, Vol. 4, no. 45107, p. 1-8, 2013.

[44] E.H. Nicollian, J.R. Brews. MOS (Metal Oxide Semiconductor) Physics and Technology, Wiley, New York (1982).

[45] D. K. Schroder, Semiconductor material and device characterization, John Wiley & Sons Inc., Hoboken, New Jersey, USA, 3rd edition, 2006.

[46] R. Castagne´, "Determination of the Slow Density of an MOS Capacitor Using a Linearly Varying Voltage," (in French) C.R. Acad. Sc. Paris 267, 866–869, Oct. 1968; M. Kuhn, "A Quasi-Static Technique for MOS C-V and Surface State Measurements," Solid-State Elec- tron. 13, 873–885, June 1970.

[47] W.K. Kappallo and J.P. Walsh, "A Current Voltage Technique for Obtaining Low-Frequency C-V Characteristics of MOS Capacitors," Appl. Phys. Lett. 17, 384–386, Nov. 1970.

[48] J. Koomen, "The Measurement of Interface State Charge in the MOS System," Solid-State Electron. 14, 571–580, July 1971; K. Ziegler and E. Klausmann, "Static Technique for Precise Measurements of Surface Potential and Interface State Density in MOS Structures," Appl. Phys. Lett. 26, 400–402, Apr. 1975.

[49] J. R. Brews and E.H. Nicollian, "Improved MOS Capacitor Measurements Using the Q-C Method," Solid-State Electron. 27, 963–975, Nov. 1984.

[50] R. Castagne´ and A. Vapaille, "Description of the SiO_2-Si Interface Properties by Means of Very Low Frequency MOS Capacitance Measurements," *Surf. Sci.* **28**, 157–193, Nov. 1971.

[51] R. Castagne´ and A. Vapaille, "Apparent Interface State Density Introduced by the Spatial Fluc- tuations of Surface Potential in an MOS Structure," *Electron. Lett.* **6**, 691–694, Oct. 1970.

[52] L.M. Terman, "An Investigation of Surface States at a Silicon/Silicon Oxide Interface Employ- ing Metal-Oxide-Silicon Diodes," *Solid-State Electron.* **5**, 285–299, Sept./Oct. 1962.

[53] E.H. Nicollian, A. Goetzberger and A.D. Lopez, “Expedient Method of Obtaining Interface State Properties from MIS Conductance Measurements,” *Solid-State Electron.* 12, 937–944, Dec. 1969.

[54] W. Fahrner and A. Goetzberger, “Energy Dependence of Electrical Properties of Interface States in Si–SiO2 Interfaces,” *Appl. Phys. Lett.* **17**, 16–18, July 1970; H. Deuling, E. Klausmann and A. Goetzberger, “Interface States in Si–SiO2 Interfaces,” *Solid-State Elec- tron.* **15**, 559–571, May 1972.

[55] J.R. Brews, “Admittance of an MOS Device with Interface Charge Inhomogeneities,” *J. Appl. Phys.* **43**, 3451–3455, Aug. 1972.

[56] J.J. Simonne, “A Method to Extract Interface State Parameters from the MIS Parallel Conduc- tance Technique,” *Solid-State Electron.* **16**, 121–124, Jan. 1973.

[57] H. Deuling, E. Klausmann and A. Goetzberger, “Interface States in Si–SiO2 Interfaces,” *Solid-State Elec- tron.* **15**, 559–571, May 1972; J.R. Brews, “Admittance of an MOS Device with Interface Charge Inhomogeneities,” *J. Appl. Phys.* **43**, 3451–3455, Aug. 1972

[58] G. Dingemans and W.M.M. Kessels,"Status and prospects of Al2O3-based surface passivation schemes for silicon solar cells".J Vac. Sci. Technol. A, 30 (4), p. 040802, 2012.

[59] R. Kotipalli, R. Delamare, F. Henry, J. Proost, D. Flandre,"Thermal stability analysis of DC-sputtered Al2O3 films for surface passivation of c-Si solar cells", Proc. 28th EU PVSEC; pp 1278–1281, 2013.

[60] M. Kharrazi Olsson, K. Macák, W. Graf.,"Reactive d.c. magnetron sputter deposited Al2O3 films: large-area coatings for industrial applications",Surface and Coatings Technology, Volume 122, Issues 2–3, pp 202-207,1999.

[61] T. Seino and T. Sato .,"Aluminum oxide films deposited in low pressure conditions by reactive pulsed dc magnetron sputtering",J. Vac. Sci. Technol. A 20, 634,2002.

[62] A. A kansha Bansal, P. Srivastava, B. R. Singh .,"On the surface passivation of c-silicon by RF sputtered Al2O3 for solar cell application",Journal of Materials Science: Materials in Electronics, volume 26, Issue 2, pp 639-645,2015.

[63] J. Schmidt, F. Werner, B. Veith, D. Zielke, R. Bock, R. Brendel, V. Tiba, P. Poodt, F. Roozeboom, A. Li and A. Cuevas, 'Surface Passivation of Silicon Solar Cells using Industrially Relevant Al2O3 Deposition Techniques', Photovoltaics International, 10, pp:52–57,2010.

[64] T.-T. A. Li, S. Ruffell, M. Tucci, Y. Mansouli´e, C. Samundsett, S. De Iullis, L. Serenelli and A. Cuevas, 'Influence of Oxygen on the Sputtering of Aluminum Oxide for the Surface Passivation of Crystalline Silicon', Solar Energy Materials and Solar Cells, 95, pp:69–72,2011.

[65] T.-T. A. Li and A. Cuevas, 'Effective surface passivation of crystalline silicon by rf sputtered aluminum oxide', Physica Status Solidi - Rapid Research Letters, 3(5), pp:160–162,2009.

[66] J. Benick, A. Richter, T.-T. A. Li, N. Grant, K. R. McIntosh, Y. Ren, K. J. Weber, M. Hermle and S. W. Glunz, 'Effect of a post-deposition anneal on Al2O3/Si interface properties', Conference Record of the 35th IEEE Photovoltaic Specialists Conference, Honolulu, USA, pp. 891–896, 2010.

[67] B. Vermang. " Aluminum oxide as negatively charged surface passivation for industrial crystalline silicon solar cells". University of Leuven: Leuven, 2012; ISBN: 978-94-6018-531-1.

[68] B. Vermang, H. Goverde, A. Uruena, A. Lorenz, E. Cornagliotti, A. Rothschild, J. John, J. Poortmans, and R. Mertens, “Blistering in ALD Al2O3 passivation layers as rear con- tacting for local Al BSF Si solar cells,” Solar Energy Materials and Solar Cells, vol. 101, pp. 204–209, June 2012.

[69] R. A. Sinton and A. Cuevas, ‘Contactless determination of current-voltage char- acteristics and minority-carrier lifetimes in semiconductors from quasi-steady-state photoconductance data’, Applied Physics Letters, 69 (17), 2510–2512,1996.

[70] P. W. Peacock and J. Robertson, ‘Behavior of hydrogen in high dielectric constant oxide gate insulators’, Applied Physics Letters, 83 (10), pp. 2025–2027 ,2003.

[71] A. R. Chowdhuri, C. G. Takoudis, R. F. Klie and N. D. Browning, ‘Metalorganic chemical vapor deposition of aluminum oxide on Si: Evidence of interface SiO2 formation’, Applied Physics Letters, 80 (22), pp. 4241–4243,2002.

[72] M.A. Contreras, J.R. Tuttle, A. Gabor, A. Tennant, K. Ramanathan, S. Asher, A. Franz, J. Keane, L. Wang, R. Noufi, High efficiency graded bandgap thin-film polycrystal- line Cu(In,Ga)Se2—based solar cells, Solar Energy Mater Sol Cells 41/42, pp. 231-246,1996.

[73] O. Lundberg, M. Edoff, J. Malmstro¨m, L. Stolt, Influence of the Cu(In,Ga)Se2 thickness and Ga-grading on the solar cell performance. Prog. Photovoltaics 11 (2003) 77–88.

[74] A. Gabor, J.R. Tuttle, M.H. Bode, M.A. Franz, A.L. Tennant, M.A. Contreras, R. Noufi, D.G. Jensen, A.M. Hermann, Band- gap engineering in Cu(In,Ga)Se2 thin films grown from (In, Ga)2Se3 precursors, Solar Energy Mater. Sol. Cells 41/42,pp. 247–260,1996.

[75] T. Dullweber, G. Hanna, W. Shams-Kolahi, A. Schwartzlander, M. A. Contreras, R. Noufi, H. W. Schock, Study of the effect of gallium grading in Cu(In,Ga)Se2, Thin Solid Films 361-362,pp. 478–481,2000.

[76] T. Dullweber, Optimierung des Wirkungsgrades von Cu(In,Ga)Se2-Solarzellen mittels variablem Verlauf der Bandluecke, Ph.D. thesis, Universitaet Stuttgart (2002).

[77] J. L. Gray, Y. J. Lee, Numerical modeling of graded band gap CIGS solar cells, in: Proc. 1st World Conf. Photovoltaic Energy Conversion, pp. 123–126, 1994.

[78] M. Topic, F. Smole, J. Furlan, Band-gap engineering in CdS/Cu(In,Ga)Se2 solar cells, J. Appl. Phys. 79 (1996) 8537–8540.

[79] S.-H. Wei, S. B. Zhang, A. Zunger, Effects of Ga addition to CuInSe2 on its electronic, structural, and defect properties, Appl. Phys. Lett. 72 (1998) 3199– 3201.

[80] M. Gloeckler, A. L. Fahrenbruch, J. R. Sites, Numerical modeling of CIGS and CdTe solar cells: Setting the baseline, in: Proc. 3rd World Conf. Photovoltaic Energy Conversion, pp. 491–494,2003.

[81] M. Gloeckler, J. R. Sites, Efficiency limitations for wide-band-gap chalcopyrite solar cells, Thin Solid Films (2005) in press.

[82] T. Dullweber, U. Rau, M. A. Contreras, R. Noufi, H.-W. Schock, Photogeneration and carrier recombination in graded gap Cu(In,Ga)Se2 solar cells, IEEE Trans. Elect. Devices 47,pp. 2249–2254,2000.

[83] D. Abou-Ras, T. Kirchartz, U. Rau. Advanced Characterization Techniques for Thin Film Solar Cells, WILEY-VCH Verlag GmbH & Co. KGaA, Weinheim, 2011.

[84] U. Rau, H. W. Schock, "Electronic properties of Cu(In, Ga)Se2 heterojunction solar cells-recent achievements, current understanding, and future challenges,", Appl. Phys. A, 69, pp. 131-147,1999.

[85] S. Hegedus, W. Shafarman, "Thin-Film Solar Cells: Device Measurements and Analysis", Prog. Photovolt: Res. Appl, 12, 2004, pp. 155-176.

[86] T. Heath, J. D. Cohen, and W. N. Shafarman, "Bulk and MetaStable Defects in CuIn(1-x)Ga(x)Se2 Thin Films Using Drive Level Capacitance Profiling." J. of Applied Physics. 95. 3 (2004).

[87] R. Herberholz, M. Igalson, H.W. Schock,"Distinction between bulk and interface states in CuInSe2/CdS/ZnO by charge spectroscopy", Appl. Phys., 83, p. 318,1998.

[88] T. Walter, R. Herberholz, C. Müller, H.W. Schock,"Determination of defect distribution from admittance measurements and application to Cu(In,Ga)Se2 based heterojunctions",J. Appl. Phys., 80, p. 4411,1996.

[89] R. Scheer, "Activation energy of heterojunction diode currents in the limit of interface recombination,", J. Appl. Phys., 105, pp. 104505(1)-104505(6),2009.

[90] K. W. Böer, Introduction to Space Charge Effects in Semiconductors (Springer-Verlag, Berlin, p. 160, 2010.

[91] R. Scheer and H. W. Schock, Thin film material properties, in: Chalcogenide Photovoltaics: Physics, Technologies, and Thin Film Devices (Wiley-VCH Verlag, Weinheim), p. 112, 2011.

[93] B. Vermang,V. Fjällström ,X. Gao, M. Edoff.," Improved rear surface passivation of Cu(In,Ga)Se2 solar cells: a combination of an Al2O3 rear surface passivation layer and nanosized local rear point contacts"., IEEE Journal of Photovoltaics 4: pp.486–492, 2014.

[95] B. Vermang, J.T. Wätjen, V. Fjällström, F. Rostvall, M. Edoff, R. Kotipalli, F. Henry, and D. Flandre, “Employing Si solar cell technology to increase efficiency of ultra-thin Cu(In,Ga)Se2 solar," Prog. Photovolt. Res. Appl., 22 (10), p. 1023, 2014.

[96] B. Vermang, J. T. Watjen, V. Fjallstrom, F. Rostvall, M. Edoff, R. Gunnarsson, I. Pilch, U. Helmersson, R. Kotipalli, F. Henry, and D. Flandre, “Highly reflective rear surface passivation design for ultra-thin Cu(In,Ga)Se2 solar cells,” Thin Solid Films, 582, 300, 2015.

[97] B. Vermang et al., “Introduction of Si PERC Rear Contacting Design to Boost. Efficiency of Cu(In,Ga)Se2 Solar Cells,” IEEE Journal of. Photovoltaics 2014; 4(6):1644-1649

[98] J. Joel, B. Vermang, J. Larsen, O. Donze-Gargand, and M. Edoff,"On the assessment of CIGS surface passivation by photoluminescence,” Phys. Status Solidi RRL, Phys. Status Solidi RRL, Volume 9, Issue 5, pp 288–292, May 2015.

[99] W. W Hsu, J.Y Chen, T.H Cheng, S.C Lu, W.S Ho, Y.Y Chen, Y.J Chien, C. W Liu, "Surface passivation of Cu(In, Ga)Se2 using atomic layer deposited Al2O3", Applied Physics Letters; 100: 023508, 2012.

[100] M.Choi,A.Janotti and C.G van de Walle,"Native point defects and dangling bonds in α-Al_2O_3”, J. Appl. Phys. 113, 044501 (2013); doi: 10.1063/1.4784114

[101] R. Kotipalli, B. Vermang, J. Joel, R. Rajkumar, M. Edoff and D. Flandre, "Investigating the electronic properties of Al2O3/Cu(In,Ga)Se2 interface,"AIP Advances, 5, 107101, 2015.

[102] W.H. Wu and B.Y. Tsui, “Two-frequency C-V correction using five-element circuit model for high-k gate dielectric and ultrathin oxide”, Electron Device Lett. IEEE 27, 2006.

[103] K. Martens, C. O. Chui, G. Brammertz, B. De Jaeger, D. Kuzum, M. Meuris, M. M. Heyns, T. Krishnamohan, K. Saraswat, H. E. Maes et al., “A combined interface and border trap model for high-mobility substrate metal–oxide–semiconductor devices applied to $In_{0.53}Ga_{0.47}As$ and InP capacitors,” IEEE Trans. Electron Devices 55, 547 (2008).

[104] M. Gloeckler, Ph.D. thesis, Colorado State University, 2002.

[105] R. Kotipalli, B. Vermang, M.Edoff and D. Flandre,” On the development and analysis of a 1-D simulation model to address the Al_2O_3 rear surface passivation effects on CIGS solar cells” (article under preparation for RRL-Solar).

[106] M. Burgelman, J. Verschraegen, S. Degrave, P. Nollet,"Modeling thin-film devices," Prog.Photovolt: Res.Appl, pp. 143–153,2004.

[107] H. Movla “Optimization of the CIGS based thin film solar cells: Numerical simulation and analysis" Optik-International Journal for Light and Electron Optics 125 (1), pp. 67-70,2014.

APPENDIX A: MOS SEMICONDUCTOR

Effective oxide thickness (T_{ox}):

$$Tox = \frac{area * 10^7 \ * \varepsilon o * \varepsilon d}{Cox}$$

where

- A is the capacitor gate area [cm^2]
- ε0 is the free space permittivity (8.854 x 10^{-14} F/cm);
- ε_d is the dielectric constant of SiO_2 (3.9) and
- C_{ox} is the measured capacitance in heavy accumulation

Effective doping concentration (N_{sub}):

$$Nsub = \frac{4 * |\varphi_{fermi}|}{q * \varepsilon o * \varepsilon si} * \left(\frac{Csmin}{area}\right)^2$$

$$\varphi_{fermi} = \pm \frac{k * T}{q} * \ln\left(\frac{Nsub}{ni}\right)$$

where

- ϕ_{fermi} is the Fermi potential, in Volts;
- C_{smin} is the minimum depletion layer capacitance, in Farads;
- A is the area of the poly gate, in cm^2;
- n_i is the intrinsic carrier concentration per cm^3;

- ε_0 is the free space permittivity (8.854 x 10^{-14} F/cm);
- ε_{Si} is the dielectric constant of Si (11.7);
- q is the magnitude of electronic charge (1.602 x 10^{-19} Coulomb);
- k is Boltzman's constant (1.38 x 10^{-23} J/K);
- T is the absolute temperature, in Kelvin.

Flat band capacitance (C_{fb}):

$$Cfb = \frac{Cox * Csfb}{Cox + Csfb}$$

$$Csfb = \frac{\sqrt{2} * area * \varepsilon o * \varepsilon si}{\lambda}$$

where

- $Csfb =$ *is the depletion layer capacitance under flat band condition*
- λ = Debye length

$$\lambda = \sqrt{(2 * k * T * \varepsilon o * \varepsilon si) * \frac{1}{q^2 * Nsub}}$$

Threshold voltage (V_{th}):

$$Vth = Vfb + (2 * phi_{fermi} - area * \frac{Q_{fixedcharge}}{Cox})$$

Fixed Charge Density (Q_{fixed}):

$$Q_{fixedcharge} = \pm \frac{q * Nsub * \varepsilon o * \varepsilon si * area}{Csmin}$$

+ for n-type(PMOS)

- for p-type (NMOS)

Effective oxide charge (Q_{eff}):

$$Q_{eff} = Q_{fixed} + Q_{mobile} + Q_{oxidetrapped}$$

$$Qeff = \frac{Cox * (W_{ms} - V_{fb})}{area}$$

Effective oxide charge density (N_{eff} in cm^{-2}):

$$N_{eff} = \frac{Q_{eff}}{q}$$

Ideal Capacitance (vs) Voltage (Classical-Method):

$$U_f = \frac{\varphi_f}{\frac{k * T}{q}}$$

$$U_S = \frac{\frac{\varphi_s}{k * T}}{q}$$

where

Intrinsic Debye Length is given by

$$L_D = \left[\frac{Ks\ \mathcal{E}okT}{2q^2ni}\right]^2$$

$$U_S^{\wedge} = +1 \quad if\ U_s > 0$$

$$U_S^{\wedge} = -1 \quad if\ U_s < 0$$

$$C = (Co)/(1 + \left(\frac{KoWeff}{KsXo}\right) \qquad \ldots\ldots\ldots\ldots\ldots\ldots \quad eq.1$$

$$F\left(U, U_f\right) = \sqrt{[e^{U_f}(e^{-U} + U - 1) + e^{-U_f}\ (e^{U} - U - 1)]}\ .eq.2$$

$$V_G = \frac{kT}{q}\left[U_s + \ U_S^{\wedge}\ \frac{(K_s X_o)}{K_o L_D} * F\left(U, U_f\right)\right] \qquad eq.3$$

$$\begin{cases} U_S^{\wedge} L_D \left[\dfrac{2F(U_s, U_f)}{e^{U_F}(1-e^{-U_s}) + e^{-U_F}(e^{U_S}-1)}\right] \ldots acc \ \ldots eq.4 \\ Weff = \dfrac{\sqrt{2}L_D}{\sqrt{(e^{U_F} + e^{-U_F})}} \ . Flat\ band \ldots . eq. 5 \\ U_S^{\wedge} L_D \left[\dfrac{2F(U_s, U_f)}{e^{U_F}(1-e^{-U_s}) + \dfrac{e^{-U_F}(e^{U_S}-1)}{1+\Delta}}\right] \ldots \dfrac{dep}{inv} \ldots eq\ 6 \end{cases}$$

where

$$\Delta = \begin{cases} 0 \quad ..... \quad Low\ freq\ limit \\ \dfrac{\left(\dfrac{e^{U_S} - U_S - 1}{F(U_S, U_F)}\right)}{\int_0^{U_S} (e^{U_F}(1-e^{-U})(e^{U} - U - 1)/(2F^3(U, U_F))} \ dU \ldots \\ High\ freq\ Limit \ldots . eq(7) \end{cases}$$

Methods to extract D_{it}:

(1) Low frequency (Quasi-static) method:

$$Dit = \frac{1}{q^2} * (\frac{Cox * Clf}{Cox - Clf} - \frac{Cox * Chf}{Cox - Chf})$$

- C_{lf}=is the minimum of the qscv curve (low-freq curve)
- C_{hf}= is the minimum of the HF curve (High-freq curve)

(2) Parallel Conductance method:

$$\frac{Gp}{\omega} = \frac{\omega G_m Cox^2}{Gm + \omega^2 (Cox - Cm)^2}$$

$$Dit \approx \frac{2.5}{q * A * \left(\frac{Gp}{\omega}\right)_{max}}$$

where:

- C_{ox}=oxide capacitance calculated from T_{ox}
- C_m= measured capacitance
- G_m=measured Conductance
- ω = Angular freq normally

(3) Terman method:

$$Dit = \frac{Cox}{q^2} * \left(\frac{d\Delta VG}{d\varphi_s}\right)$$

Series resistance correction of C-V-G curves:

$$\frac{Gp}{\omega} = \frac{\omega G_c Cox^2}{{G_c}^2 + \omega^2 (Cox - Cc)^2}$$

where

$$C_c = \frac{C_m}{(1 - r_s\, G_m)^2 + (\omega r_s C_m)^2}$$

$$G_c = \frac{\omega^2\ r_s\ C_m\ C_c - G_m}{r_s\ G_m - 1}$$

$$r_s = \frac{Gma}{{G_{ma}}^2 + \omega^2 {C_{ma}}^2}$$

Dual-Frequency Five Element MOS-Small Signal Model:

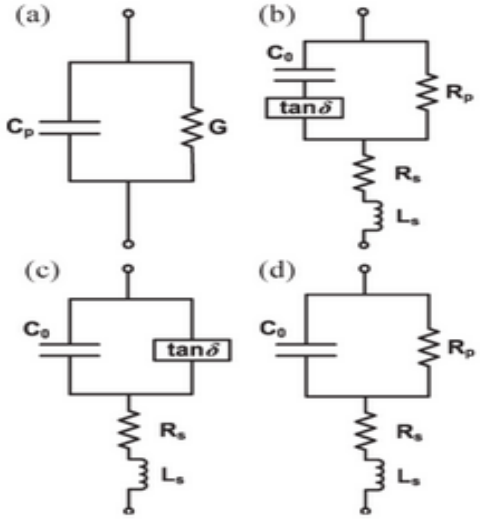

Small-signal equavelent circuit model of MOS capacitor (a) simple parrale circuit model (b) Five element model proposed by W.H.Wu et. el. (c) Four-element circuit model for low leakage high k-dielectrics (d) Four-element circuit model for ultra-thin and leaky k-dielectrics [taken from 101].

$$C_0 = \frac{(\omega_2^2 - \omega_1^1)(G_1^2 + \omega_1^2 C_1^2)(G_2^2 + \omega_2^2 C_{p2}^2)}{\omega_1^2 \omega_2^2 [C_{p1}(G_2^2 + \omega_2^2 C_{p2}^2) - C_{p2}(G_1^2 + \omega_1^2 C_{p1}^2)}$$

$$C_O R_p = \frac{C_{p1}(G_2^2 + \omega_2^2 C_{p2}^2) - C_{p2}(G_1^2 + \omega_1^2 C_{p1}^2)}{G_1(G_2^2 + \omega_2^2 C_{p2}^2) - G_2(G_1^2 + \omega_1^2 C_{p1}^2)}$$

where

- Suffix 1 represents low frequency curve (to be corrected for dispersion)

- Suffix 2 represents high frequency curve (1 Mhz)
- Suffix p represents parallel mode

APPENDIX B: SOLAR CELL JUNCTION CAPACITANCE

Charge density at the edge of the depletion region:

$$N(W) = -\frac{C^3}{q\varepsilon A^2\left(\frac{dC}{dV}\right)} = -\frac{2}{q\varepsilon A^2}\left[\frac{dV}{d(\frac{1}{C^2})}\right]$$

where

- W is width of the depletion region
- A is the area of the device
- q is the fundamental charge

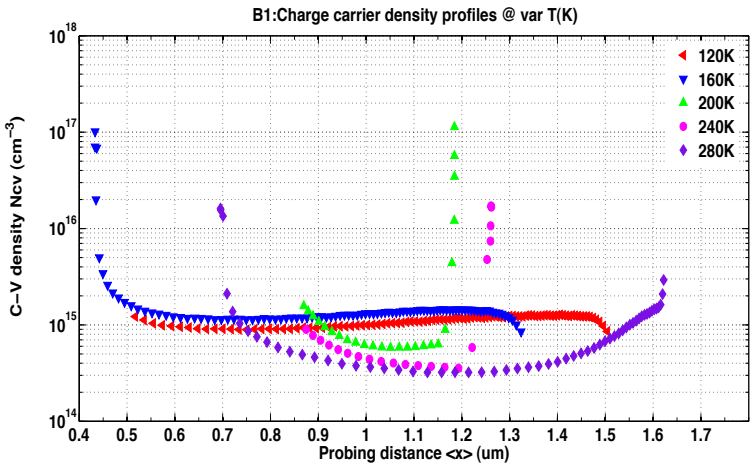

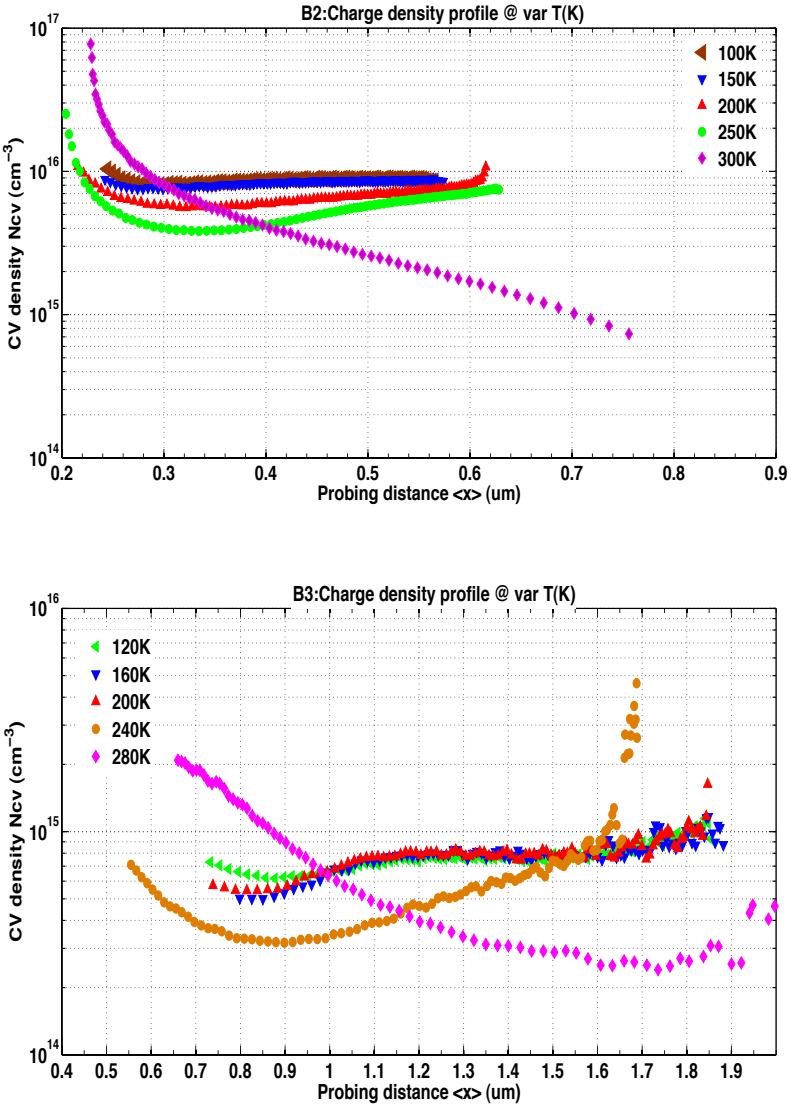

*C-V charge density as a function of temperature for B1: ungraded (**UG**), **B2**: front surface graded (**FSG**) and **B3**: double side graded (**DSG**) CIGS solar cell*

Deep-Level Capacitance Profiling (DLCP):

In DLCP additional non-linear CV terms (2^{nd}, 3^{rd} … harmonics) are taken into account;

$$\frac{dQ}{dV} = C_0 + C_1\, dV + C_2 dV^2 + \ldots\ldots\ldots$$

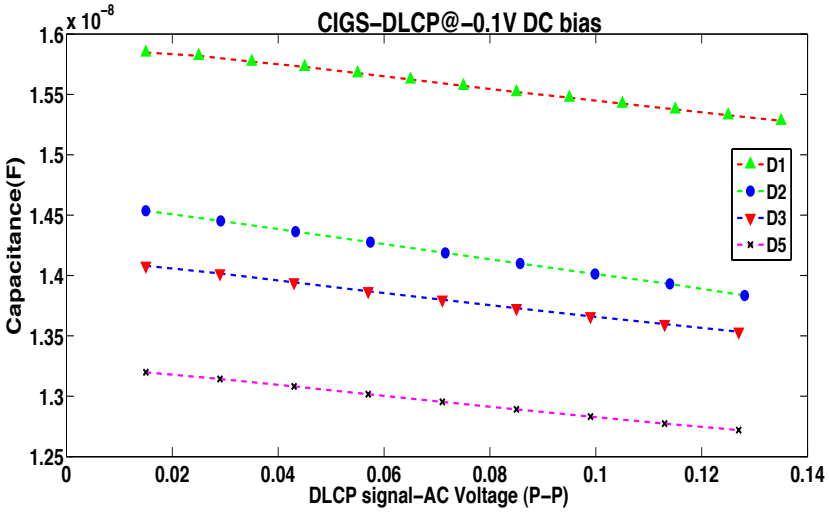

CIGS solar cell (UG) junction capacitance vs DLCP varying ac-signal amplitude

DLCP-Deep defect density (N_{DL}) is given by

$$N_{DL} = \frac{C_0^3}{2q\varepsilon A^2 C_1}$$

and the probing distance is given by

$$<x> = \frac{\varepsilon A}{C_O}$$

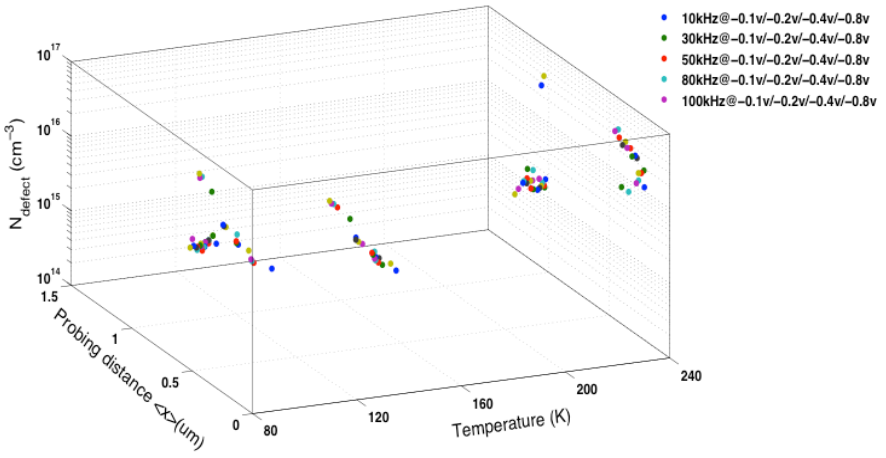

*DLCP as function of dc-voltage, frequency and temperature for ungraded (**UG**) CIGS Solar cells*

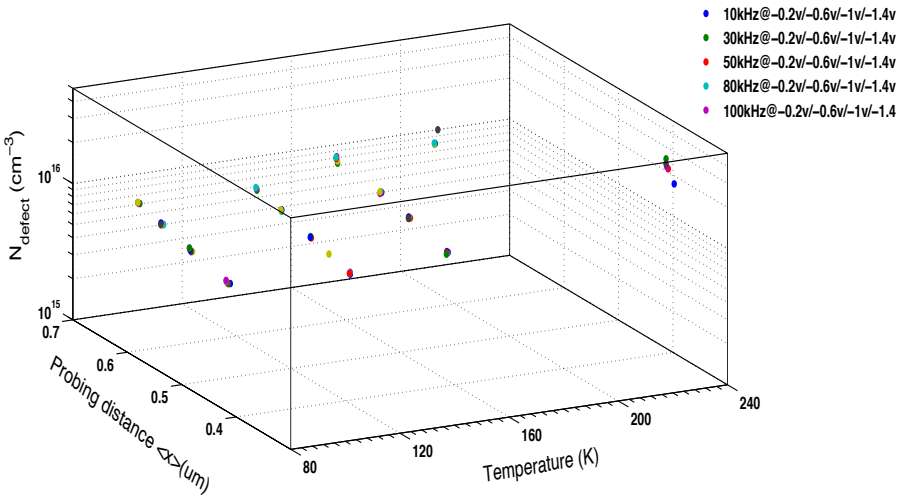

*DLCP as function of dc-voltage, frequency and temperature for front-surface graded (**FSG**) CIGS Solar cells*

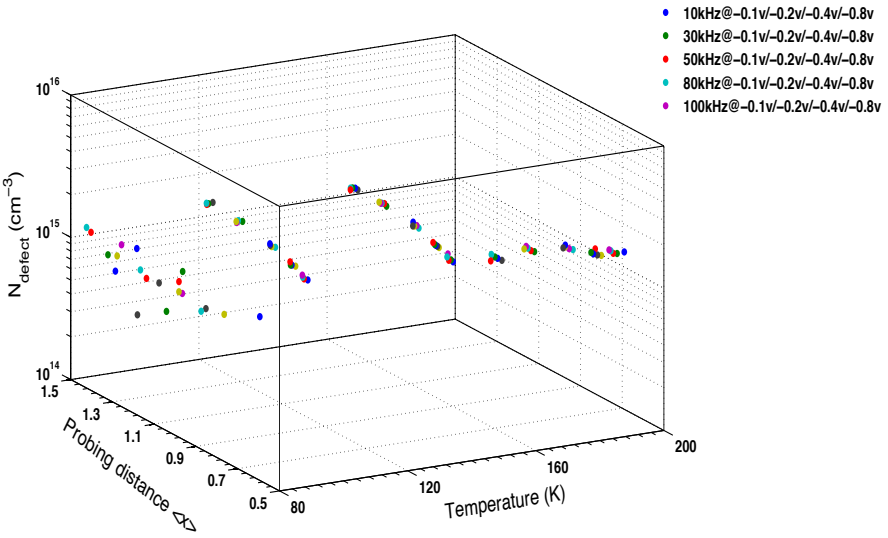

*DLCP as function of dc-voltage, frequency and temperature for double-sided graded (**DSG**) CIGS Solar cells*

***X-ray fluorescence* (*XRF*):**

Sample Type	Cu/III(%)	Ga/III(%)
Ungraded (UG)	**97.4**	**33.6**
Front Surface Graded (FSG)	**87.1**	**39.1**
Double Side Graded (DSG)	**87.6**	**35.2**

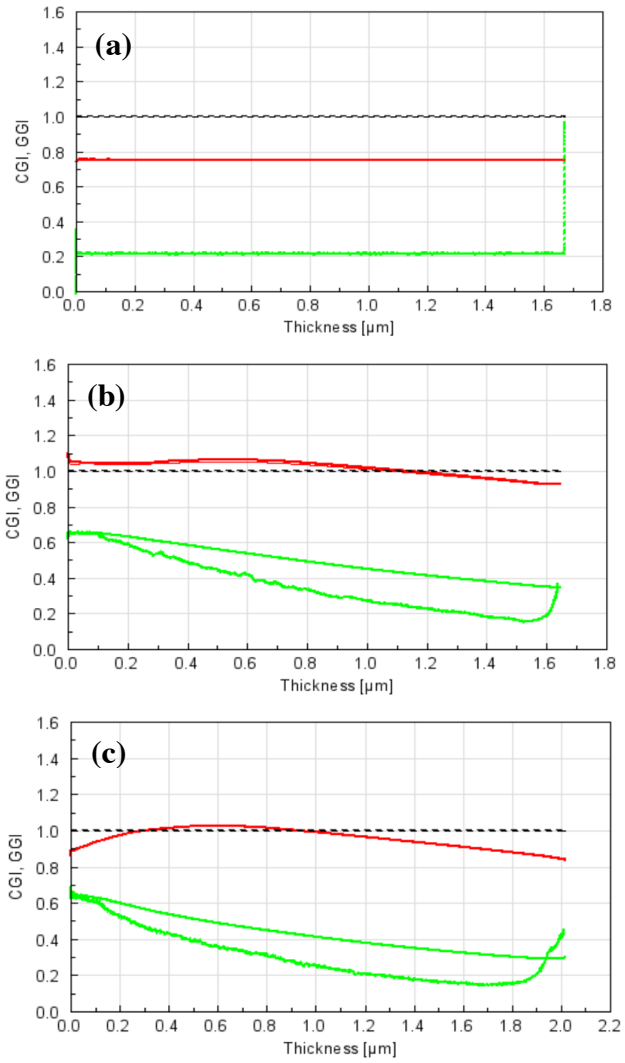

*Elemental depth profiling (**CGI** and **GGI**) in the target material for (a) UG, (b) BSG and (c) DSG CIGS solar cells*

Admittance Spectroscopy:

Density of states for a parabolic band that represents n^+p junction

$$N_t(E_\omega) = -\frac{2U_d^{3/2}}{w\sqrt{q}\sqrt{qU_d - (E_g - E_\omega)}}\frac{dC}{d\omega}\frac{\omega}{kT}$$

where

E_ω = Defect energy cross-over frequency (i.e. the frequency for which a defect at an energy *E* with respect to the valence band (E_V) can be charged and discharged by the ac signal.

U_d= built-in voltage in the junction

q= fundamental charge

E_g= bandgap of CIGS

k= boltzman constant

T= temperature in kelvin

APPENDIX C: CIGS SOLAR CELL FABRICATION STEPS

TABLE 1

OVERVIEW OF ALL STEPS INVOLVED TO FABRICATE Al_2O_3 (ALD/DC-SPUTTERED) REAR SURFACE PASSIVATED CIGS SOLAR CELLS FOR VARYING ABSORBER THICKNESS

Rear passivated CIGS solar cells for varying absorber thickness				
Step	240 nm	500 nm	1100 nm	1580 nm
1	Glass cleaning	Glass cleaning	Glass cleaning	Glass cleaning
2	Mo rear contact sputtering.	Mo rear contact sputtering.	Mo rear contact sputtering.	Mo rear contact sputtering.
3	ALD-Al_2O_3 passivation deposition	Particle-rich CBD CdS deposition	Particle-rich CBD CdS deposition	Particle-rich CBD CdS deposition
4	Rear contact openings using e-beam litho.	MgF_2-evap./ALD-Al_2O_3	ALD-Al_2O_3 passivation deposition.	ALD-Al_2O_3 passivation deposition.
5		CdS–particle removal	CdS–particle removal	CdS–particle removal
6	NaF evap.	NaF evap.	NaF evap.	NaF evap.
7	Ungraded CIGS co-evap.	Ungraded CIGS co-evap.	Ungraded CIGS co-evap.	Ungraded CIGS co-evap.
8	CBD CdS buffer deposition	CBD CdS buffer deposition	CBD CdS buffer deposition	CBD CdS buffer deposition
9	(i)ZnO(:Al)window sputt	(i)ZnO(:Al)window sputt	(i)ZnO(:Al)window sputt	(i)ZnO(:Al)window sputt
10	Ni/Al/Ni–front contact evap.	Ni/Al/Ni–front contact evap.	Ni/Al/Ni–front contact evap.	Ni/Al/Ni–front contact evap.

11	$0.5cm^2$ solar–cell scribing.	$0.5cm^2$ solar–cell scribing.	$0.5cm^2$ solar–cell scribing.	$0.5cm^2$ solar–cell scribing.
12	MgF_2 ARC evap.	MgF_2 ARC evap.		

SCAPS-model with baseline properties for Al_2O_3 passivated CIGS solar cells:

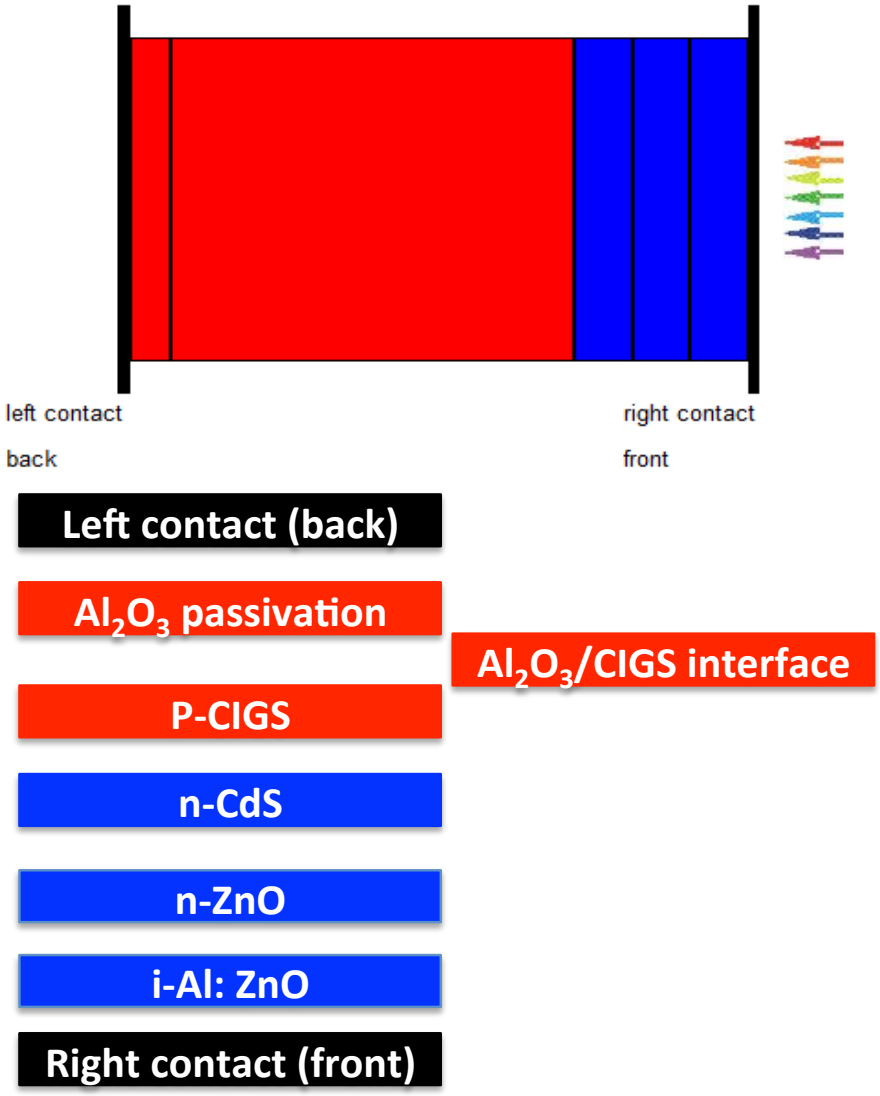

General Device Properties

	Front	Back
Φ_b [eV]	Φ_{bn} = 0.0	Φ_{bp} = 0.2
S_e [cm/s]	10^7	10^7
S_h [cm/s]	10^7	10^7
Reflectivity Rf	0.05	0.8

Gaussian Defect States

	ZnO	CdS	CIGS
N_{DG},N_{AG} [cm^{-3}]	D: 10^{17}	A: 10^{18}	D: 10^{14}
WG [eV]	0.1	0.1	0.1
σe [cm^2]	10^{-12}	10^{-17}	$5x10^{-13}$
σh [cm^2]	10^{-15}	10^{-12}	10^{-15}

Layer Properties

	ZnO	CdS	CIGS	Al_2O_3
W [nm]	200	50	2000	22.5
μe [cm^2/Vs]	100	100	100	100
μh [cm^2/Vs]	25	25	25	25
ε/ε0	9	10	13.6	13.6
n, p [cm^{-3}]	n: 10^{18}	n: 10^{17}	p: $2x10^{16}$	p: $2x10^{16}$
Eg [eV]	3.3	2.4	1.15	1.15
N_C [cm^{-3}]	2.2e18	2.2e18	2.2e18	2.2e18
N_V [cm^{-3}]	1.8e19	1.8e19	1.8e19	1.8e19